2015

Improving the accuracy performance of fringe projection profilometry for the 3D shape measurement of objects in motion

Lei Lu
University of Wollongong, 11490@uowmail.edu.au

IMPROVING THE ACCURACY PERFORMANCE OF FRINGE PROJECTION PROFILOMETRY FOR THE 3D SHAPE MEASUREMENT OF OBJECTS IN MOTION

A thesis submitted in fulfilment of the requirements

for the award of the degree

Doctor of Philosophy

from

University of Wollongong

by

Lei Lu

B. E., Henan University of Science and Technology, China

M. E., Zhengzhou University, China

School of Electrical, Computer and Telecommunications Engineering

March 2015

STATEMENT OF ORIGINALITY

I, Lei Lu, declare that this thesis, submitted in fulfilment of the requirements for the award of Doctor of Philosophy, in the School of Electrical, Computer and Telecommunications Engineering, University of Wollongong, is wholly my own work unless otherwise referenced or acknowledged. The document has not been submitted for qualifications at any other academic institution.

Signature: 

Lei Lu

31 March, 2015

ACKNOWLEDGEMENTS

I would like to take this opportunity to express my thanks to those who helped me in various aspects.

First, thanks to my supervisor Professor Jiangtao Xi, for his guidance, patience and support throughout my PhD career. His insights for research always inspired me and help me to well address the issues I met. Also, I want to thank my co-supervisors Dr. Yanguang Yu and Dr. Qinghua Guo for their valuable suggestions and encouragement.

I would like to thank my family members, my father Lianqing Lu, mother Yuping Wang and brother Ming Lu for their love, encouragement and support.

Thanks to my friends and colleagues in the lab. Dr. Ke Wu, Dr. Ke Chen, Dr. Yongkai Yin, Pu Cao, Zhengrong Huang provided a lot help for my research and we always discuss about the problems we met. Thanks to Dr. Ke Chen and his wife Wei Han, Dr. Chao Yu, Yuanlong Fan, Xiaochen He, Kankan Zhao, Yan Gao, Yuan Sun and other friends for countless parties and travels. I have a colourful and wonderful life in these three years.

Last but never least I would like to thank all the staffs of the School of Electrical, Computer and Telecommunications Engineering. I have a happy time in University of Wollongong with their cooperation and help.

AUTHOR'S PUBLICATIONS

Much of the work in this thesis has been published or submitted as academic papers. These papers are:

Journal papers:

1. Lei Lu, Jiangtao Xi, Yanguang Yu, and Qinghua Guo, "New approach to improve the accuracy of 3-D shape measurement of moving object using phase shifting profilometry," *Optics Express*, vol. 21, no. 25, pp. 30610-30622, 2013.
2. Lei Lu, Jiangtao Xi, Yanguang Yu, and Qinghua Guo, "New approach to improve the performance of fringe pattern profilometry using multiple triangular patterns for the measurement of objects in motion," *Optical Engineering*, vol. 53, no. 11, pp. 112211, 2014.
3. Lei Lu, Jiangtao Xi, Yanguang Yu, and Qinghua Guo, "Improving the accuracy performance of phase-shifting profilometry for the measurement of objects in motion," *Optics Letters*, vol. 39, no. 23, pp. 6715-6718, 2014.
4. Lei Lu, Jiangtao Xi, Yanguang Yu, and Qinghua Guo, Yongkai Yin, and Limei Song, "A novel shadow removal method for phase-shifting profilometry," *Applied Optics*, vol. 54, no. 19, pp. 6059-6064, 2015.

Conference paper:

1. Lei Lu, Jiangtao Xi, Yanguang Yu, and Limei Song, "An approach to compensate the object movement errors in phase shifting profilometry," *in Proceedings of SPIE - Optical Metrology and Inspection for Industrial Applications II*, 856304-856308, 2012.

CONTENTS

LIST OF FIGURES

LIST OF TABLES

ACRONYMS

3D: three-dimensional

2D: two-dimensional

FPP: fringe projection profilometry

PSP: phase-shifting profilometry

DMD: digital micro-mirror device

TOF: time-of-flight

CMM: coordinate measuring machine

FTP: Fourier transform profilometry

SVD: singular value decomposition

RMS: root mean square

ABSTRACT

This thesis focuses on improving the accuracy of using multiple-shot fringe projection profilometry (FPP) for three dimensional (3D) shape measurement of rigid objects with movement. By using information on the object movement, the errors caused by the object movement in the projection of the multiple fringe patterns are addressed. The author mathematically describes the movement of the rigid object using a rotation matrix and translation vector. The influence on the fringe patterns caused by the movement is then analysed. Because the movement of the object changes the height distribution of the object surface, and the height distribution is related to the captured fringe patterns, a new expression for fringe patterns with movement is obtained. Using the new expression, algorithms are proposed to address the errors caused by different types of movement. At last, the errors caused by the object movement are removed successfully.

At the beginning of this thesis, an algorithm based on phase-shifting profilometry (PSP) is proposed to address the errors caused by the two dimensional (2D) movement of the object. Firstly, the rotation matrix and the translation vector describing the movement of the object are estimated using a set of marks placed on the surface of the object. New expressions for the fringe patterns under the influence of the 2D object movement are then derived and used to determine the correct phase map, which leads to accurate measurement of the object profile.

Because the intensity ratio method with a triangular fringe pattern can be more efficiently calculated than the phase value in PSP, an algorithm based on the intensity ratio method is proposed to address the errors caused by 2D movement.

The movement of the object is described by the rotation matrix and the translation vector. The influence on the fringe patterns caused by the 2D movement of the object is then analysed and then used to estimate the normalised fringe patterns from the object without movement. Finally, the object is reconstructed by using the existing intensity ratio algorithm and incorporating the estimated fringe patterns, which leads to improved measurement accuracy.

In practice, the movement of an object is not limited to two dimensions. Therefore, a third algorithm based on PSP is proposed to address the errors when the object is subject to 3D movement. Because 3D movement introduces unknown height variation of the object, the algorithms used to account for 2D movement become invalid. An iterative least-squares algorithm is proposed to address the errors caused by the 3D movement. The object is limited to be a rigid object, and the movement consists of a translation in the direction of height and a 2D movement in the plane perpendicular to the direction of height. The proposed method does not require the height variation caused by the movement to be known in advance.

The thesis also addresses the errors caused by the shadow in PSP. Because the shadow areas in the captured image do not include the information of the fringe patterns, errors will be introduced to the measurement results. To remove the influence caused by the shadow, the reconstructed 3D results are mapped on a point-by-point basis to the corresponding positions on the digital micro-mirror device (DMD) of the projector. A set of rules are then presented to detect the shadow points based on their mapped positions on the DMD.

Experimental results are given to verify the proposed algorithms above. These proposed algorithms not only have the advantages of the multiple-shot technique, but

also improve the accuracy of the 3D reconstruction for an object with movement. The invalid points caused by the shadow are also removed and a high-quality result can be obtained. A 3D shape measurement system that can reconstruct a moving object with high accuracy is then built. Finally, the thesis is concluded and future work is proposed.

1 INTRODUCTION

1.1 Overview of 3D shape measurement techniques

The 3D shape measurement techniques have attracted intensive research due to the huge potential for application in many areas such as entertainment [1, 2], biomedicine [3], and design and manufacturing [4, 5]. Numerous techniques for 3D shape measurement have been developed in the past decades, e.g., time-of-flight (TOF) [6, 7], stereo vision [8-10] and structured light [11-15] techniques. Each of the techniques has different features, and therefore can be implemented into different applications [16-19]. As the application (such as the object on a conveyor etc.) is not limited to the stationary object measurement, the objective of the thesis work is to develop 3D shape measurement technique with high accuracy, dense resolution and fast measurement speed for the reconstruction of moving objects.

As shown in Fig. 1.1, 3D shape measurement techniques can be classified as contact based techniques and non-contact techniques. The non-contact techniques consist of active techniques and passive techniques. Based on differences in the principle of the reconstruction, the active techniques can be further classified as TOF techniques or structured light techniques. The TOF techniques reconstruct shape of an object based on the time of the flight of the projected laser or light beam. The structured light techniques reconstruct the shape of an object based on triangular relationships and are described as FPP and non-FPP according to the type of fringe patterns used. FPP techniques are divided into single-shot techniques and multiple-shot techniques based on the number of fringe patterns used.

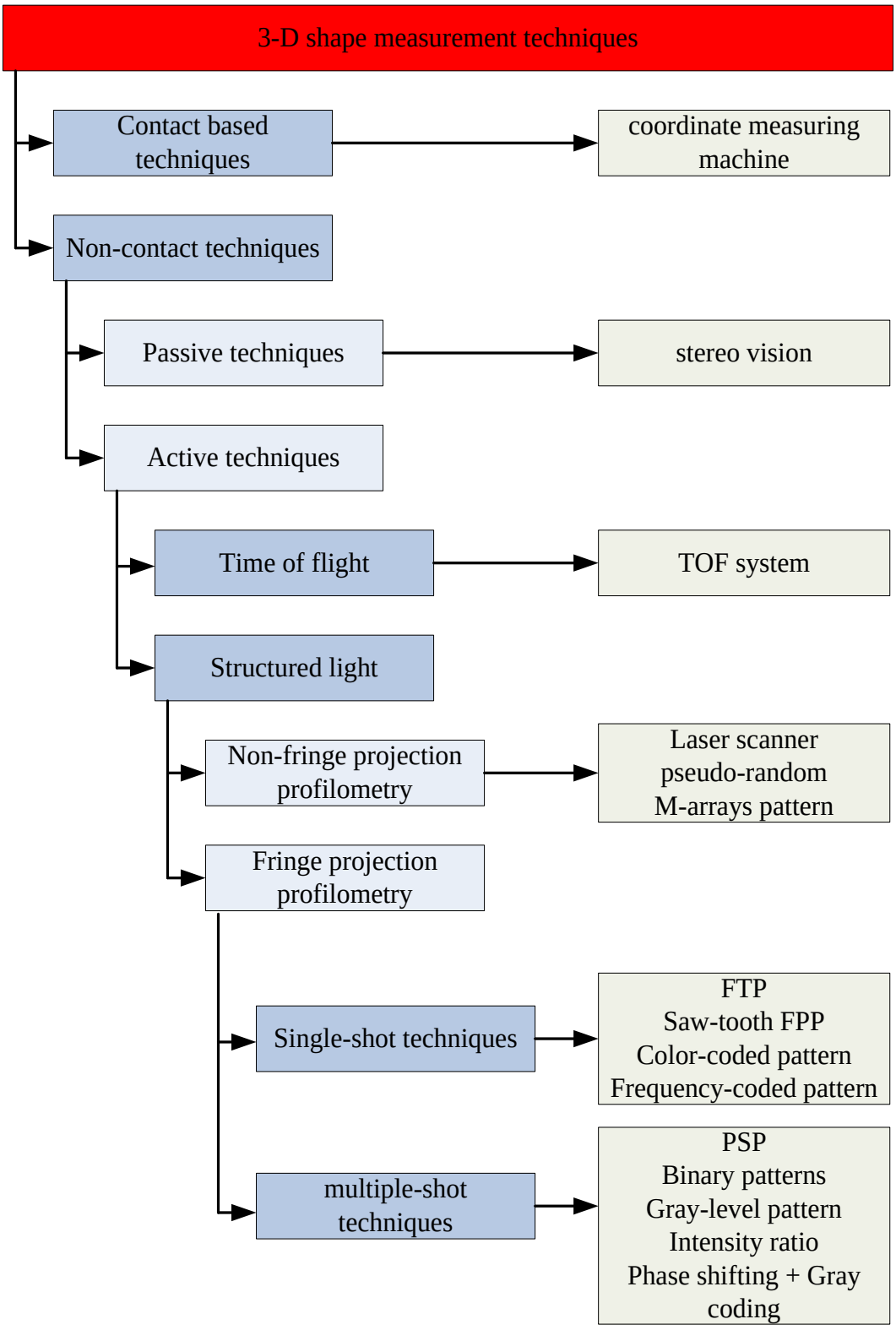

Fig. 1.1. Classifications of 3D shape measurement techniques.

1.1.1 Contact based techniques

To obtain a 3D reconstruction of the shape of an object, the most direct method is to measure the coordinates of each point on the object surface through contact. Contact based 3D shape measurement techniques, such as the coordinate measuring machine (CMM), have been developed for contact measurement [20, 21]. The CMM consists of three main components: the main body, the probing system and the data collection system. The main body includes the parts that control the motion of the probes. The probe makes contact with the surface of the object to be measured and the 3D data is then calculated by the data collection system. Contact based techniques can achieve accurate reconstruction results, but there are also some disadvantages. Contact based techniques take a long time to perform the reconstruction. Calibration of the passive arm of the probe is expensive and complex [22]. They also require touching the object directly, which may damage the object surface or not be possible for an object with a soft surface. In addition, the object must be kept stationary during the measurement. Therefore, contact based techniques are not feasible in many applications.

1.1.2 Non-contact techniques

Non-contact 3D shape measurement techniques were developed to address the disadvantages mentioned above. Non-contact techniques do not require touching the object during the reconstruction, and can therefore be used to measure objects with soft surfaces. Based on the method used to probe the object, non-contact techniques can be classified as either passive techniques or active techniques. Passive techniques use a camera to capture images of the object and do not require any pattern or light beam emitted onto the object surface. Only the ambient light from the object surface is reflected into the camera. The 3D shape of the object is then

reconstructed from the captured images. In contrast, for active techniques, a designed pattern or light beam is directly casted onto the object surface, which is coded by the projected pattern or light beam. Images of the object reflecting the pattern or light beam are then captured by a camera. The object can be reconstructed by analysing the relationship between the projected pattern or light beam and the captured ones. The details are presented in the following sections.

1.1.2.1 Passive techniques

Passive techniques for 3D shape measurement only rely on ambient light to capture the image of the measured object. Stereo vision is a typical passive 3D shape measurement technique [8, 23, 24]. Inspired by the two eyes of humans, two cameras are used to capture images of the measured object from different angles. The position of the object in the two captured images will have a relative difference. This relative difference is known as disparity, and can be used to reconstruct the 3D shape of the object. The disparity map can be obtained by finding the points on the two captured images that correspond to the same point on the object. The 3D information about the object can then be extracted using system parameters that are obtained from calibration of the stereo vision system. The stereo vision technique only employs the cameras for reconstruction of the object, and the image acquisition speed can be as high as the speed of the camera. However, because the object is reconstructed by using the two captured images to detect the corresponding points on the object, the stereo vision technique requires a high computational time and the reconstructed result has difficulty reaching pixel-level resolution [25]. Importantly, only the points on the object that overlap in the two captured images can be reconstructed because the technique requires the object to be captured by two cameras at the same time, resulting in a small range of the measurement in the angle

of view. Furthermore, it is difficult to measure objects with texture-less surfaces because the process for finding the correspondences will be complex [26]. All of the above disadvantages limit the application of the stereo vision techniques.

1.1.2.2 Active techniques

Instead of only using the object texture and the ambient light reflected from the object surface as in the passive techniques, active techniques project a designed pattern or light beam onto the object surface to reconstruct the object. Compared with the emitted pattern or light beam, the reflected pattern or light beam will be distorted or delayed because of the height distribution of the object. The object can then be reconstructed by analysing the relationship between the projected pattern or light beam and the received ones that has been reflected from the object surface. Depending on the principle used for reconstruction, active techniques can be classified into two categories [27]: the first is based on the TOF [6, 7, 28], and the second is the triangular-based structured light techniques [8, 11, 29-31]. The structured light techniques can be further classified as the FPP techniques or non-FPP techniques. The details are described below.

(1) TOF techniques

A typical TOF system consists of a light source and a light sensor [32]. A modulated light beam is emitted by the light source and then reflected back from the object surface and captured by the light sensor. The time interval between the emission of the light beam and the capture of the reflected light is calculated. The distance of the object determines the value of the time interval between emitting and capturing the light beam. Using the speed of light, the height information of the object can be obtained by estimating the elapsed time between the emission and capture of the projected light beam. To reconstruct the whole surface of the object, each point on

the object needs to be scanned, and therefore the TOF techniques are limited in terms of speed. In addition, the reconstructed resolution and the accuracy of TOF techniques are low [6, 7].

(2) Structured light techniques

Structured light techniques project a coded pattern or light beam onto the object surface to reconstruct the 3D shape of the object. An imaging sensor (e.g., a camera) is used to acquire a 2D image of the object under the structured light illumination. The captured structured light will be distorted by the height of the object surface. The 3D shape of the object is then extracted from the difference between the projected pattern or light beam and the captured ones. Structured light techniques reconstruct the object 3D shape based on the triangular relationship. Based on the different types of the projected pattern or light beam, structured light techniques can be classified as non-FPP and FPP.

I. Non-fringe projection profilometry

Laser scanner techniques [33, 34] project a line of coded laser onto the surface of the object, and then a camera is used to detect the reflected line. The laser scanner system can achieve high resolution and accuracy, leading to high quality 3D surface reconstruction. In each acquired image, only the points belonging to the laser stripe can be reconstructed, and therefore, a large number of images must be acquired to reconstruct the whole object. Furthermore, the object is required to be stationary during the measurement.

The pseudo-random speckle pattern [11, 35] and the M-arrays pattern [36] are two typical techniques that project dots to reconstruct the 3D shape of object. The aim of the pseudo-random speckle and M-arrays pattern techniques is to have a unique

intensity pattern in every sub-window, which allows successful identification of the projected pattern. Microsoft Kinect [2] uses the pseudo-random speckle technique successfully. Specifically, a pseudo-random speckle pattern is projected onto the scene by an infrared laser and is viewed by a camera. The shift of the speckle pattern in space is measured and then mapped to depth through triangulation. Relying on the single-frame correspondence strategy, Kinect can capture dynamic depth at 30 frames per second. However, due to the limited distinguish ability of a single fixed pattern, the accuracy and resolution is not high [11].

II. Fringe projection profilometry

FPP projects fringe patterns onto the object to reconstruct the 3D shape of the object. A projector or laser interference can be used to generate the fringe patterns, and the type of the fringe pattern can be sinusoidal [37], binary [38], triangular [39, 40], trapezoidal [41] or saw tooth [42]. Today, FPP is widely used in 3D shape measurement because of its potential to achieve high accuracy, dense resolution and high speed measurement [43].

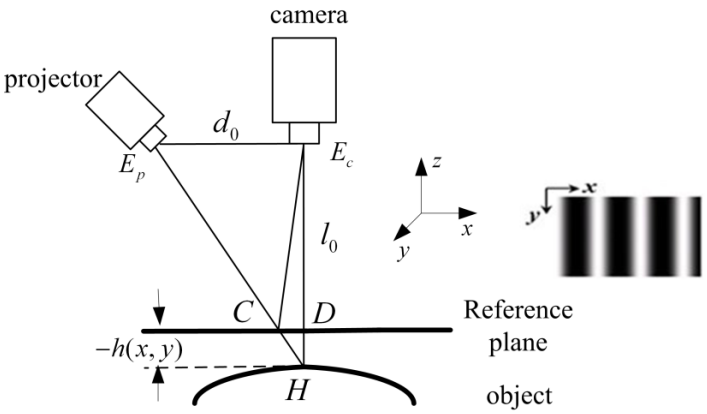

Fig. 1.2. The structure of the FPP system.

A typical structure of a 3D shape measurement system based on FPP techniques is shown in Fig. 1.2. The system consists of a camera, a projector and a reference

plane, where d_0 is the distance between the camera and the projector, l_0 is the distance between the camera and the reference plane and $h(x, y)$ is the height distribution of the object. During measurement, a set of fringe patterns is first projected onto the reference plane and an image is captured by the camera. Then, after removing the reference plane, the same set of fringe patterns is projected onto the object surface and an image is captured by the same camera [44]. Because of the shape of the object, the fringe patterns reflected from the object surface will have distortions. The shape information of the object can be extracted by the difference between the fringe patterns captured from the object and the reference plane. An overview of FPP techniques is presented in the following section.

1.2 Literature review of FPP

This section reviews the algorithms for the FPP techniques. According to the number of fringe patterns used, FPP techniques can be classified as single-shot techniques or multiple-shot techniques. Because the proposed algorithms in this thesis are based on the PSP and intensity ratio methods, the principles of these two algorithms are also presented in detail. Finally, related work for the measurement of moving objects based on multiple-shot FPP and shadow removal are also discussed in this section.

1.2.1 Single-shot techniques and multiple-shot techniques

Single-shot techniques such as Fourier transform profilometry (FTP), the colour-coded pattern technique and the frequency-coded pattern technique only require one fringe pattern to reconstruct the 3D shape of the object. Therefore, single-shot techniques are suitable for the measurement of a moving object. However, because only one fringe pattern is used, single-shot techniques are affected by the noise such

as ambient light and variation in the reflectivity of the object surface, resulting in low accuracy in 3D shape of the reconstructed object. In contrast, multiple-shot techniques such as PSP, binary pattern profilometry and the intensity ratio method require more than one (normally at least three) fringe patterns to reconstruct the 3D shape of the object. Because more information is used, multiple-shot techniques are more robust than the single-shot techniques and can achieve a high accurate result. However, multiple-shot techniques require more time to acquire the fringe patterns, and the object must be kept stationary during the projection of the multiple fringe patterns. Errors will be introduced when the object moves. The details are described in the following sections.

1.2.1.1 Single-shot techniques

(a) FTP

FTP was first introduced by Takeda *et al.* [45] and only requires one sinusoidal fringe pattern to reconstruct the 3D shape of an object. Instead of working in a spatial domain, FTP extracts the phase value in the frequency domain. Using the captured fringe pattern, the first step is to apply the Fourier transform to the captured intensity values. In the frequency domain, the phase component can be isolated from the background component and extracted using a band-pass filter. The phase distribution is then obtained by applying the inverse Fourier transform to the phase component. Because only one fringe pattern is required, FTP is suitable for real-time 3D shape measurement [27, 46, 47]. However, the design of the filter used in FTP is difficult to obtain the phase component clearly because there will be overlap between the phase component and the fundamental component when the spatial frequency of the fringe pattern is low [48].

(b) Saw-tooth FPP

A saw-tooth fringe pattern can be employed to reconstruct the 3D shape of the object because it has a similar shape to the wrapped phase map [42]. Only one saw-tooth fringe pattern is required to be projected onto the object surface and then captured by the camera. The deformed saw-tooth pattern encoding the object shape is converted to a wrapped phase map without using the phase extract algorithm. The object is then reconstructed using the triangular relationship. Because saw-tooth FPP uses the captured fringe patterns to reconstruct the object directly, the noise in the fringe patterns will significantly affect the accuracy.

(c) Colour-coded pattern techniques

Taking advantage of colour projection and capture techniques, multiple fringe patterns can be combined into one colour-coded fringe pattern that includes all of the information of the fringe patterns used in the multiple-shot techniques [49-58]. The colour-coded fringe pattern is a composite of the red, green and blue colours in the projector that is projected onto the object surface. A camera with a 3-channel charge-coupled device is used to capture the fringe pattern. The 3-channel charge-coupled device camera has three independent acquisition channels for red, green and blue, and each channel corresponds to a specific spectrum band. The different colours in the captured fringe pattern are separated by the different channels. In this way, three fringe patterns can be obtained from one shot. The 3D shape of the object is then reconstructed using the information obtained from the three channels. Because only one composite fringe pattern is used, this technique can achieve high speeds and can be used for measurement of moving objects. A disadvantage is that cross-talk between the different channels of the camera affects the accuracy of the reconstructed 3D shape [59].

(d) Frequency-coded pattern techniques

Instead of combining multiple fringe patterns by colour, Guan, *et al*. [60] combined the multiple patterns of PSP into a composite pattern based on different frequencies. In their system, each PSP fringe pattern is modulated along an orthogonal direction with a distinct carrier frequency. The modulated fringe patterns are then summed to form a single frame and projected onto the target object. The reflected image is captured by the camera and then decoded to retrieve the multiple PSP frames. Each PSP fringe pattern is separated using band-pass filters and the depth of the object can be reconstructed using the traditional PSP method. The band-pass filters used in the decoding procedure will, however, increase the complexity and blur the depth of the reconstruction.

1.2.1.2 Multiple-shot techniques

(a) Binary pattern techniques

Binary pattern techniques code the fringe patterns with black and white stripes [61-63]. Only two illumination levels (0 and 1) are used, and these form a sequence of the projection patterns. In general, N fringe patterns can code 2^N stripes, and each point on the object has a unique binary code. Because only 0 and 1 are used in the fringe patterns, the binary coding technique is robust to ambient light and the surface characteristics of the object (such as variation in reflectivity). The resolution of the binary coding technique is low when a limited number of fringe patterns are employed. The resolution can be increased by projecting a large number of sequential fringe patterns, which results in a significant increase in the acquisition time. This technique requires the object to be kept stationary during the projection of the binary code, and, this method is, therefore, not suitable for high-resolution measurement of moving objects.

(b) Gray-level pattern techniques

Binary coding techniques only use two illumination levels in the projected fringe patterns. This means that the illumination levels of the projector are not fully used and a larger number of fringe patterns are needed to increase the resolution of the measurement. To reduce the number of the fringe patterns used and achieve high measurement resolution, gray-level pattern techniques use fringe patterns with multiple illumination levels to reconstruct the object [64-67]. Assuming that the intensity values of the projected fringe pattern are classified into M levels (binary coding is the case when $M = 2$) and N fringe patterns are used, M^N stripes can be coded. Using the gray-level pattern technique, the number of required fringe patterns can be reduced significantly, but it is easily affected by variations in the reflectivity of the object surface and the threshold used to distinguish the different gray levels is not reliable when multiple levels are used.

(c) Intensity ratio techniques

Intensity ratio techniques [39, 40, 68, 69] were developed to use all illumination levels of the projector to measure the 3D shape of the object surface. Intensity ratio techniques use at least two patterns: a ramp pattern and a uniform pattern. The intensity value of the ramp pattern increases across the whole image and uses all illumination levels of the projector. The 3D information can be obtained from the difference between the two patterns [70, 71]. The advantage of the intensity ratio techniques is the fast processing speed, but it is limited by the number of illumination levels (normally 255 levels for the projector) and the resolution is low when a large object is measured. Intensity ratio techniques are sensitive to noise such as the ambient light and variations in the reflectivity of the object surface. These disadvantages can be overcome by projecting periodical patterns such as triangular

fringe patterns and trapezoidal fringe patterns [39, 40, 72-74]. However, the ambiguity problem will be introduced when periodical patterns are used.

(d) PSP

PSP is a well-known 3D shape measurement technique that employs sinusoidal fringe patterns [75-80]. The multiple fringe patterns are equally phase shifted and at least three fringe patterns are normally required to reconstruct the 3D shape of the object. Phase information from the projected fringe patterns are used to reconstruct the object. During the calculation of the phase value, the effects of ambient light and the reflectivity of the object surface can be eliminated. Therefore, the PSP algorithm is more robust to noise and can achieve high accuracy in the measurement result. However, because multiple fringe patterns are used, the object is required to be kept stationary during the projections of the fringe patterns. If the object moves during the measurement, errors will be introduced into the result. In addition, because periodical patterns are used, the ambiguity problem also exists in PSP.

(e) Phase-shifting and gray coding technique

Fringe patterns with multiple periods use the illumination levels of the projector efficiently and can achieve high resolution. However because the intensity values of the fringe patterns are repeated between the different periods, the ambiguity problem of the fringe order is introduced. Unwrapping algorithms [81-84] can be used to address this ambiguity. By combining the gray code and the multiple period fringe pattern techniques, the ambiguity problem can be addressed [85]. Let us take PSP as an example to show how it works. After the fringe patterns of PSP are captured, the gray code patterns are projected and captured. The decoded gray code helps to determine the order of the fringe patterns without any ambiguity and the object is reconstructed by PSP with high accuracy and high resolution. However, this method

requires a large number of projections and it is not suitable for the measurement of a moving object.

1.2.2 Principles of the PSP and the intensity ratio method

The proposed algorithms in this thesis are based on PSP and the intensity ratio method. The following sections present the details of the reconstruction principles of these two algorithms.

1.2.2.1 Principle of the PSP

A typical structure of a PSP system is shown in Fig. 1.2. Considering the use of *N*-step PSP, the sinusoidal fringe patterns acquired from the reference plane and the object can be expressed, respectively, as follows:

$$s_n(x,y) = a + b\cos(\phi(x,y) + \frac{2\pi(n-1)}{N}) \tag{1.1}$$

and

$$d_n(x,y) = a + b\cos(\phi(x,y) + \Phi(x,y) + \frac{2\pi(n-1)}{N}) \tag{1.2}$$

where $n = 1,2,3,...,N$; $s_n(x,y)$ is the *n*th fringe pattern on the reference plane; $d_n(x,y)$ is the *n*th fringe pattern on the object; a is the average intensity and b is the intensity modulation of the sinusoidal fringe patterns. To simplify the problem, we assume a and b are constant. $\phi(x,y)$ is the phase value on the reference plane and $\Phi(x,y)$ is the phase difference between the reference plane and object that is caused by the shape of the object. The phase maps of the reference plane and the object can be calculated by

$$\phi^r(x,y) = \phi(x,y) = \arctan \frac{-\sum_{n=1}^{N} s_n(x,y) \sin 2\pi(n-1)/N}{\sum_{n=1}^{N} s_n(x,y) \cos 2\pi(n-1)/N} \tag{1.3}$$

and

$$\phi^o(x,y) = \phi(x,y) + \Phi(x,y) = \arctan \frac{-\sum_{n=1}^{N} d_n(x,y) \sin 2\pi(n-1)/N}{\sum_{n=1}^{N} d_n(x,y) \cos 2\pi(n-1)/N} \tag{1.4}$$

where $\phi^r(x,y)$ is the phase value on the reference plane and $\phi^o(x,y)$ is the phase value on the object surface. The function arctan(·) is defined as the four-quadrant inverse tangent.

In Eqs. (1.3) and (1.4), the phase values calculated by arctan(·) are wrapped into $-\pi$ to π and are discontinuous. To calculate the height of the object, the phase unwrapping algorithm (such as quality guide method [83] and multiple-frequency method [87] etc.) is used to remove the discontinuities from the wrapped phase values to obtain a true phase value [81-83, 86-89]. The method described in [83] is used in this chapter. Assuming that $\Phi^r(x,y)$ and $\Phi^o(x,y)$ are the unwrapped phase values for $\phi^r(x,y)$ and $\phi^o(x,y)$, respectively, then the relationship between the wrapped phase value and the true phase value is

$$\begin{cases} \Phi^r(x,y) = 2\pi k^r(x,y) + \phi^r(x,y) \\ \Phi^o(x,y) = 2\pi k^o(x,y) + \phi^o(x,y) \end{cases} \tag{1.5}$$

where $k^r(x,y)$ and $k^o(x,y)$ are the integers defining the fringe number of $\phi^r(x,y)$ and $\phi^o(x,y)$, respectively. The phase difference between the reference plane and the object can then be calculated by

$$\Phi(x,y) = \Phi^o(x,y) - \Phi^r(x,y) \tag{1.6}$$

Now that we have obtained the phase difference between the object and the reference plane, the height distribution of the object can be calculated from the triangular relationship of the system. As shown in Fig. 1.2, because $\Delta E_p E_c H$ is similar with ΔCDH, we can have

$$\frac{\overline{CD}}{d_0} = \frac{-h(x,y)}{l_0 - h(x,y)} \tag{1.7}$$

Because point *C* and point *D* are both points on the reference plane, the phase difference $\Phi(x,y)$ can be calculated by

$$\Phi(x,y) = 2\pi f_0 \overline{CD} \tag{1.8}$$

where f_0 is the spatial frequency of the fringe patterns on the reference plane. Substituting Eq. (1.8) into Eq. (1.7), the height of the object can be calculated by

$$h(x,y) = \frac{l_0 \Phi(x,y)}{\Phi(x,y) - 2\pi f_0 d_0} \tag{1.9}$$

1.2.2.2 Principle of the intensity ratio method

The intensity ratio method with triangular pattern is used in this thesis and the structure can also be described by Fig. 1.2. A set of *N* triangular fringe patterns is projected onto the reference plane and the object surface and captured by the camera.

The fringe patterns have the same spatial period T, but are successively shifted by T/N. With these N fringe patterns, the following equation is employed to yield a function called the intensity ratio [90, 91]:

$$r_0(x,y) = \frac{\sum_{n=1}^{N}(-1)^{n+1} p_n(x,y) - \mathrm{mod}(N,2) \times p_{\min}(x,y)}{p_{\max}(x,y) - p_{\min}(x,y)} \qquad N \geq 2 \tag{1.10}$$

where $p_n(x,y)$ is the nth highest intensity value among the N projected patterns at the location of (x,y), and $p_{\max}(x,y)$ and $p_{\min}(x,y)$ are the maximum and minimum intensities of the triangular patterns. Note that these fringe patterns are vertical stripes, with the light intensity being constant in the y direction but varying in a triangular way in the x direction. It can be shown that $r_0(x,y)$ is still a triangular function with the period T/N, but its value is normalised into the range [0,1] by Eq. (1.10). The following is then applied to $r_0(x,y)$:

$$r_T(x,y) = \begin{cases} (-1)^{k+1} r_0(x,y) + 2 \times round(\frac{k-1}{2}) & k = 1,2,...,2N, N \text{ is the odd number} \\ (-1)^{k} r_0(x,y) + 2 \times round(\frac{k}{2}) - 1 & k = 1,2,...,2N, N \text{ is the even number} \end{cases} \tag{1.11}$$

where k is the region number, by which each fringe period T is divided into $2N$ equally spaced segments. With the operation in Eq. (1.11), we can obtain a function $r_T(x,y)$ that monotonically increases over every fringe period T. Then, $r_T(x,y)$ can be unwrapped to yield $r(x,y)$, which monotonically increases over the whole image pattern space. Note that these operations are applied to the fringe patterns from the

object surface and the reference plane, yielding two unwrapped intensity ratios, $r_d(x,y)$ and $r_s(x,y)$ respectively.

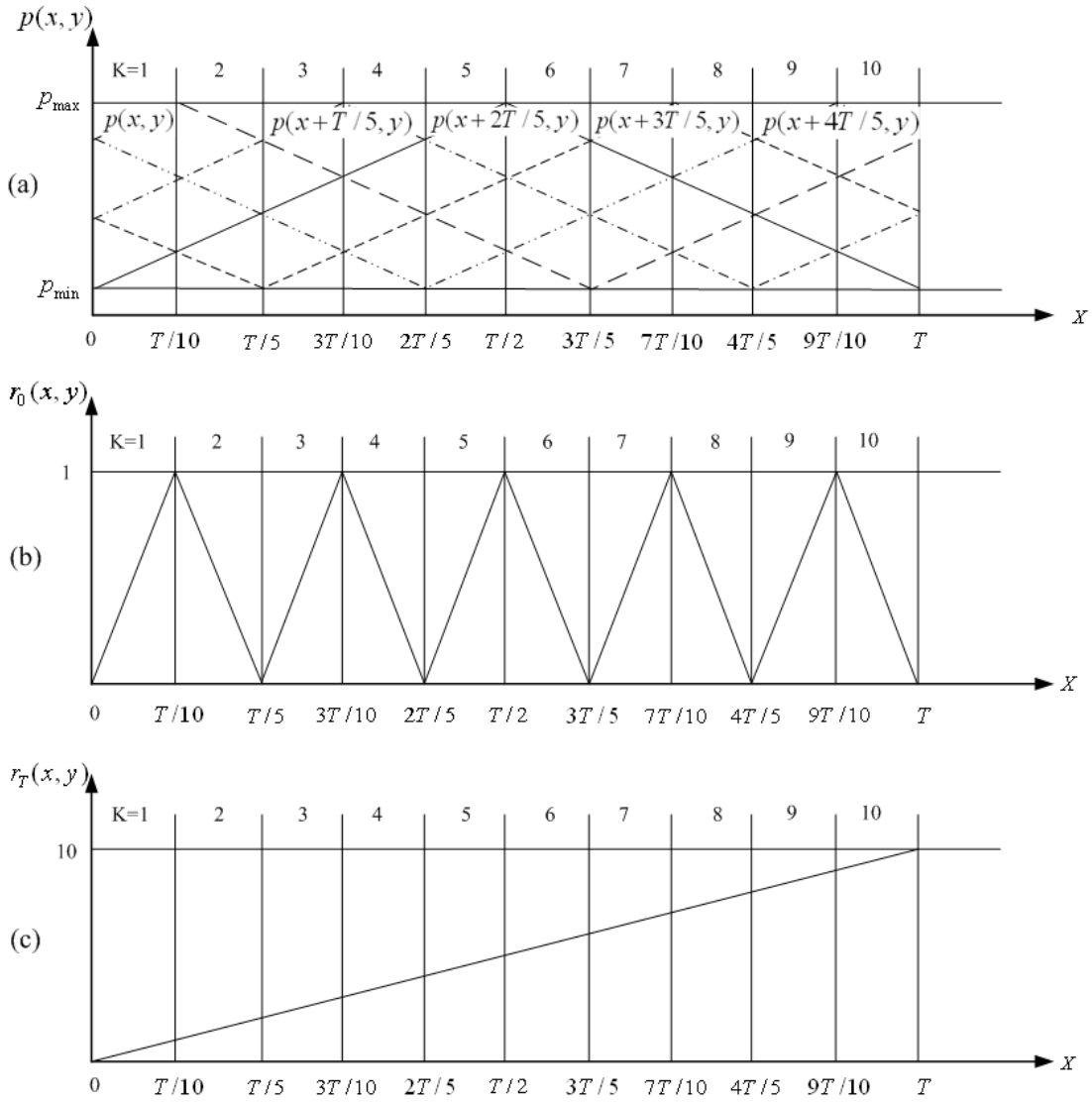

Fig. 1.3. Five-step triangular pattern phase-shifting method: (a) cross-section of the five triangular patterns shifted by $T/5$ of the fringe period; (b) cross-section of the triangular shape intensity ratio; (c) cross-section of the intensity ratio ramp after removal of triangles.

The height of the object can be calculated as follows:

$$h(x,y)=\frac{\Delta r(x,y)}{Td_0/pl_0+(1/l_0)\Delta r(x,y)} \tag{1.12}$$

where $h(x, y)$ is the height distribution of the object, $\Delta r(x, y) = r_d(x, y) - r_s(x, y)$ is the unwrapped intensity ratio difference between the object and the reference plane, T is the fringe pitch of the pattern generated by a computer and p is the fringe pitch on the reference plane.

To illustrate the procedure described above, let us use an example where five triangular patterns are employed. Figure 1.3 shows the cross-section of the five triangular patterns on the reference plane, and Fig. 1.3(a) shows the intensity of the five spatially shifted triangular fringe patterns; $r_0(x, y)$ is still triangular with the period $T/5$ but is normalised into the range [0,1], and $r_T(x, y)$ has its value increasing from 0 to 10 over the period T.

1.2.3 Related work

This section discusses the related work of the issues on the 3D measurement for the moving object based on multiple-shot technique and shadow removal.

As discussed in Section 1.2.1, the single-shot technique is suitable for the 3D reconstruction of the object in motion because of its fast speed. However, the accuracy is low. The multiple-shot technique can achieve high accuracy 3D result but errors will be introduced if the object is moved during the measurement. For removing the errors caused by the movement in multiple-shot techniques, the challenges are: (1) track the movement of the object; (2) remove the influence caused by the movement.

For the shadow removal issue, as the shadow has no information of the projected fringe patterns used in the FPP technique, the shadow area in the captured fringe

pattern will cause errors in the reconstructed result. The existing methods always require complex calculation or threshold determination, which limit the application.

The related work for the above two issues are presented in the following.

1.2.3.1 Related work for the measurement of a moving object based on multiple-shot FPP

Yuan and Tan, *et al*. [92, 93] developed a tracking fringe projection method to simultaneously measure variations in both the position and the shape of a moving object. Their method combines a commonly used FPP method and a laser tracking technique into the optical system. The measurement fringe patterns come from a projector and the tracking fringe patterns are emitted by a He-Ne laser with high intensity. The measurement fringe patterns are captured by a camera and are used to reconstruct the object. The tracking fringes are detected by a position sensing detector and are used to track the object. The object is reconstructed by the conventional fringes and the order of the conventional fringes is determined by the tracking fringes. This method not only requires a projector and camera, but also needs a laser and position sensing detector to reconstruct the object. This increases the cost of the hardware.

Rusinkiewicz and Hall-Holt, *et al*. [94, 95] proposed a method that uses boundary coded stripe patterns that vary over time to measure the moving object. A triangulation-based scanning system for moving scenes is introduced. To allow the object to move during scanning, the system uses a new kind of illumination pattern that is based on coding the boundaries between the projected stripes. The boundaries are tracked from frame to frame, permitting the determination of depth, even in the presence of moving objects in the scene. By finding the nearest stripe patterns over

time, a unique code can be determined for any stripe at any time. However, this method requires the object to be moved slowly to avoid erroneous temporal correlations. Moreover, because only the depths at the stripe boundaries are measured in this method, the reconstruction speed is low.

Zhang and Yau [96] proposed a modified two-plus-one phase-shifting algorithm to reconstruct the 3D shape of a moving object. In their method, two sinusoidal fringe patterns with π phase shifting and a uniform flat image are used to calculate the phase map. The two phase-shifted fringe patterns contain the height information of the object, and the uniform flat image provides the texture information for the measurement and it is less sensitive to movement. Because only two sinusoidal fringe patterns carry the information about the object profile, measurement error due to motion is smaller than in traditional PSP. Compared with traditional PSP, this method maintains the measurement speed (three fringe patterns are needed) while reducing the errors caused by motion. However, errors still occur when the object moves during the projections of the two sinusoidal fringe patterns.

Thibaut, *et al*. [97] proposed a method combining a sinusoidal phase-shifting method and stereo matching techniques to measure a moving object with motion compensation. Their method combines the benefits of the two techniques, which are high reconstruction accuracy through use of a phase-shifting technique and robustness to discontinuities through stereo vision. The system includes a projector, two high-speed monochrome cameras and a texture camera. For the phase-shifting algorithm, three images are required to calculate the phase. To be as insensitive to motion as possible, the three images need to be acquired in quick succession. The proposed system has an inter-frame delay of 6 milliseconds. Despite this fast

acquisition speed, the motion will still distort the calculated phase and affect the reconstructed 3D geometry. With the assumption that the object has uniform motion between the captured fringe patterns, a relative phase error between the distorted phase caused by motion and the correct phase is expressed. Then, a linear least-squares fit can be performed between the neighbouring pixels to solve the phase variance caused by motion. This method not only requires more cameras, but also assumes the motion between the fringe patterns is constant.

To increase the measurement accuracy of single-shot FTP, a π phase-shifting FTP has been proposed [98]. Two fringe patterns that are π phase-shifted are used to reconstruct the object. The accuracy is higher than for traditional FTP, but because two fringe patterns are used, this method cannot be used for the measurement of moving objects. Hu and He [99] proposed an improved π phase-shifting FTP algorithm to measure an object moving at a constant speed. In their algorithm, only one fringe pattern is projected onto the object, but the fringe pattern comprises two regions with a π phase-shifting to each other. Two line-scan cameras are used to capture the deformed fringe pattern in the two regions. To find the corresponding points between the two regions, the object must be moved at a constant velocity and the movement direction should be perpendicular to the line-scan direction. A point on the object can be captured twice when moving through the two regions of the fringe patterns. With the two π shifting fringe patterns for one point on the object, the traditional π phase-shifting FTP algorithm is used to reconstruct the object. This system can improve the accuracy of the measurement significantly, but it requires two line-scan cameras and is costly in implementation. The application of this method is limited because the object must be moved as a constant speed and the movement direction should be perpendicular to the line-scan direction of the camera.

High speed equipment has also been used to reconstruct a moving object [100-103]. Wang, *et al*. [104] proposed using a high speed camera at 5,000 frames per second to measure a moving object. With a high speed camera, the object can be considered as stationary during the projection of the phase shifted fringe patterns but this assumption limits the speed of the object movement. The use of high speed equipment means a significant increase in the cost of system implementation.

1.2.3.2 Related work for shadow removal

FPP uses the intensity values of the fringe pattern to reconstruct the object. As the camera and the projector probe the object from different directions, shadow areas will be captured. Because the shadow areas do not contain the information of the fringe patterns, errors will be introduced in the result. Several methods have been proposed to address the effect of shadows.

Skydan, *et al*. [105] used multiple projectors to probe the object from different angles to obtain a shadow-free surface reconstruction. However, the typical PSP system only includes one projector. Zhang [106] proposed using a Gaussian filter to smooth the fringe pattern and then identify invalid points using the monotonicity characteristic of the unwrapped phase map. However, although the Gaussian filter reduces the phase noise, it also introduces distortion to the details of the object surface. Chen, *et al*. [107] proposed a method to identify invalid points by applying a threshold to the least-squares fitting errors in temporal phase unwrapping. However, in the presence of noise, not all invalid points can be identified because some invalid points also have small least-squares fitting errors [108]. Data modulation and intensity modulation of the fringe patterns are also employed to

remove the shadow area in practice [109-111], but there is no effective way to determine the value of the threshold required by the methods.

1.3 Outstanding issues and contributions of the thesis

1.3.1 Outstanding issues

From the literature review in Section 1.2, it can be seen that FPP is one of the most widely used techniques because of its potential for high accuracy, dense resolution and fast speed. The single-shot techniques such as FTP and colour-coded fringe pattern profilometry only employ a single fringe pattern to probe the object. These methods are insensitive to movement of object and are suitable for measuring moving objects in real-time. However, accuracy suffers from the influence of ambient light, variations in the reflectivity of the object surface and cross-talk. To achieve robust and accurate measurement, multiple-shot techniques (e.g., PSP and intensity ratio approaches) can be employed. As more fringe patterns are used, the influence of ambient light and variations in the reflectivity of the object surface can be offset during the calculations. Therefore, these multiple-shot techniques are more robust and able to achieve high accuracy of measurement. However, additional time is required due to the use of the multiple fringe patterns and the object must be kept stationary during the projection and capture of the multiple fringe patterns. When the object moves between the gaps between the capture of the multiple fringe patterns, errors will be introduced [112, 113]. These errors can be remedied by increasing the speed of digital projection and capture [114, 115]. When the speed of the projector and camera are fast enough, the object can be seen as static between the captured fringe patterns. However this usually leads to a significant increase in the hardware cost.

In summary, the outstanding issues for the existing FPP algorithms can be described as follows:

- Using multiple-shot techniques, errors will be introduced in the measurement of moving objects. How does the movement of the object influence the fringe patterns?
- Because the 2D movement of the object does not change the height of the object surface, is it possible to track the movement of the object among the multiple fringe patterns and then reconstruct the 3D shape of the object without the influence caused by the movement?
- In FPP, 3D movement of the object is more complex than 2D because unknown height variations of the object are introduced. What is the influence on the fringe patterns caused by the 3D movement and is it possible to measure the object with multiple-shot techniques and without requiring the height variations of the object to be known beforehand?
- To obtain high-quality reconstruction results, how can the influence caused by the shadow be removed?

1.3.2 Contributions

The objective of this thesis is to develop a new 3D shape measurement system that uses multiple-shot techniques and is not affected by the influence caused by object movement. The contributions of this thesis are as follows:

1. Mathematically described the movement of the object;
2. Analysed the influence on the fringe patterns caused by the movement of the object;

3. According to the different types of movement, proposed several algorithms to improve measurement accuracy when the object is subject to the 2D movement and 3D movement;
4. Proposed a method to remove the points influenced by the shadow on the fringe patterns to obtain a high-quality result;
5. Built a low cost 3D shape measurement system with only one camera and one projector to measure a moving object accurately with high resolution.

1.4 Experimental set-up

In this section, the measurement system used in the experiments for this thesis is presented. The measurement system is based on the system used for FPP. To obtain accurate results, the system is calibrated before measurement. The details are presented below.

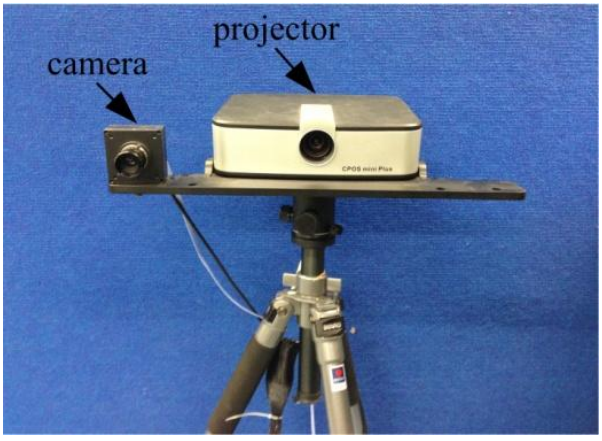

Fig. 1.4. The system set-up used in the experiments.

The measurement system used in this thesis is shown in Fig. 1.4. The system includes a projector (LG-HW300G) with a 1024 pixel × 768 pixel resolution and a camera (Microview-MVC1000SAM-GE30) with a 1280 pixel × 1024 pixel resolution.

As described above, the FPP techniques use the camera and projector to reconstruct the shape of the object based on the triangular relationship. The accuracy of the measurement will be affected by factors such as the focal distances of the camera and the projector, the spatial frequency of the fringe patterns and the parameters of the system geometry. Traditional methods of measurement cannot obtain these factors with high accuracy. The accuracy of the reconstruction depends on the proper calibration of each element used in the FPP system [116]. To calibrate the measurement system, methods based on neural networks [117, 118], bundle adjustment [119, 120] and absolute phase [121] have been developed. In practice, complicated and time-consuming procedures are usually involved.

The system used in this thesis is calibrated using the method proposed by Zhang and Huang [122]. As with the stereo vision system, the FPP system also uses the camera to capture the image of the object. Therefore, the calibration methods used in stereo vision techniques can be used to calibrate the camera in the FPP system. However, because the projector in the FPP system only emits the fringe patterns, the conventional calibration method of stereo vision is invalid for projector calibration. To calibrate the FPP system, the projector is seen as the inverse of the camera and the camera is used to capture the fringe patterns for the projector. In this method, the projector can be calibrated by the method for the camera calibration used in a stereo vision system [122]. The details are described below.

The camera is calibrated first using the well-known method proposed by Zhang [123]. A calibration board shown in Fig. 1.5 is used in our laboratory. There are 11 × 9 circles on the board, for which the relative positions are known with high accuracy. In Zhang's method, the camera is described by a pinhole model, which

includes intrinsic parameters, such as the focal length, principle point and pixel skew factor, and extrinsic parameters, such as the rotation and translation from the world coordinate system to the camera coordinate system. During calibration, the calibration board is moved to at least three positions and captured by the camera. The centres of the circle marks can then be extracted. Because the relative positions of the circles on the calibration board are known, it can be used to build the relationship between the world coordinate system and the camera coordinate system. Then, the intrinsic parameters and extrinsic parameters of the camera can be obtained.

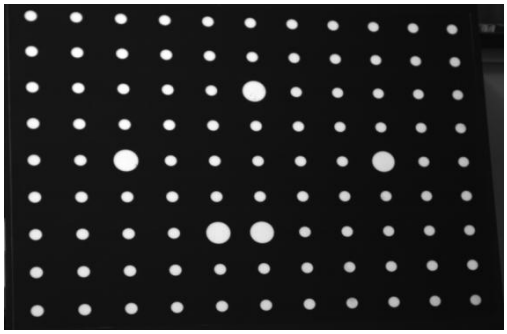

Fig. 1.5. The calibration board.

For the projector calibration, the camera is used to capture images from the projector and then these images are transformed into the projector images so that they are as if captured directly by the DMD of the projector. The projector can then be calibrated by the same method used for the camera calibration.

1.5 Structure of the thesis and conclusion

1.5.1 Structure of the thesis

The thesis is organised as follows:

- Chapter 2 proposes the methodology to improve the accuracy of the 3D shape measurement based on PSP for a rigid object with 2D movement. Using the information on the movement, new expressions of the fringe patterns with the influence of movement are derived. The obtained expressions are then used to reconstruct the object without the influence caused by the 2D movement.
- In Chapter 3, a new algorithm based on the intensity ratio method is proposed to address the errors caused by the 2D movement of the object. The influence on the fringe patterns caused by the 2D movement of the object is analysed and the normalised fringe patterns of the object without movement are estimated. Using the estimated fringe patterns, the object is reconstructed by the traditional intensity ratio method.
- To measure a rigid object with 3D movement, an iterative least-squares method is proposed in Chapter 4. The method is based on PSP and the movement consists of a translation movement in the height direction and a 2D movement in the plane perpendicular to the direction of height. A new model that describes the fringe patterns under the influence of 3D movement of the object is proposed. Because the 3D movement of the object introduces unknown height variations, an iterative least-squares algorithm is applied to estimate the phase value in the proposed method.
- In Chapter 5, a new method is proposed to remove the invalid points in the shadow area on the fringe patterns of PSP. The proposed algorithm maps all the reconstructed results to the DMD plane of the projector. Because only the points reflecting the projected fringe patterns can be used to reconstruct the object, the points in the shadow area will be mapped to an incorrect position

in the DMD plane. A set of rules are then proposed to remove the invalid points caused by the shadow.

- To complete the thesis, Chapter 6 summaries the presented work and proposes the future research directions.

1.5.2 Conclusion

An introduction to 3D shape measurement techniques has been presented and techniques based on FPP have been reviewed in this chapter. Although numerous techniques have been developed and high accuracy measurement can be achieved for stationary objects, it remains extremely difficult to reconstruct a moving object with high accuracy using low cost equipment.

Through analysis of the influence on the fringe patterns caused by the movement of a rigid object, this thesis proposes some approaches to address the above issue based on multiple-shot 3D reconstruction techniques. The proposed methods not only inherit the advantages of the multiple-shot algorithms, such as being robust to ambient light and variance in the reflectively of the object surface, but also overcome the weakness of the invalidity of the moving object measurement.

2 RECONSTRUCTION OF THE OBJECT WITH 2D MOVEMENT BASED ON PSP

2.1 Introduction

Of the different approaches to implementing the FPP technique, PSP is one of the most widely used ones because of its high accuracy and robustness to the influence of ambient light and variations in reflectivity. With the PSP approach, at least three sinusoidal fringe patterns with a certain phase shift from each other are used to probe the object. The 3D information is retrieved by processing the reflected fringe patterns that are acquired by a camera. A fundamental requirement of PSP is that the object must be kept stationary during the projection and acquisition of the multiple fringe patterns. If the object moves, errors will be introduced to the results of the measurement. In many applications, this requirement is difficult to meet. The errors introduced by movement of the object can be remedied by increasing the speed of digital projection and capture, but this usually leads to a significant increase in the hardware cost. Therefore, it is highly desirable to develop a technique for the measurement of a moving object with inexpensive digital projector and camera equipment.

In this chapter, a novel approach to reducing the measurement error arising from the 2D movement of a rigid object is proposed. The proposed algorithm requires the object to be rigid and the movement of the object must be in 2D. The measurement system is static and the speed of the object movement is not required to be constant. The proposed algorithm is based on analysis of the phase maps of the fringe patterns

acquired from the surface of an object that is subjected to 2D movement. Because 2D movement of an object can be modelled by a rotation matrix and a translation vector, the relationship between the phase maps of the fringe patterns can be described the same way. The relationship between the phase maps can then be employed to eliminate the influence of the object movement, thereby achieving accurate 3D shape measurement.

This chapter is organised as follows. Section 2.2 analyses the reason for the error when the object is moved during traditional PSP measurement. A new method is then presented to address the above errors. Next, simulations and experimental results are presented in Section 2.3 to verify the effectiveness of the proposed algorithm. Section 2.4 concludes this chapter.

2.2 Principle of the proposed method based on PSP

The effectiveness of the conventional PSP algorithm presented in Chapter 1 depends on the validity of Eqs. (1.3) and (1.4). In order for Eqs. (1.3) and (1.4) to hold, the phase values of $s_n(x, y)$ and $d_n(x, y)$ must be equally spaced by $2\pi / N$. When the object is kept stationary, the fringe patterns are required to be accurately created and projected. However, when the object is moved during the projection of the multiple fringe patterns, even when the projected fringe patterns are equally spaced, the phase shifts of all the points on the object between the captured fringe patterns of the object are not same. When the object moves, Eqs. (1.3) and (1.4) will be violated, and errors will occur in the measurement.

In order to calculate the phase map of the object with movement, the first task is to describe the movement of the object. The surface shape of an object is still described

by the height distribution $h(x, y)$, and it is subject to a 2D movement in the $x-y$ plane. Due to the movement, a point (x, y) on the object surface will be moved to the point (u, v) following the relationship below

$$\begin{bmatrix} x \\ y \end{bmatrix} = \mathbf{R}\begin{bmatrix} u \\ v \end{bmatrix} + \mathbf{T}, \qquad \begin{bmatrix} u \\ v \end{bmatrix} = \bar{\mathbf{R}}\begin{bmatrix} x \\ y \end{bmatrix} + \bar{\mathbf{T}}. \tag{2.1}$$

where $\mathbf{R}$, $\bar{\mathbf{R}}$, $\mathbf{T}$ and $\bar{\mathbf{T}}$ are referred to as rotation matrices and translation vectors which describe the relationship between (x, y) and (u, v), and they are given by

$$\mathbf{R} = \begin{bmatrix} r_{11} & r_{12} \\ r_{21} & r_{22} \end{bmatrix}, \qquad \mathbf{T} = \begin{bmatrix} t_1 \\ t_2 \end{bmatrix}, \tag{2.2}$$

$$\bar{\mathbf{R}} = \begin{bmatrix} \bar{r}_{11} & \bar{r}_{12} \\ \bar{r}_{21} & \bar{r}_{22} \end{bmatrix}, \qquad \bar{\mathbf{T}} = \begin{bmatrix} \bar{t}_1 \\ \bar{t}_2 \end{bmatrix}. \tag{2.3}$$

The relationship between $(\mathbf{R}, \mathbf{T})$ and $(\bar{\mathbf{R}}, \bar{\mathbf{T}})$ can be expressed as

$$\bar{\mathbf{R}} = \mathbf{R}^{-1}, \qquad \bar{\mathbf{T}} = -\mathbf{R}^{-1}\mathbf{T}. \tag{2.4}$$

As the shape of the object surface does not change, the height distribution of the object surface after movement becomes

$$\tilde{h}_{x-y}(u, v) = h_{x-y}(x, y) \tag{2.5}$$

where the subscript $x-y$ denotes the coordinate system in which the functions are defined. From Eq. (2.1), we have

$$\tilde{h}_{x-y}(u, v) = h_{x-y}(x, y) = h_{x-y}(f(u, v), g(u, v)) \tag{2.6}$$

where

$$f(u,v) = r_{11}u + r_{12}v + t_1, \qquad g(u,v) = r_{21}u + r_{22}v + t_2. \tag{2.7}$$

Without loss of generality, (u,v) can be replaced by (x,y), yielding the following:

$$\tilde{h}_{x-y}(x,y) = h_{x-y}(f(x,y), g(x,y)) \tag{2.8}$$

As mentioned above, the movement of the object during the measurement will cause variance in the phase map of reflected fringe patterns, which then results in unequally spaced phase shift among the fringe patterns. This is the fundamental reason of the errors caused by the movement. To address this problem, the relationship between the movement of object and phase maps is analysed below.

For the N-step PSP, the fringe patterns on the reference plane and object without movement are described in Eqs. (1.1) and (1.2), respectively. After the movement of the object, the fringe patterns of the object become the following:

$$\tilde{d}^n_{x-y}(x,y) = a + b\cos(\phi(x,y) + \tilde{\Phi}(x,y) + \frac{2\pi(n-1)}{N}) \tag{2.9}$$

where $\tilde{\Phi}(x,y)$ is the phase difference at point (x,y) after movement. From Eq. (1.9) we can see a corresponding relationship between the height distribution and the phase difference, and hence a similar relationship to Eq. (2.8) should also hold for the phase differences before and after the movement:

$$\tilde{\Phi}(x,y) = \Phi(f(x,y), g(x,y)) \tag{2.10}$$

Substituting Eq. (2.10) into Eq. (2.9) yields the following:

$$\tilde{d}^n_{x-y}(x,y) = a + b\cos(\phi(x,y) + \Phi(f(x,y), g(x,y)) + \frac{2\pi(n-1)}{N}) \tag{2.11}$$

Note that Eq. (2.11) is defined in $x-y$ coordinate system. Now let us consider Eq. (2.11) in a new coordinate system $\xi-\eta$, which has the relationship to the $x-y$ system as follows:

$$\begin{bmatrix} x \\ y \end{bmatrix} = \bar{\mathbf{R}} \begin{bmatrix} \xi \\ \eta \end{bmatrix} + \bar{\mathbf{T}} \tag{2.12}$$

In $\xi-\eta$ coordinate system, Eq. (2.11) becomes

$$\begin{aligned} \tilde{d}^n_{\xi-\eta}(\xi,\eta) &= \tilde{d}^n_{x-y}(\bar{f}(\xi,\eta), \bar{g}(\xi,\eta)) \\ &= a + b\cos(\phi(\bar{f}(\xi,\eta), \bar{g}(\xi,\eta)) + \Phi(\xi,\eta) + \frac{2\pi(n-1)}{N}) \end{aligned} \tag{2.13}$$

where, from Eq. (2.3) we have

$$\bar{f}(\xi,\eta) = \bar{r}_{11}\xi + \bar{r}_{12}\eta + \bar{t}_1, \qquad \bar{g}(\xi,\eta) = \bar{r}_{21}\xi + \bar{r}_{22}\eta + \bar{t}_2. \tag{2.14}$$

Equation (2.13) is the expression of the fringe patterns in the $\xi-\eta$ coordinate system. Obviously, when $(\bar{\mathbf{R}}, \bar{\mathbf{T}})$ are available, $\tilde{d}^n_{\xi-\eta}(\xi,\eta)$ can be obtained. As Eq. (2.13) is valid for arbitrary 2D movement, it can be rewritten in a general form as follows:

$$\begin{aligned} \tilde{d}^n(x,y) &= \tilde{d}^n_{x-y}(\bar{f}(x,y), \bar{g}(x,y)) \\ &= a + b\cos(\phi(\bar{f}(x,y), \bar{g}(x,y)) + \Phi(x,y) + \frac{2\pi(n-1)}{N}) \end{aligned} \tag{2.15}$$

The above can be extended to N-step PSP. Due to the movement of the object, the fringe patterns on the object can be obtained as follows:

$$\begin{cases} \tilde{d}^1(x,y) = a + b\cos(\phi(x,y) + \Phi(x,y)) \\ \tilde{d}^2(x,y) = a + b\cos(\phi(\bar{f}_2(x,y), \bar{g}_2(x,y)) + \Phi(x,y) + 2\pi/N) \\ \vdots \\ \tilde{d}^N(x,y) = a + b\cos(\phi(\bar{f}_N(x,y), \bar{g}_N(x,y)) + \Phi(x,y) + 2\pi(N-1)/N) \end{cases} \tag{2.16}$$

where $\tilde{d}^1(x,y)$ is the first and original fringe patterns; $\tilde{d}^n(x,y) \quad n = 2,3,...,N$ can be obtained from the captured fringe patterns $\tilde{d}^n_{x-y}(x,y)$ by Eq. (2.15). In other words, the left hand side of Eq. (2.16) is available. The phase map of the reference plane $\phi(x,y)$ can be calculated by Eq. (1.3). $(\bar{f}_n(x,y), \bar{g}_n(x,y)) \quad n = 2,3,...,N$ are also known for given rotation matrices and translation vectors. Solving Eq. (2.16), a wrapped $\Phi(x,y)$ can be obtained as follows:

$$\Phi(x,y) = \arctan\frac{D_A - D_B}{D_C - D_D} \tag{2.17}$$

where

$$D_A = \sum_{n=1}^{N} \tilde{d}^n(x,y)\cos\frac{2\pi(n-1)}{N} \sum_{n=1}^{N} \cos(\phi(\bar{f}_n(x,y), \bar{g}_n(x,y)) + \frac{2\pi(n-1)}{N}) \sin\frac{2\pi(n-1)}{N},$$

(2.18)

$$D_B = \sum_{n=1}^{N} \tilde{d}^n(x,y)\sin\frac{2\pi(n-1)}{N} \sum_{n=1}^{N} \cos(\phi(\bar{f}_n(x,y), \bar{g}_n(x,y)) + \frac{2\pi(n-1)}{N}) \cos\frac{2\pi(n-1)}{N},$$

(2.19)

$$D_C = \sum_{n=1}^{N} \tilde{d}^n(x,y)\cos\frac{2\pi(n-1)}{N} \sum_{n=1}^{N} \sin(\phi(\bar{f}_n(x,y), \bar{g}_n(x,y)) + \frac{2\pi(n-1)}{N}) \sin\frac{2\pi(n-1)}{N},$$

(2.20)

$$D_D = \sum_{n=1}^{N} \tilde{d}^n(x,y) \sin\frac{2\pi(n-1)}{N} \sum_{n=1}^{N} \sin(\phi(\bar{f}_n(x,y), \bar{g}_n(x,y)) + \frac{2\pi(n-1)}{N}) \cos\frac{2\pi(n-1)}{N}.$$

(2.21)

In Eqs. (2.18)-(2.21), when $n=1$,

$$\bar{f}_1(x,y) = x, \qquad \bar{g}_1(x,y) = y. \tag{2.22}$$

As the rotation matrices and translation vectors are assumed to be known in the above, the last question is how to determine them. Various approaches have been proposed to solve this problem [124-126]. As only 2D movement is considered and the object does not have deformation, the singular value decomposition (SVD) method [125] is chosen and the details are described as follows.

Assume that there are two sets of corresponding points and their coordinates are

$$\mathbf{P_j} = \begin{bmatrix} x_j \\ y_j \end{bmatrix}, \qquad \mathbf{Q_j} = \begin{bmatrix} u_j \\ v_j \end{bmatrix}, \qquad j = 1,2,...,J. \tag{2.23}$$

where $\mathbf{P_j}$ are the points on the object before movement and $\mathbf{Q_j}$ are the corresponding points on the object after movement; J is the number of the corresponding points. With Eq. (2.1), $\mathbf{P_j}$ and $\mathbf{Q_j}$ are related by the following:

$$\mathbf{Q_j} = \bar{\mathbf{R}}\mathbf{P_j} + \bar{\mathbf{T}} + \mathbf{V_j} \tag{2.24}$$

where $\mathbf{V_j}$ is a noise vector. In order to determine the rotation matrix $\bar{\mathbf{R}}$ and translation vector $\bar{\mathbf{T}}$, we define the following:

$$\mathbf{P}' = \frac{1}{J}\sum_{j=1}^{J}\mathbf{P_j}, \qquad \mathbf{P_{cj}} = \mathbf{P_j} - \mathbf{P}', \tag{2.25}$$

$$\mathbf{Q}' = \frac{1}{J}\sum_{j=1}^{J}\mathbf{Q_j}, \qquad \mathbf{Q_{cj}} = \mathbf{Q_j} - \mathbf{Q}'. \tag{2.26}$$

Then $\bar{\mathbf{R}}$ and $\bar{\mathbf{T}}$ are obtained by minimising the square error below:

$$\begin{aligned}\Sigma^2 &= \sum_{j=1}^{J}\left\|\mathbf{Q_j} - \hat{\bar{\mathbf{R}}}\mathbf{P_j} - \hat{\bar{\mathbf{T}}}\right\|^2 \\ &= \sum_{j=1}^{J}\left\|\mathbf{Q_{cj}} - \hat{\bar{\mathbf{R}}}\mathbf{P_{cj}}\right\|^2 \\ &= \sum_{j=1}^{J}(\mathbf{Q_{cj}}^{\mathbf{T}}\mathbf{Q_{cj}} + \mathbf{P_{cj}}^{\mathbf{T}}\mathbf{P_{cj}} - 2\mathbf{Q_{cj}}^{\mathbf{T}}\hat{\bar{\mathbf{R}}}\mathbf{P_{cj}})\end{aligned} \tag{2.27}$$

Equation (2.27) is minimised when the last term is maximised, which is equivalent to maximising the trace of $(\hat{\bar{\mathbf{R}}}, \mathbf{H})$, where $\mathbf{H}$ is a correlation matrix defined by

$$\mathbf{H} = \sum_{j=1}^{J}\mathbf{P_{cj}}\mathbf{Q_{cj}}^{\mathbf{T}} \tag{2.28}$$

Assume the singular value decomposition of $\mathbf{H}$ is described by $\mathbf{H} = \mathbf{U}\Lambda\mathbf{V}^T$, where $\mathbf{U}$, Λ and $\mathbf{V}$ are three matrices. The optimal rotation matrix, $\hat{\bar{\mathbf{R}}}$, that maximises the trace is the following:

$$\hat{\bar{\mathbf{R}}} = \mathbf{V}\mathbf{U}^T \tag{2.29}$$

and the translation vector is determined as

$$\hat{\bar{\mathbf{T}}} = \mathbf{Q}' - \hat{\bar{\mathbf{R}}}\mathbf{P}' \tag{2.30}$$

Based on the above, the proposed technique can be implemented by the steps below:

Step 1: Based on the *N*-step PSP, *N* fringe patterns are projected onto the object surface, and $\tilde{d}^n_{x-y}(x,y) \quad n=1,2,3,...,N$ are captured;

Step 2: Determine the rotation matrix and translation vector for the movement of object when each of the fringe patterns is captured;

Step 3: With the rotation matrix and translation vector, Eq. (2.15) is used to calculate $\tilde{d}^n(x,y)$;

Step 4: Determine the phase difference $\Phi(x,y)$ with Eq. (2.17);

Step 5: Calculate the 3D shape of object by Eq. (1.9).

2.3 Simulations and experiments

Simulations are carried out to verify the performance of the proposed algorithm. In the simulations, three-step PSP algorithm is used and the object is a hemisphere. When the object is stationary, the reconstructed results are shown in Fig. 2.1. Next we carry out the simulations in which the object moves at the second step and the third step of PSP. Note that in the simulation, the rotation matrices and translation vectors are known a priori, and hence the proposed technique is applied directly to reconstruct the object.

In the first simulation the hemisphere moves in the right bottom direction as indicated by the arrow in Fig. 2.2(b), and the movement distance is 10 mm and 15 mm in the second step and third step respectively. Figures 2.2(a) and 2.2(b) are the reconstructed results using the traditional PSP directly. Figure 2.2(c) is the cross-section of the object at the dashed line in Fig. 2.2(b). There are obvious errors in the result.

When the proposed algorithm is applied, the object can be reconstructed successfully as shown in Figs. 2.3(a) and 2.3(b). Figure 2.3(c) is the cross-section of the object on the dashed line in Fig. 2.3(b). The surface becomes smooth by using the proposed algorithm.

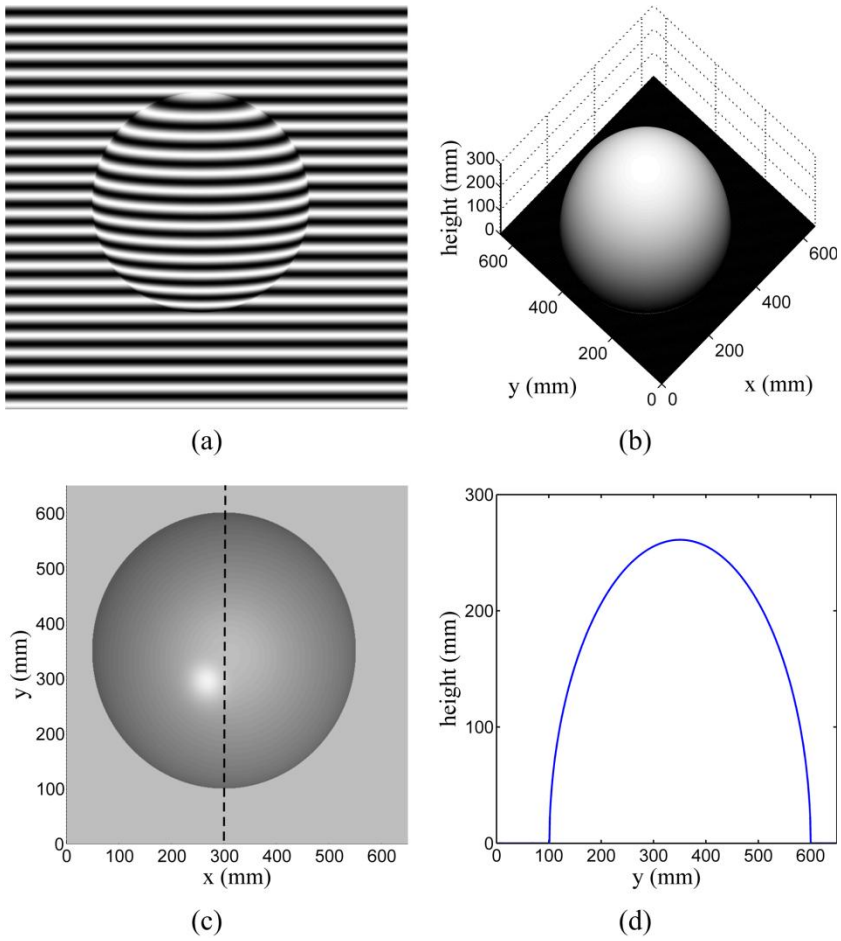

Fig. 2.1. Hemisphere simulation. (a) Fringe patterns of the hemisphere for the first step of PSP; (b) Reconstructed result by Mesh display; (c) Front view of Fig. 2.1(b); (d) The cross-section of the dashed line in Fig. 2.1(c) where x=300 mm.

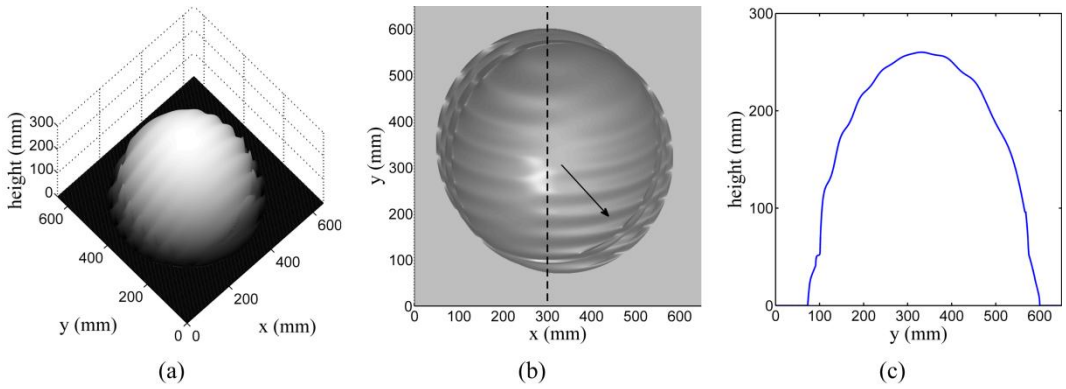

Fig. 2.2. Reconstructed results of traditional PSP when the object has oblique movement. (a) Reconstructed result by Mesh display; (b) Front view of Fig. 2.2(a); (c) The cross-section of the dashed line in Fig. 2.2(b) where x=300 mm.

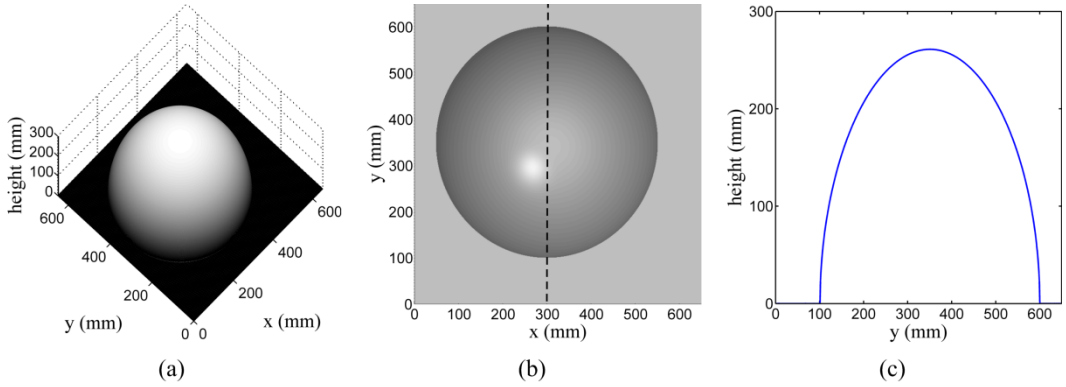

Fig. 2.3. Reconstructed results of the proposed algorithm when the object has oblique movement. (a) Reconstructed result by Mesh display; (b) Front view of Fig. 2.3(a); (c) The cross-section of the dashed line in Fig. 2.3(b) where x=300 mm.

Now we consider the case when the object is rotated clockwise around the axis through point (x,y), e.g. (0,600) perpendicular to x-y plane as shown by the arrow in Fig. 2.4(b). For the step 2 and step 3 of the PSP, the rotation angle is 0.213 rad and 0.311 rad respectively. Figures 2.4(a) and 2.4(b) are the reconstructed results when the traditional PSP is used. Figure 2.4(c) shows the cross-section of the dashed line in Fig. 2.4(b). Clearly, the movement causes distortion in the traditional PSP.

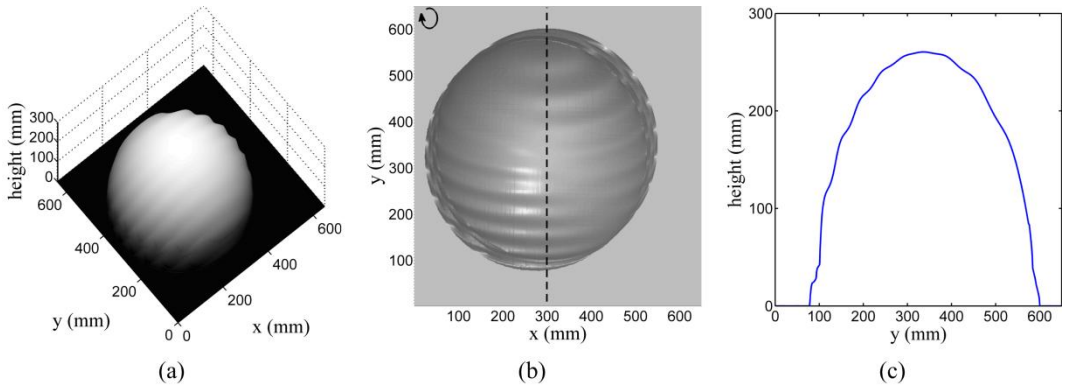

Fig. 2.4. Reconstructed results of the traditional PSP when the object has rotation movement. (a) Reconstructed result by Mesh display; (b) Front view of Fig. 2.4(a); (c) The cross-section of the dashed line in Fig. 2.4(b) where x=300 mm.

Figures 2.5(a) and 2.5(b) are the reconstructed results obtained by the proposed algorithm when the object is subject to the above rotation. The smooth surface indicates that the object is well reconstructed.

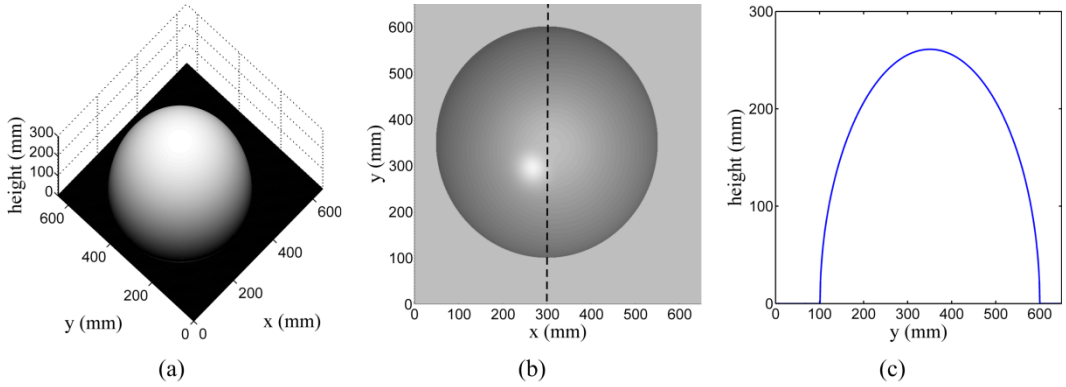

Fig. 2.5. Reconstructed results of the proposed algorithm when the object has rotation movement. (a) Reconstructed result by Mesh display; (b) Front view of Fig. 2.5(a); (c) The cross-section of the dashed line in Fig. 2.5(b) where x=300 mm.

In the experiments, a plastic mask is used as the object. The size of the mask is approximate 250 mm × 250 mm. The measurement system requires the camera to be parallel with the reference plane. Before measurement, the system is calibrated. During the experiment, the object is controlled by the optical instrument to

implement the expect movement. In order to calculate the rotation matrix and translation vector, we placed three marks on the mask (shown in Fig. 2.6) to indicate the corresponding points on the multiple fringe patterns. For achieving high accuracy in determining the rotation matrix and translation vector, the positions of the corresponding points must be accurately extracted. In order to achieve this, marks are circular with diameter of 15 mm, and the centers of these circles are employed as the corresponding points in Eq. (2.23). When multiple fringe patterns are acquired, we firstly extract a set of points on the edge of the circles using the approach presented in [127], and the accuracy can be sub-pixel, that is, <0.5 mm. Then least-squares curve-fitting is employed to extract the centers of the circles, and the accuracy should also be <0.5 mm. Such accuracy enables us to have accurate estimation of the rotation matrix and translation vector using the algorithm described in Eqs. (2.23)-(2.30).

Fig. 2.6. Object with marks.

In the first experiment, the conventional three-step PSP algorithm is used. When the object is stationary, the reconstructed results are shown in Fig. 2.7. Figure 2.7(a) is the captured fringe patterns for the first step of PSP. Figures 2.7(b) and 2.7(c) are the

reconstructed results of the mask. Figure 2.7(d) is the cross-section of the dashed line in Fig. 2.7(c) where x=115 mm. The results show that good reconstruction can be obtained.

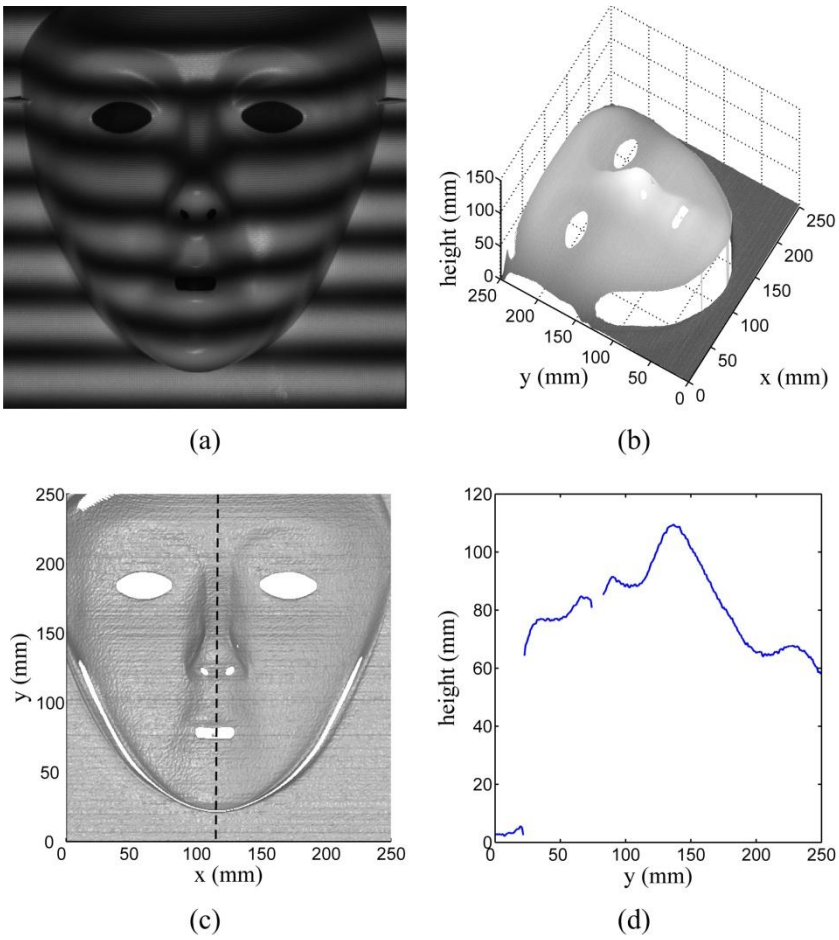

Fig. 2.7. Reconstructed results of the traditional PSP when the object is stationary. (a) Fringe patterns of the first step of PSP; (b) Reconstructed result by Mesh display; (c) Front view of Fig. 2.7(b); (d) The cross-section of the dashed line in Fig. 2.7(c) where x=115 mm.

In the second experiment, the object is moved in the direction of the arrow as shown in Fig. 2.8(b) at the second and third step of PSP. The movement distance is 11 mm for the second step and 14 mm for the third step of PSP. Figures 2.8(a) and 2.8(b) are the measurement result of the traditional PSP algorithm. Figure 2.8(a) is the mesh display of the reconstructed result. Figure 2.8(b) is the front view of Fig.

2.8(a). Figure 2.8(c) shows the cross-section of the dashed line in Fig. 2.8(b) where x=115 mm. The errors in the reconstructed result are obvious and significant.

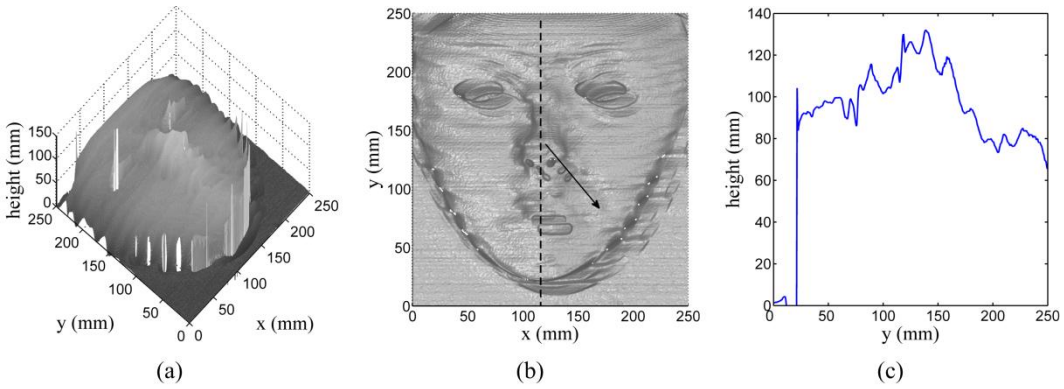

Fig. 2.8. Reconstructed results of the traditional PSP when the object has oblique movement. (a) Reconstructed result by mesh display; (b) Front view of Fig. 2.8(a); (c) The cross-section of the dashed line in Fig. 2.8(b) where x=115 mm.

Then the proposed algorithm is examined to the case where the object is moved by the same amount as above. The reconstructed results in Fig. 2.9 show that significant improvement was achieved.

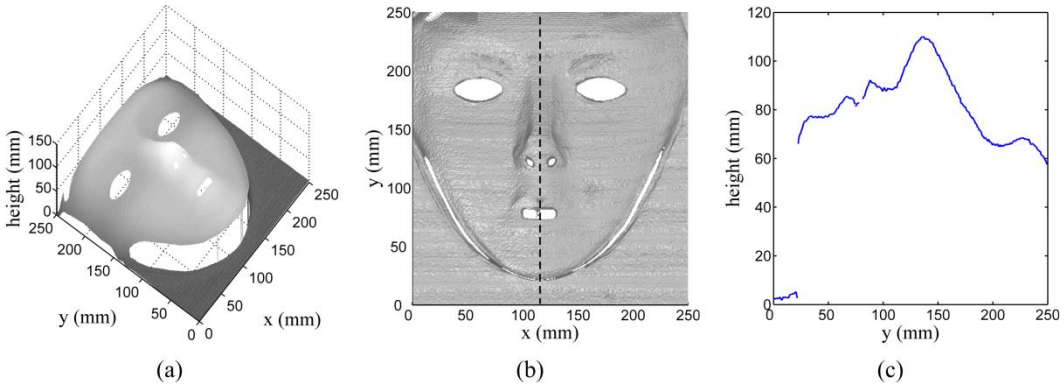

Fig. 2.9. Reconstructed results of the proposed algorithm when the object has oblique movement. (a) Reconstructed result by mesh display; (b) Front view of Fig. 2.9(a); (c) The cross-section of the dashed line in Fig. 2.9(b) where x=115 mm.

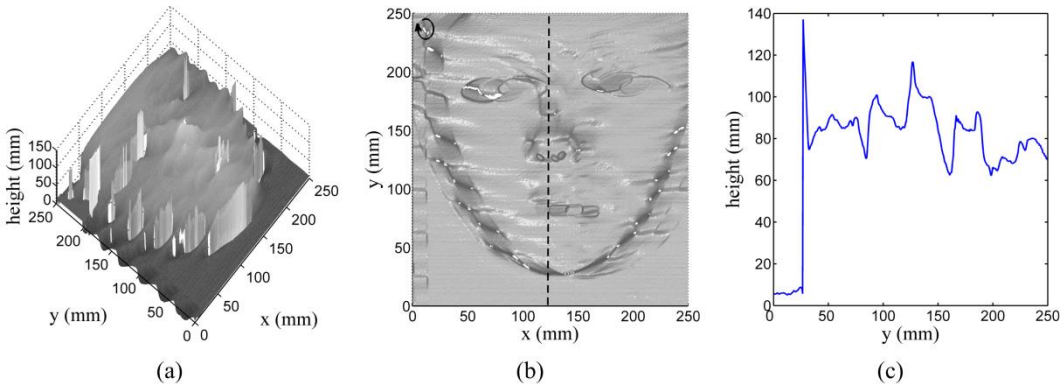

Fig. 2.10. Reconstructed results of the traditional PSP when the object has rotation movement. (a) Reconstructed result by mesh display; (b) Front view of Fig. 2.10(a); (c) The cross-section of the dashed line in Fig. 2.10(b) where x=120 mm.

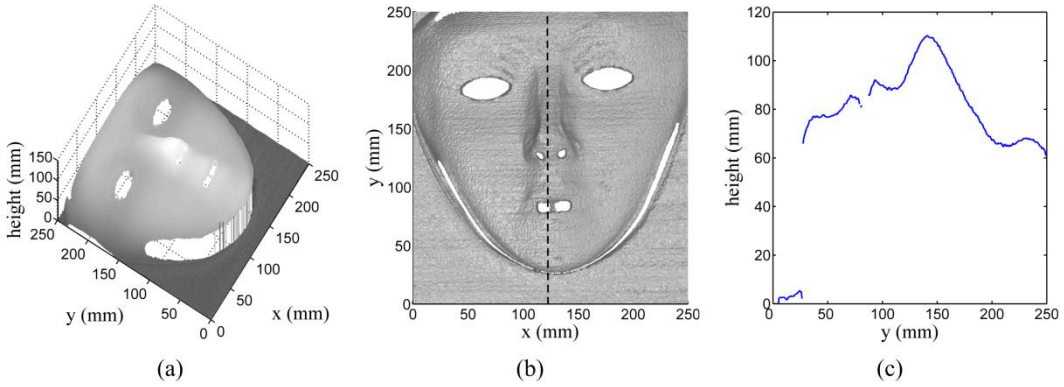

Fig. 2.11. Reconstructed results of the proposed algorithm when the object has rotation movement. (a) Reconstructed result by mesh display; (b) Front view of Fig. 2.11(a); (c) The cross-section of the dashed line in Fig. 2.11(b) where x=120 mm.

Table 2.1. The RMS measurement error of the mask

Movement type	RMS error (traditional PSP)	RMS error (the proposed algorithm)
Oblique	57.276 mm	0.081 mm
Rotation	68.371 mm	0.076 mm

In the final experiment, the object is rotated clockwise around the top left corner (as shown in Fig. 2.10(b)) from the second step to the third step of PSP. The rotation angle is 0.0387 rad in the second step and 0.0446 rad in the third step. The results with the traditional three-step PSP are shown in Figs. 2.10(a)-2.10(c), which are significantly distorted in contrast to the original mask.

The results with the proposed approach are shown in Figs. 2.11(a) and 2.11(b). The surface of the mask is well reconstructed and the cross-section of the dashed line in Fig. 2.11(b) is also smooth. The results are much better than those in Fig. 2.10.

In order to evaluate the performance improvement of the proposed technique over the traditional PSP, we also calculated the root mean square (RMS) measurement error for the experimental results presented above on the mask. As the true shape of the mask is not known, the measurement result in Fig. 2.7 (i.e., the mask is kept stationary) is used as the reference. The RMS errors with respect to Fig. 2.7 of the cases considered above are obtained in Table 2.1. It is seen that, without the proposed algorithm, the RMS error is 57.27 mm and 68.37 mm respectively. When the proposed technique is employed, the RMS error becomes 0.081 mm and 0.076 mm, indicating a significant reduction in the RMS error and thus significant improvement in measurement accuracy.

2.4 Conclusion

In this chapter, a new approach has been presented to achieve accurate 3D shape measurement of a moving object using PSP. The proposed algorithm inherits the advantage of robustness of PSP and enables the accurate measurement of moving object using inexpensive equipment. As the proposed method tracks the object movement and PSP method is employed, the reconstructed result is not affected by

the surface property of the object such as reflection variations. The proposed technique consists of two steps. Firstly, the rotation matrix and the translation vector describing the 2D movement of the object are estimated from the multiple fringe patterns. Secondly, the expressions of the fringe patterns acquired from the object that is subject to 2D movement are derived. Based on these expressions, the phase maps of the fringe patterns of the moving object can be obtained. These are used to yield an accurate reconstruction of the 3D shape of the object. The performance of the proposed algorithm has been verified by simulations and experiments.

3 RECONSTRUCTION OF THE OBJECT WITH 2D MOVEMENT BASED ON INTENSITY RATIO METHOD

3.1 Introduction

The algorithm described in Chapter 2 can reconstruct the moving object accurately. However, the calculation burden for the phase value is big. The intensity ratio approach proposed by Jia, *et al*. [40, 69] reconstructs an object using the projection of multiple triangular patterns. Instead of calculating the phase map, as in traditional PSP, this technique reconstructs the object by computing the intensity ratio from the captured triangular fringe patterns. Because calculation of the intensity ratio does not involve the arctangent function, the computational burden of the intensity ratio method is much less than for the calculation of the phase map [41]. However, as with all multiple-shot techniques, the intensity ratio approach also requires that the object be kept stationary during the projection and acquisition of the multiple triangular patterns. When the object moves, errors will occur and there is no technique to address the problem yet.

Inspired by the method described in Chapter 2, this chapter proposes a new approach to reduce the measurement error of the intensity ratio approach that arises from the movement of an object. The system setup is as same as the one used in Chapter 2 and the object movement is also controlled by the optical instruments. We still consider that the rigid object is subject to 2D movement that can be described by a rotation matrix and translation vector. In the proposed method, the rotation matrix and translation vector are acquired in real-time and are incorporated into new

expressions for the fringe patterns that are acquired from the object. These new expressions are then employed to create a new formulation of the 3D shape of the object in motion. Because of the proposed method tracks the object frame by frame, the reconstructed result will not be affected by the surface property of the object. Experimental results are also presented to validate the proposed approach.

This chapter is organised as follows. Section 3.2 describes the derivation of the method that addresses the error in the intensity ratio method that is caused by 2D movement. Section 3.3 presents the experimental result to verify the proposed algorithm, and Section 3.4 concludes this chapter.

3.2 Principle of the proposed method based on intensity ratio method

The principle of the traditional intensity ratio method is described in Chapter 1. In order to reduce the error caused by the object movement, we need to figure out how the movement influences the fringe patterns acquired from the object surface. Same with the description in Chapter 2, we still assume that the object is subject to a 2D movement on the $x-y$ plane. $h(x,y)$ is still used as the height distribution before movement and $\tilde{h}(x,y)$ is the height distribution after movement; the 2D movement is still described by the rotation matrices and translation vector $\mathbf{R}$, $\bar{\mathbf{R}}$, $\mathbf{T}$ and $\bar{\mathbf{T}}$. Then, we can obtain the relationship between $h(x,y)$ and $\tilde{h}(x,y)$ as:

$$\tilde{h}_{x-y}(x,y) = h_{x-y}(f(x,y), g(x,y)) \tag{3.1}$$

where $f(x,y)$ and $g(x,y)$ are defined in Eq. (2.7).

Assume $p(x, y)$ is one triangular fringe pattern from the reference plane and the corresponding fringe pattern on the object can be described by $q(x, y)$. According to the model described in [128], the deformed fringe pattern $q(x, y)$ is a shifted version of $p(x, y)$:

$$q(x, y) = p(x - u(x, y), y) \tag{3.2}$$

where $u(x, y)$ is the shift function which varies with the height of the object. The height distribution of the object is given by

$$h(x, y) = \frac{l_0 u(x, y)}{u(x, y) + d_0} \tag{3.3}$$

Corresponding to Eq. (3.2), the fringe patterns of the object with movement can be expressed as following:

$$\tilde{q}_{x-y}(x, y) = p(x - \tilde{u}(x, y), y) \tag{3.4}$$

where $\tilde{q}_{x-y}(x, y)$ is the fringe patterns of object with movement; $\tilde{u}(x, y)$ is the shift function of object with movement. From Eq. (3.3) we can see a corresponding relationship between the height distribution and the shift function, and hence a similar relationship to Eq. (3.1) should also hold for the shift function without and with movement:

$$\tilde{u}(x, y) = u(f(x, y), g(x, y)) \tag{3.5}$$

Substituting Eq. (3.5) into Eq. (3.4) yields the following:

$$\tilde{q}_{x-y}(x, y) = p(x - u(f(x, y), g(x, y)), y) \tag{3.6}$$

Note Eq. (3.6) is defined in $x-y$ coordinate system. Now let us consider Eq. (3.6) in a new coordinate system $\xi-\eta$, which has the relationship to the $x-y$ system as described in Eq. (2.12). In $\xi-\eta$ coordinate system, Eq. (3.6) becomes

$$\tilde{q}_{\xi-\eta}(\xi,\eta)=\tilde{q}_{x-y}(\bar{f}(\xi,\eta),\bar{g}(\xi,\eta))=p(\bar{f}(\xi,\eta)-u(\xi,\eta),\bar{g}(\xi,\eta)) \tag{3.7}$$

where $\bar{f}(\xi,\eta)$ and $\bar{g}(\xi,\eta)$ are defined in Eq. (2.14).

Equation (3.7) is the expression of the fringe patterns in the $\xi-\eta$ coordinate system. When $(\bar{\mathbf{R}},\bar{\mathbf{T}})$ are available, $\tilde{q}_{\xi-\eta}(\xi,\eta)$ can be obtained. As Eq. (3.7) holds for arbitrary 2D movement, it can be rewritten in a general form as follows:

$$\tilde{q}(x,y)=p(\bar{f}(x,y)-u(x,y),\bar{g}(x,y)) \tag{3.8}$$

Equation (3.8) reveals the influence of the object movement on the fringe patterns. Obviously, direct use of these patterns in the intensity ratio method in Eqs. (1.10) and (1.12) will result in measurement error. However, when $\bar{f}(x,y)$ and $\bar{g}(x,y)$ are available, Eq. (3.8) can also be utilised to estimate the fringe patterns without movement. Instead of the fringe patterns acquired, these estimated fringe patterns will be used to compute the intensity ratios, which will lead to reduction of the measurement error. This is the basic idea of the proposed approach.

In order to estimate the fringe patterns without movement, we firstly normalise the fringe patterns from the reference plane based on the peak points $p_{\max}(x,y)$ and the bottom points $p_{\min}(x,y)$. Figure 3.1(a) shows an example of the normalised fringe pattern $p_0(x,y)$ with its value falling within the range from 0 to 1. Then we convert the normalised pattern into a monotonically increasing one $p_r(x,y)$ as shown in Fig.

3.1(b). $p_r(x, y)$ ranges from 0 to 2. Finally, we unwrap the results to yield the form monotonically increasing over the whole image space, as shown in Fig. 3.1(c).

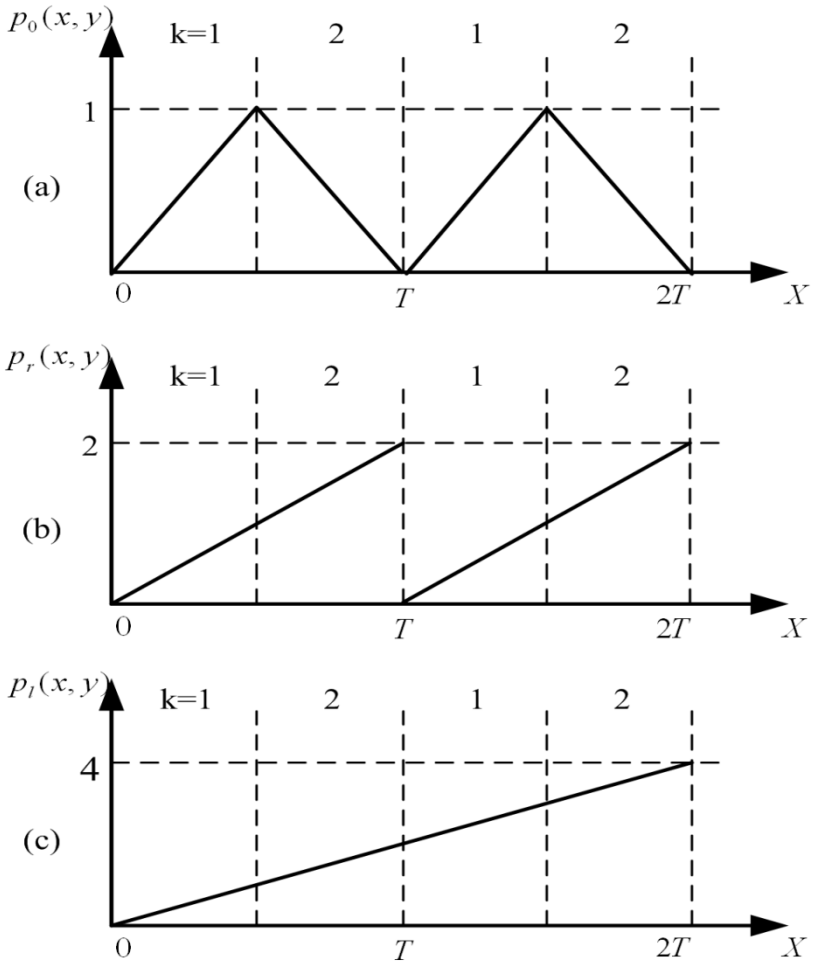

Fig. 3.1. Transform of the triangular fringe patterns: (a) cross-section of the normalised triangular fringe patterns; (b) cross-section of the fringe pattern ramp; (c) cross-section of the unwrapped fringe patterns.

Because the fringe patterns on the object and reference plane satisfy Eq. (3.2) and Eq. (3.8), the unwrapped fringe patterns should also satisfy the same relationship. As $p_l(x, y)$ is a linear function with respect to x, we have

$$q_l(x, y) = p_l(x - u(x, y), y) = p_l(x, y) + p_l(-u(x, y), y) \tag{3.9}$$

and

$$\begin{aligned}\tilde{q}_l(x,y) &= p_l(\bar{f}(x,y) - u(x,y), \bar{g}(x,y)) \\ &= p_l(\bar{f}(x,y), \bar{g}(x,y)) + p_l(-u(x,y), \bar{g}(x,y)).\end{aligned} \tag{3.10}$$

where $q_l(x,y)$ and $\tilde{q}_l(x,y)$ are the unwrapped fringe patterns of object without movement and with movement respectively.

For the vertical fringe patterns used, the intensity values are constant with respect to y direction:

$$p_l(-u(x,y), y) = p_l(-u(x,y), \bar{g}(x,y)) \tag{3.11}$$

Substituting Eq. (3.9) and Eq. (3.11) into Eq. (3.10), we have the following:

$$q_l(x,y) = \tilde{q}_l(x,y) - p_l(\bar{f}(x,y), \bar{g}(x,y)) + p_l(x,y) \tag{3.12}$$

Equation (3.12) can be used to estimate the unwrapped fringe patterns from the object without movement.

In order to have the triangular fringe patterns required for computation of intensity ratio requires, $q_l(x,y)$ is wrapped based on the inverse processes shown in Fig. 3.1, yielding estimation of the normalised triangular fringe patterns of object without movement $q_0(x,y)$.

In summary, based on the derivation above, the proposed approach can be implemented by the following steps:

Step 1: Project N fringe patterns on to the surface of the object and then, normalise and unwrap the fringe patterns acquired from both the object surface and the reference plane.

Step 2: Calculate the rotation matrices and translation vectors for the movement of object when each fringe pattern captured. Note that we can use the same approach as described in Chapter 2.

Step 3: With the rotation matrix and translation vector, use Eq. (3.12) to determine the estimation of the unwrapped fringe patterns from the object without movement;

Step 4: Construct the estimation of triangular patterns from the object without movement.

Step 5: Construct the 3D shape of the object using intensity ratio-to-shape conversion relationship in Eq. (1.12).

3.3 Experiments

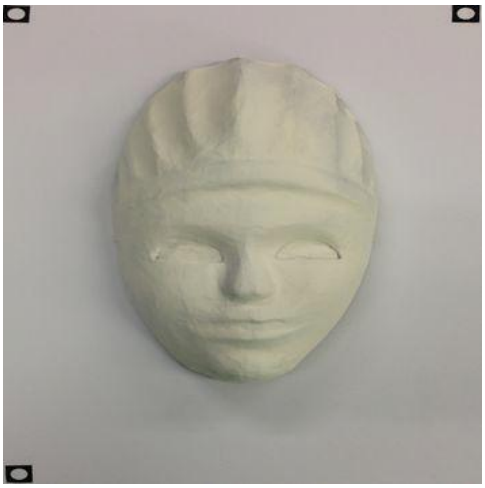

Fig. 3.2. The mask with the circle marks.

A mask is measured to verify the proposed algorithm in the experiment. The size of the mask is approximate 130 mm × 280 mm and five-step intensity ratio method is used to reconstruct the object. Similar to the method described in Chapter 2, three circle marks as shown in Fig. 3.2 are used to calculate the rotation matrix and translation vector. When the multiple fringe patterns are captured, the locations of the center of the circle marks are extracted, which are used as the corresponding points in the least-squares fitting algorithm described in [125] for determining the rotation matrix and translation vector.

In the first experiment, the traditional five-step intensity ratio method described in [40] is used and the object is kept stationary, and the reconstructed 3D shape is shown in Fig. 3.3. Figure 3.3(a) is the triangular fringe pattern for the first step. Figure 3.3(b) is the front view of the reconstructed result and Fig. 3.3(c) is the mesh display of the result. The results clearly show that the traditional intensity ratio method works well when the object is kept stationary.

Fig. 3.3. Reconstructed result of the traditional triangular pattern phase-shifting profilometry when the object is stationary: (a) the triangular fringe patterns of the first step; (b) the front view of the reconstructed result of the object; (c) the mesh display of the reconstructed result of the object.

In the second experiment, we still use the traditional intensity ratio method, but the object moves obliquely during the projection of the five successive fringe patterns. Figure 3.4 shows the five fringe patterns captured from the object. The object is moved to the right direction for 7.7 mm in the second step, 4.3 mm in the left direction in the third step, 3.5 mm and 2.7 mm in the left and down direction in the fourth step and fifth step respectively. The reconstructed results for the second experiment are shown in Fig. 3.5. Figure 3.5(a) is the front view of the reconstructed result and Fig. 3.5(b) is the mesh display of the result, which are significantly distorted.

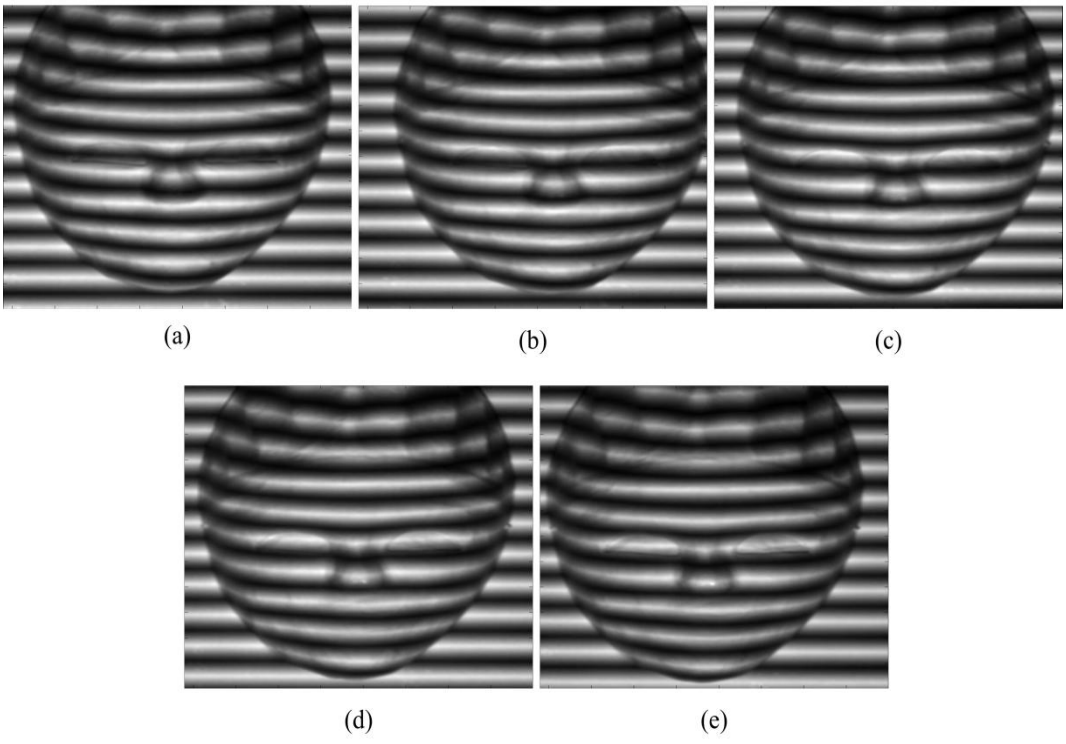

Fig. 3.4. The captured triangular fringe patterns when the object has oblique movement: (a)-(e) the fringe patterns of object from the first step to the fifth step.

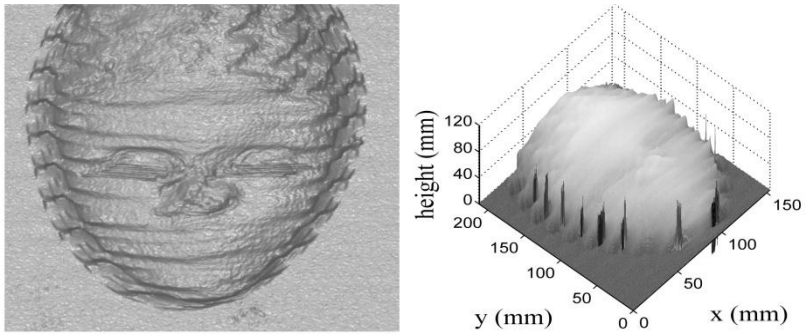

Fig. 3.5. The reconstructed result of the traditional triangular pattern phase-shifting profilometry when the object has oblique movement: (a) the front view of the reconstructed result; (b) the mesh display of the reconstructed result.

Then, in the third experiment, we applied the proposed method to the object moving in the same way as above. Figure 3.6 shows the normalised fringe patterns acquired from the object in motion.

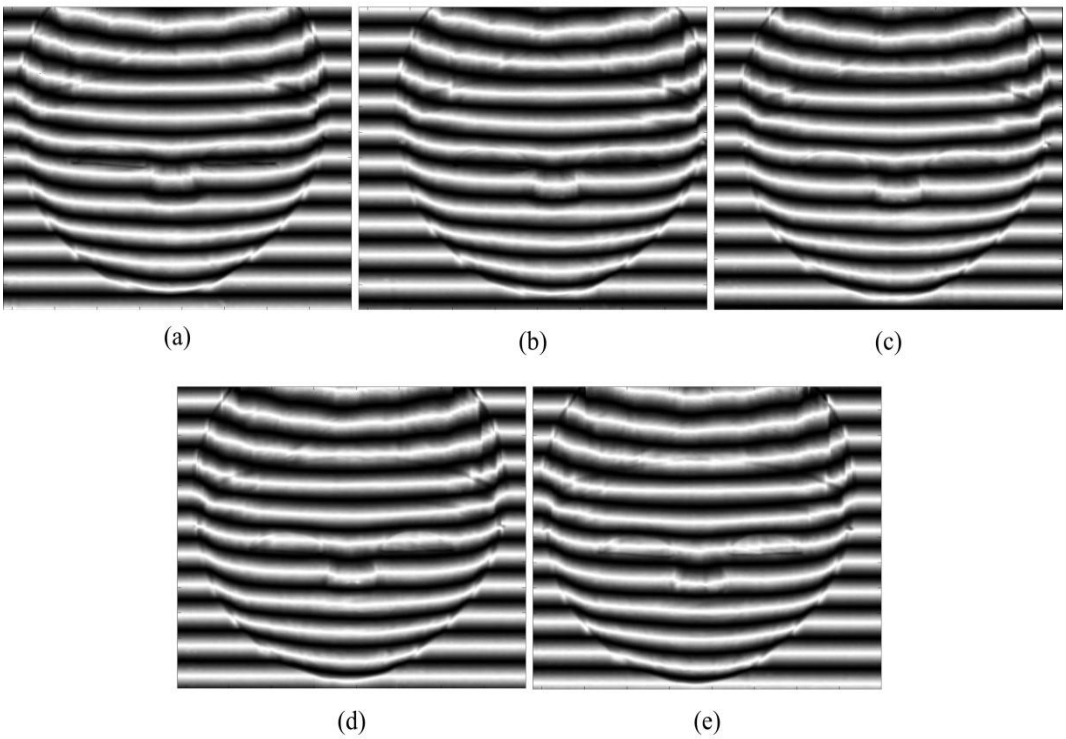

Fig. 3.6. The normalised fringe patterns of object with movement: (a)-(e) the normalized fringe patterns of the object with movement from the first step to the fifth step.

With the proposed method, we are able to obtain estimations of the normalised fringe patterns from the object without movement, as shown in Fig. 3.7. It is seen that, compared with the positions of the object in Fig. 3.6, the object is moved back by the proposed method.

Until now, the normalised fringe patterns of the object without movement are obtained, which then can be used in the traditional intensity ratio method with the results shown in Fig. 3.8. Figure 3.8(a) is the wrapped intensity ratio of the mask; Fig. 3.8(b) is the front view of the reconstructed result and Fig. 3.8(c) is the mesh display of the result. Within contrast to the results in Fig. 3.5, the surface of the mask is well reconstructed and hence significant improvement is achieved.

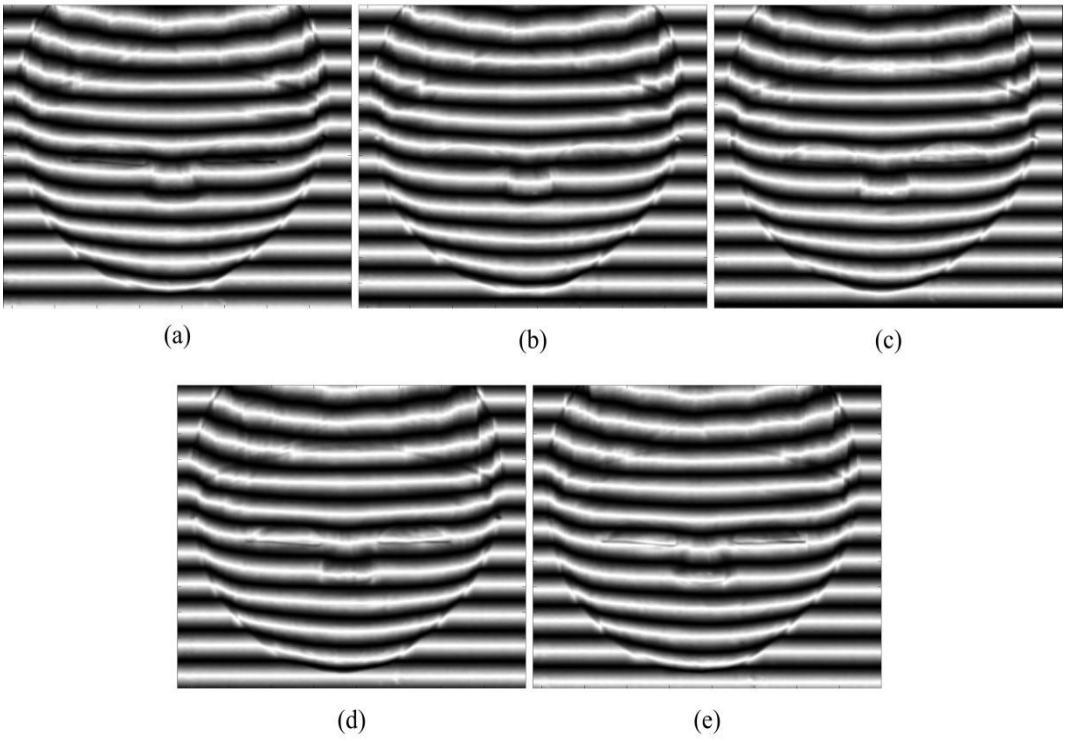

Fig. 3.7. The estimated normalised fringe patterns of the object without movement: (a)-(e) the normalised fringe patterns of object without movement from the first step to the fifth step.

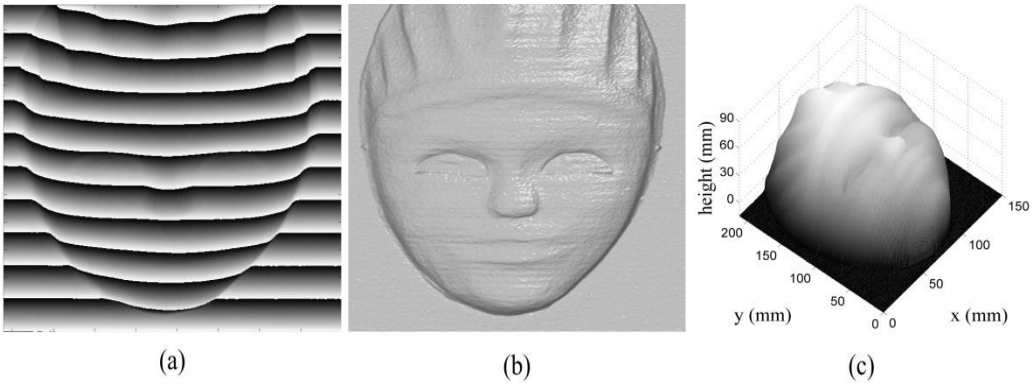

Fig. 3.8. The reconstructed results with the proposed algorithm when the object has oblique movement: (a) the wrapped intensity ratio of the object; (b) the front view of the reconstructed result; (c) the mesh display of the reconstructed mask.

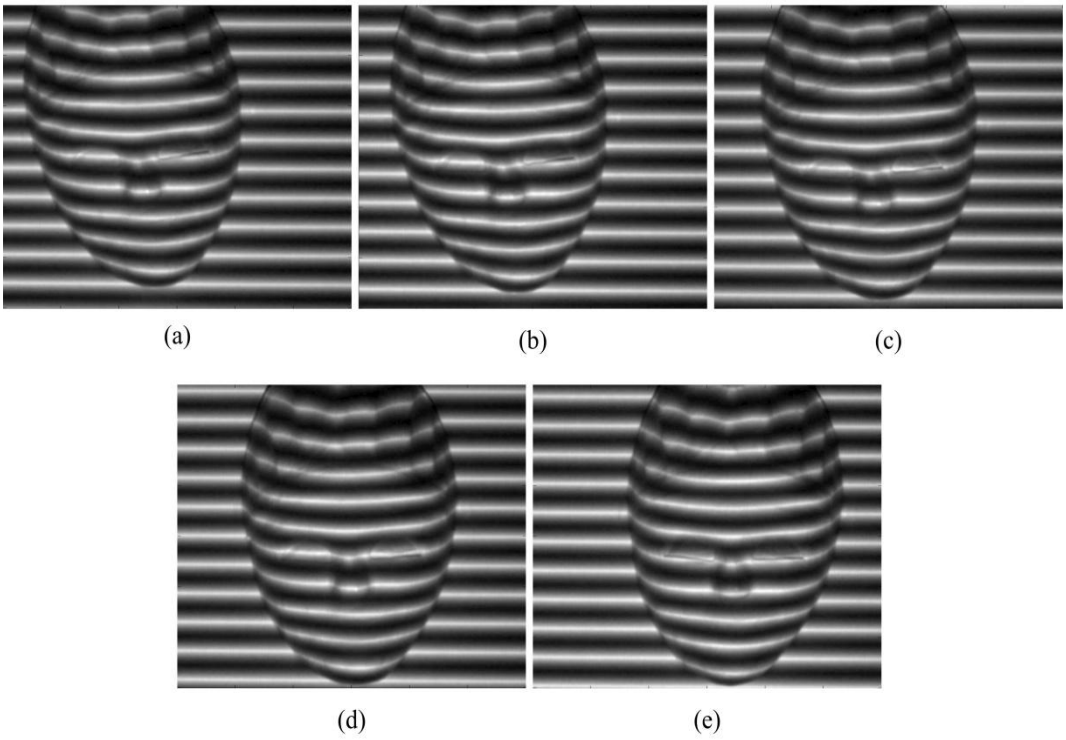

Fig. 3.9. The captured triangular fringe patterns when the object has rotation movement: (a)-(e) the fringe patterns of object from the first step to the fifth step.

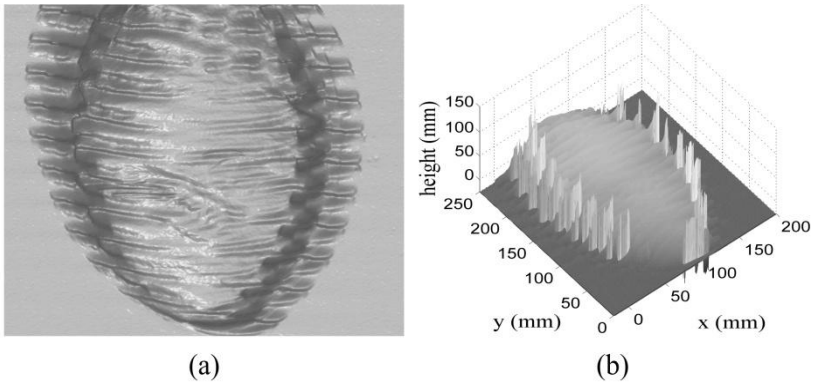

Fig. 3.10. The reconstructed result of the traditional triangular pattern phase-shifting profilometry when the object has rotation movement: (a) the front view of the reconstructed result; (b) the mesh display of the reconstructed result.

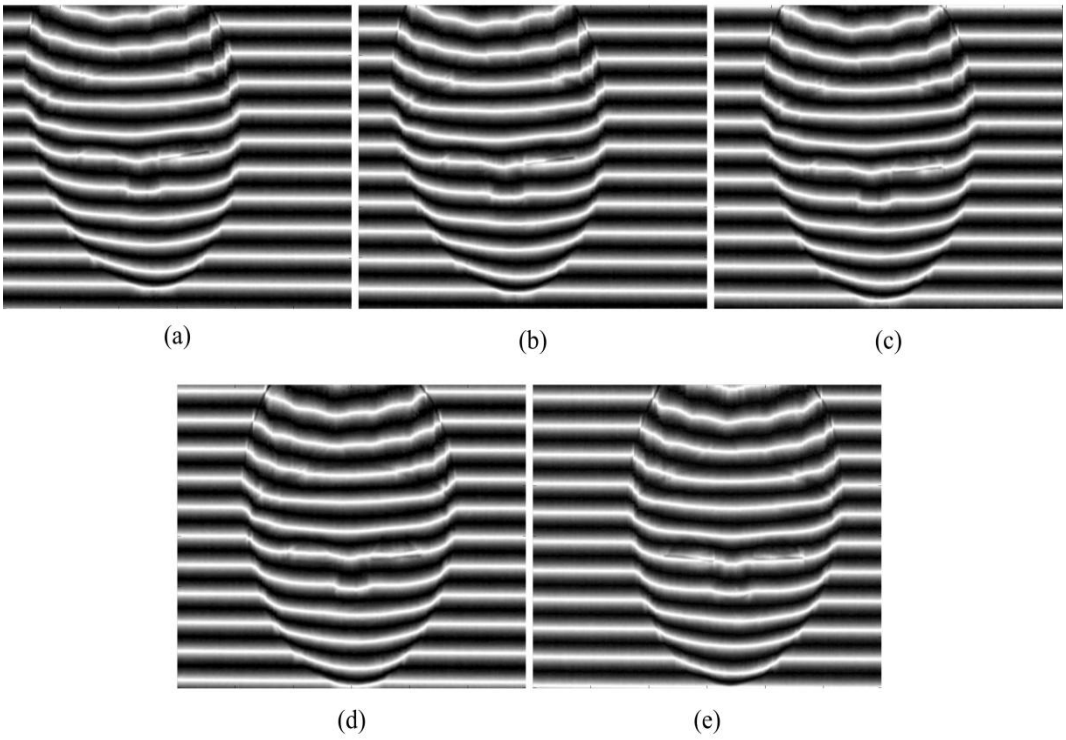

Fig. 3.11. The normalised fringe patterns of object with the rotation movement: (a)-(e) the normalised fringe patterns of the object with movement from the first step to the fifth step.

In the fourth experiment, we consider the case when the object is rotated clockwise around the bottom left corner during the measurement. The rotation angle is 0.1671 rad, 0.1446 rad, 0.1356 rad and 0.1103 rad for the second step, third step, fourth step

and fifth step respectively. Fig. 3.9 shows the captured fringe patterns of object from the first step to the fifth step.

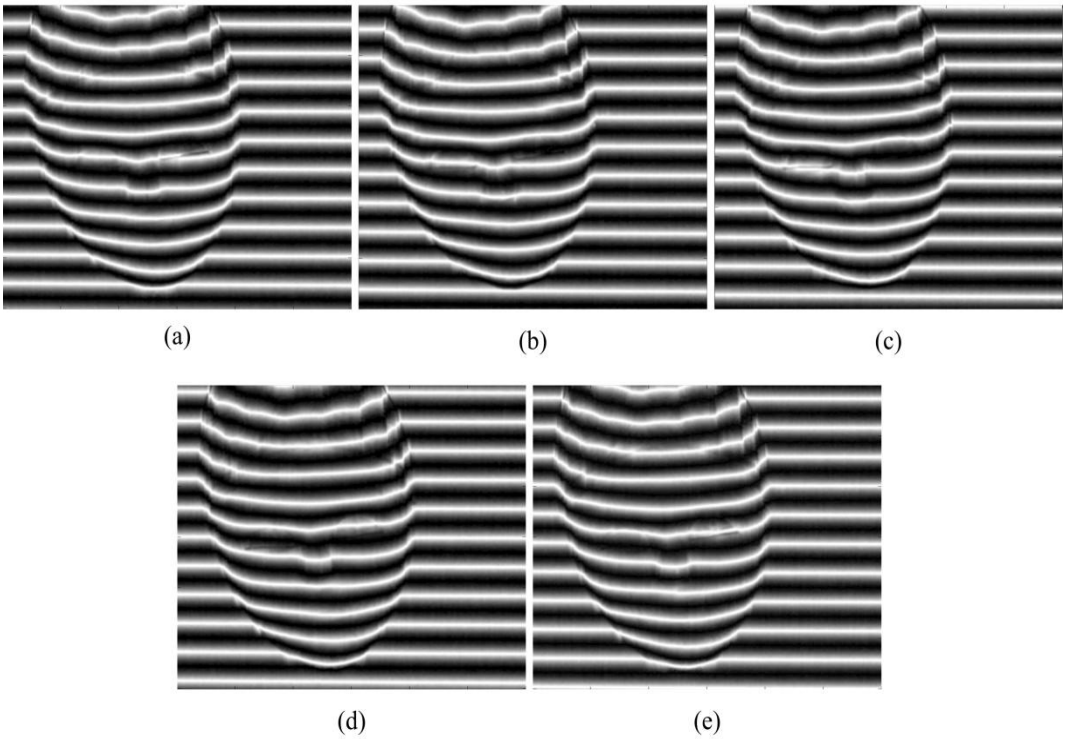

Fig. 3.12. The estimated normalised fringe patterns of the object without movement: (a)-(e) the normalised fringe patterns of object without movement from the first step to the fifth step.

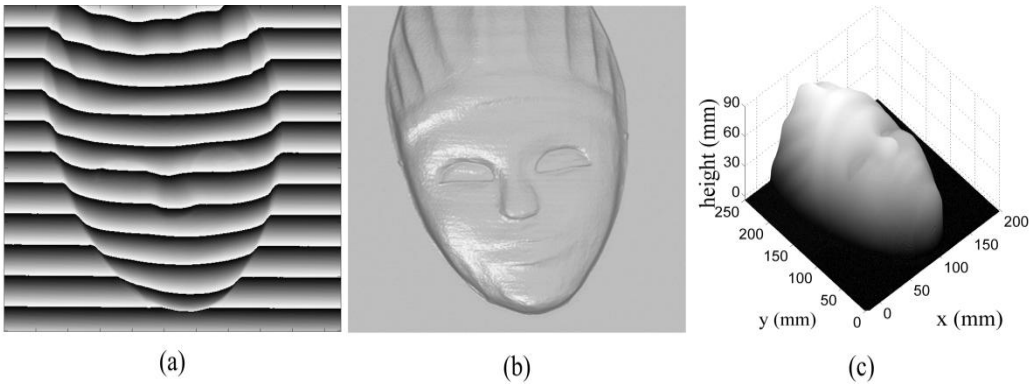

Fig. 3.13. The reconstructed results with the proposed algorithm when the object has rotation movement: (a) the wrapped intensity ratio of the object; (b) the front view of the reconstructed result; (c) the mesh display of the reconstructed mask.

Fig. 3.10 shows the reconstructed results obtained by the traditional intensity ratio method, which are obviously distorted in contrast to the original mask.

Then, the proposed approach is applied when the object is subject to the same rotation in the fifth experiment. Figure 3.11 shows the normalised fringe patterns of object with movement from the first step to the fifth step. With the proposed approach, the fringe patterns of object without movement can be estimated, as shown in Fig. 3.12. With the estimation of the normalised fringe patterns from the object without movement, the 3D shape of the object is reconstructed by the traditional intensity ratio technique. As shown in Fig. 3.13, the results are much better than those in Fig 3.10.

Table 3.1 shows the RMS error for the experimental results presented above, with the measurement result in Fig. 3.3 (the mask is kept stationary) as the reference and the help of the rotation matrix and translation vector. It is seen that, without the proposed method, the RMS error is 63.559 mm and 89.251 mm respectively. When the proposed approach is employed, the RMS error becomes 0.381 mm and 0.426 mm. Hence we can say that accuracy can be improved significantly by the proposed method.

Table 3.1. The RMS measurement error of the mask

Movement type	RMS error (the traditional triangular pattern profilometry)	RMS error (the proposed algorithm)
Oblique	63.559 mm	0.381 mm
Rotation	89.251 mm	0.426 mm

3.4 Conclusion

In this chapter, an approach has been proposed to improve the accuracy of 3D shape measurement of moving objects based on triangular patterns and the intensity ratio method. The proposed method consists of the following steps. Firstly, the fringe patterns of the moving object are captured. The rotation matrix and translation vector are then calculated to describe the movement of the object. Based on analysis of the influence of the movement on the fringe patterns, normalised fringe patterns of the object without movement can be estimated. These are used to compute the intensity ratio for the reconstruction of the 3D shape of the object. The performance of the proposed method has been confirmed by a series of experiments.

4 RECONSTRUCTION OF THE OBJECT WITH 3D MOVEMENT BASED ON PSP

4.1 Introduction

The proposed algorithms in Chapter 2 and Chapter 3 focus on errors caused by the 2D movement of the object. Because the 2D movement does not change the height of the object to be measured, the 3D shape of the object can be reconstructed using the derived expression of the fringe patterns with the information about the movement. In practice, movement of an object is not limited to two dimensions. With 3D movement, the height of the object will change and the variations are not known in advance. Therefore, the situation with 3D movement is more complex than with 2D movement.

This chapter presents a new approach that aims to reduce the errors associated with PSP for 3D shape measurement of a rigid object in 3D motion. In particular, we consider the case where the object has a rigid shape and the movement consists of a translation in the direction of height and 2D movement in the plane perpendicular to the direction of height. The camera is required to be parallel with the reference plane and the object movement is controlled by the optical instruments. Firstly, a new model is proposed to describe the fringe patterns reflected from an object that is subject to 3D movement. An iterative least-squares algorithm is then presented to estimate the phase map. Experiments show that, compared with conventional PSP, the proposed method is capable of significantly reducing the error caused by the 3D movement of the object. The details of the proposed algorithm are described below.

This chapter is organised as follows. Section 4.2 describes the method for addressing 3D movement when using PSP for shape measurement, Section 4.3 presents experimental results to verify the method and Section 4.4 concludes the chapter.

4.2 Principle of the proposed method for 3D movement based on PSP

Let us work out the relationship between the 3D movement of the object and the fringe patterns. As described in the Chapter 1, when the object is kept stationary and *N*-step PSP is used, the fringe patterns acquired from the reference plane and the object can be expressed by Eqs. (1.1) and (1.2). When the phase difference $\Phi(x, y)$ is obtained, the shape of the object can be calculated by Eq. (1.9).

Now let us consider the case where the object is subject to a 3D movement. Because of the movement, the height distribution changes from $h(x, y)$ to $\tilde{h}(x, y)$. Due to the rigid nature of the subject shape, a point (x, y) on the object is moved to (u, v) following the relationship below:

$$\begin{bmatrix} x \\ y \\ h(x,y) \end{bmatrix} = \mathbf{R}_{3D} \begin{bmatrix} u \\ v \\ \tilde{h}(u,v) \end{bmatrix} + \mathbf{T}_{3D}, \quad \begin{bmatrix} u \\ v \\ \tilde{h}(u,v) \end{bmatrix} = \bar{\mathbf{R}}_{3D} \begin{bmatrix} x \\ y \\ h(x,y) \end{bmatrix} + \bar{\mathbf{T}}_{3D}. \tag{4.1}$$

where $\mathbf{R}_{3D}$, $\bar{\mathbf{R}}_{3D}$, $\mathbf{T}_{3D}$ and $\bar{\mathbf{T}}_{3D}$ are referred to as rotation matrices and translation vectors for the 3D movement. As we only consider the case that the movement is the combination of a translation in the direction of height and a 2D movement in the plane perpendicular to the direction of height, we have:

$$\mathbf{R}_{3D}=\begin{bmatrix} r_{11} & r_{12} & 0 \\ r_{21} & r_{22} & 0 \\ 0 & 0 & 1 \end{bmatrix},\quad \mathbf{T}_{3D}=\begin{bmatrix} t_1 \\ t_2 \\ t_3 \end{bmatrix},\quad \bar{\mathbf{R}}_{3D}=\begin{bmatrix} \bar{r}_{11} & \bar{r}_{12} & 0 \\ \bar{r}_{21} & \bar{r}_{22} & 0 \\ 0 & 0 & 1 \end{bmatrix},\quad \bar{\mathbf{T}}_{3D}=\begin{bmatrix} \bar{t}_1 \\ \bar{t}_2 \\ \bar{t}_3 \end{bmatrix}. \tag{4.2}$$

Because the movement in the direction of height is exclusively a translation, we have:

$$\tilde{h}^{x-y}(u,v)=h^{x-y}(x,y)+\bar{t}_3=h^{x-y}[\,f_{3D}(u,v),g_{3D}(u,v)]+\bar{t}_3 \tag{4.3}$$

where $x-y$ denotes the coordinate system in which the functions are defined and

$$f_{3D}(u,v)=r_{11}u+r_{12}v+t_1,\quad g_{3D}(u,v)=r_{21}u+r_{22}v+t_2\,. \tag{4.4}$$

Without loss of generality, (u,v) can be replaced by (x,y). Therefore, Eq. (4.3) yields the following:

$$\tilde{h}^{x-y}(x,y)=h^{x-y}[\,f_{3D}(x,y),g_{3D}(x,y)]+\bar{t}_3 \tag{4.5}$$

Define the object fringe patterns after movement as:

$$\tilde{d}_n^{x-y}(x,y)=a+b\cos[\phi(x,y)+\tilde{\Phi}(x,y)+2\pi n/N] \tag{4.6}$$

where $\tilde{\Phi}(x,y)$ is the phase difference at point (x,y) after movement. Generally, the distance between the camera and the reference plane l_0 is much larger than the measured object and the height variation $\bar{t}_3$. The phase variations caused by $\bar{t}_3$ for each point of object are approximately same. Because of Eq. (4.5), we have

$$\tilde{\Phi}(x,y)=\Phi[\,f_{3D}(x,y),g_{3D}(x,y)]+\Phi' \tag{4.7}$$

where Φ' is the phase variation which is caused by $\bar{t}_3$. Submit Eq. (4.7) into Eq. (4.6), we have

$$\tilde{d}_n^{x-y}(x,y) = a + b\cos\{\phi(x,y) + \Phi[f_{3D}(x,y), g_{3D}(x,y)] + \Phi' + 2\pi n/N\} \quad (4.8)$$

Note that in order to avoid the phase ambiguity, Φ' is limited to less than 2π, requiring that the object movement is smaller than a single fringe. Now, let us consider Eq. (4.8) in a new coordinate system $\xi-\eta$ following the relationship below:

$$\begin{bmatrix} x \\ y \end{bmatrix} = \begin{bmatrix} \bar{r}_{11} & \bar{r}_{12} \\ \bar{r}_{21} & \bar{r}_{22} \end{bmatrix} \begin{bmatrix} \xi \\ \eta \end{bmatrix} + \begin{bmatrix} \bar{t}_1 \\ \bar{t}_2 \end{bmatrix} \quad (4.9)$$

In $\xi-\eta$ coordinate system, Eq. (4.8) becomes:

$$\begin{aligned} &\tilde{d}_n^{\xi-\eta}(\xi,\eta) = \tilde{d}_n^{x-y}[\bar{f}_{3D}(\xi,\eta), \bar{g}_{3D}(\xi,\eta)] \\ &= a + b\cos\{\phi[\bar{f}_{3D}(\xi,\eta), \bar{g}_{3D}(\xi,\eta)] + \Phi(\xi,\eta) + \Phi' + 2\pi n/N\} \end{aligned} \quad (4.10)$$

where

$$\bar{f}_{3D}(u,v) = \bar{r}_{11}u + \bar{r}_{12}v + \bar{t}_1, \quad \bar{g}_{3D}(u,v) = \bar{r}_{21}u + \bar{r}_{22}v + \bar{t}_2. \quad (4.11)$$

Use (x,y) to replace (ξ,η) and extend Eq. (4.10) to *N*-step PSP, yielding the following:

$$\begin{aligned} &\tilde{d}_n(x,y) = \tilde{d}_n^{x-y}[\bar{f}_{3D\_n}(x,y), \bar{g}_{3D\_n}(x,y)] \\ &= a + b\cos\{\phi[\bar{f}_{3D\_n}(x,y), \bar{g}_{3D\_n}(x,y)] + \Phi(x,y) + \Phi'_n + 2\pi n/N\} \end{aligned} \quad (4.12)$$

Equation (4.12) describes the influence of the 3D movement on the fringe patterns. To simplify the expression, Eq. (4.12) can be rewritten as following:

$$\tilde{d}_n(x,y) = a + b\cos[\phi'_n(x,y) + \Phi(x,y) + \delta_n] \tag{4.13}$$

where $\phi'_n(x,y) = \phi[\bar{f}_{3D\_n}(x,y), \bar{g}_{3D\_n}(x,y)]$ and it can be obtained by the fringe patterns of reference plane and Eq. (4.11); $\delta_n = \Phi'_n + 2\pi n/N$ is the phase sift amount caused by the phase shift of PSP and height variations $\bar{t}_3$ for each step, which is unknown in advance. In order to obtain $\Phi(x,y)$, we must estimate the value of δ_n. Inspired by the methods presented in Ref. [129-131] which can extract the random phase shifts for other applications, we propose to employ iterative least-squares approach to obtain δ_n and $\Phi(x,y)$. The proposed method starts from an initial value of $\delta_n = 2\pi n/N$ and can be implemented by the following steps.

Step 1: Estimate $\Phi(x,y)$ when an estimation of δ_n is available (it takes the initial value for the first iteration). To this end we rewrite Eq. (4.13) as:

$$\tilde{d}_n(x,y) = a + B(x,y)\cos[\phi'_n(x,y) + \delta_n] + C(x,y)\sin[\phi'_n(x,y) + \delta_n] \tag{4.14}$$

where $B(x,y) = b\cos\Phi(x,y)$ and $C(x,y) = -b\sin\Phi(x,y)$. Assuming that there are M pixels in one fringe pattern, and when δ_n is known, there are 2M+1 unknowns and MN equations in Eq. (4.14). When $N \geq 3$, the unknowns can be obtained by the over-determined least-squares method. Apply Eq. (4.12) on the measured fringe patterns $\tilde{d}_n^{x-y}$ to obtain $d_n^m(x,y)$, then, the sum of the squared error in each pixel is:

$$S(x,y) = \sum_{n=1}^{N}[\tilde{d}_n(x,y) - d_n^m(x,y)]^2 \tag{4.15}$$

Based on Eq. (4.15), the least-squares criteria satisfy that $\partial S(x,y)/\partial a = 0$, $\partial S(x,y)/\partial B(x,y) = 0$ and $\partial S(x,y)/\partial C(x,y) = 0$, yield the following:

$$\mathbf{X}(x,y) = \mathbf{A}^{-1}(x,y)\mathbf{B}(x,y) \tag{4.16}$$

where

$$\mathbf{A}(x,y) = \begin{bmatrix} N & \sum_{n=1}^{N}\cos[\phi_n'(x,y)+\delta_n] & \sum_{n=1}^{N}\sin[\phi_n'(x,y)+\delta_n] \\ \sum_{n=1}^{N}\cos[\phi_n'(x,y)+\delta_n] & \sum_{n=1}^{N}\cos^2[\phi_n'(x,y)+\delta_n] & \sum_{n=1}^{N}\cos[\phi_n'(x,y)+\delta_n]\times \\ & & \sum_{n=1}^{N}\sin[\phi_n'(x,y)+\delta_n] \\ \sum_{n=1}^{N}\sin[\phi_n'(x,y)+\delta_n] & \sum_{n=1}^{N}\cos[\phi_n'(x,y)+\delta_n]\times & \sum_{n=1}^{N}\sin^2[\phi_n'(x,y)+\delta_n] \\ & \sum_{n=1}^{N}\sin[\phi_n'(x,y)+\delta_n] & \end{bmatrix}, \tag{4.17}$$

$$\mathbf{X}(x,y) = [a \quad B(x,y) \quad C(x,y)]^T, \tag{4.18}$$

$$\mathbf{B}(x,y) = [\sum_{n=1}^{N} d_n^m(x,y) \quad \sum_{n=1}^{N} d_n^m(x,y)\times\cos[\phi_n'(x,y)+\delta_n] \quad \sum_{n=1}^{N} d_n^m(x,y)\times\sin[\phi_n'(x,y)+\delta_n]]^T. \tag{4.19}$$

From Eqs. (4.16)-(4.19) the unknowns a, $B(x,y)$ and $C(x,y)$ can be solved and $\Phi(x,y)$ can be determined:

$$\Phi(x,y) = \tan^{-1}[-C(x,y)/B(x,y)] \tag{4.20}$$

Step 2: Estimate δ_n by the least-squares method using $\Phi(x,y)$ estimated by Step 1. For this purpose Eq. (4.13) can also be rewritten as:

$$\tilde{d}_n(x,y) = a + B_n'\cos[\phi_n'(x,y)+\Phi(x,y)] + C_n'\sin[\phi_n'(x,y)+\Phi(x,y)] \tag{4.21}$$

where $B_n' = b\cos\delta_n$ and $C_n' = -b\sin\delta_n$. The sum of the squares error in each frame is:

$$S_n' = \sum_{(x,y)}[\tilde{d}_n(x,y) - d_n^m(x,y)]^2 \tag{4.22}$$

The least-squares solution which minimises S_n' is:

$$\mathbf{X}_n' = \mathbf{A}_n'^{-1}\mathbf{B}_n' \tag{4.23}$$

where

$$\mathbf{A}_n' = \begin{bmatrix} M & \sum_{x,y}\cos[\phi_n'(x,y)+\Phi(x,y)] & \sum_{x,y}\sin[\phi_n'(x,y)+\Phi(x,y)] \\ \sum_{x,y}\cos[\phi_n'(x,y)+\Phi(x,y)] & \sum_{x,y}\cos^2[\phi_n'(x,y)+\Phi(x,y)] & \sum_{x,y}\cos[\phi_n'(x,y)+\Phi(x,y)]\times \sin[\phi_n'(x,y)+\Phi(x,y)] \\ \sum_{x,y}\sin[\phi_n'(x,y)+\Phi(x,y)] & \sum_{x,y}\cos[\phi_n'(x,y)+\Phi(x,y)]\times \sin[\phi_n'(x,y)+\Phi(x,y)] & \sum_{x,y}\sin^2[\phi_n'(x,y)+\Phi(x,y)] \end{bmatrix}, \tag{4.24}$$

$$\mathbf{X}_n' = [a \quad B_n' \quad C_n']^T, \tag{4.25}$$

$$\mathbf{B}_n' = [\sum_{x,y} d_n^m(x,y) \quad \sum_{x,y} d_n^m(x,y)\times \cos[\phi_n'(x,y)+\Phi(x,y)] \quad \sum_{x,y} d_n^m(x,y)\times \sin[\phi_n'(x,y)+\Phi(x,y)]]^T. \tag{4.26}$$

Hence the unknowns a, B_n' and C_n' can be obtained by Eqs. (4.23)-(4.26). Then, δ_n can be calculated by:

$$\delta_n = \tan^{-1}[-C_n' / B_n'] \tag{4.27}$$

The two steps described above are repeated in the way that δ_n estimated from Step 2 is employed in Step 1 to obtain a better estimation of $\Phi(x,y)$, and $\Phi(x,y)$ obtained in Step 1 is utilised in Step 2 to yield a better estimation of δ_n. The iterative process will stop when the convergence condition is met:

$$\left|(\delta_n^k - \delta_1^k) - (\delta_n^{k-1} - \delta_1^{k-1})\right| < \varepsilon \tag{4.28}$$

Then $\Phi(x, y)$ will be taken as the correct phase distribution. In the above k is the number of iterations and ε is the accuracy requirement, e.g., 10^{-4}. In the experiments presented below, we found that a very good convergence can always be achieved, e.g., k is around 10 when $\varepsilon = 10^{-4}$.

4.3 Experiments

Experiments have been carried out to verify the proposed method, where the object is the mask shown in Fig. 4.1(a) and the PSP is of 3-step. The object was moved on step-by-step basis in order to emulate the instantaneous positions of the object when the multiple image patterns are taken. Note that in practice, the shutter of the camera must be fast enough in order to avoid blurring in the captured images. As the camera in our laboratory is not fast enough, we kept the object stationary at each step when the fringe patterns are taken.

In order to obtain $\Phi(x, y)$ from Eq. (4.13), $\phi_n'(x, y)$ should be available. To this end we should obtain $(\bar{r}_{11}, \bar{r}_{12}, \bar{r}_{21}, \bar{r}_{22}, \bar{t}_1, \bar{t}_2)$ in Eq. (4.11). Three marks are employed and placed on the object as shown in Fig. 4.1(a). The centers of the marks are extracted using the same approach described in Chapter 2, which are used as the corresponding points between multiple fringe patterns. As Eqs. (4.1) and (4.2) show that $\bar{t}_3$ is independent of $(\bar{r}_{11}, \bar{r}_{12}, \bar{r}_{21}, \bar{r}_{22}, \bar{t}_1, \bar{t}_2)$, the SVD method described in Chapter 2 can be employed to obtain $(\bar{r}_{11}, \bar{r}_{12}, \bar{r}_{21}, \bar{r}_{22}, \bar{t}_1, \bar{t}_2)$. Then, the following experiments have been conducted:

Experiment 1: We applied the traditional 3-step PSP to the mask when the mask is kept stationary during the measurement. The measurement result is shown in Fig. 4.1(b), which matches expectations of the traditional 3-step PSP.

Fig. 4.1. The measurement results for the first experiment: (a) the measured mask; (b) the reconstructed result by mesh display with the traditional PSP when the object is stable.

Experiment 2: Then, we moved the object in the direction of height for 3 mm and 4 mm in the second and third step of PSP respectively. The result with traditional PSP is shown in Fig. 4.2(a) and there are obvious errors. In contrast, when the proposed algorithm is applied to the case where the object is moved by the same amount as above, significant improvement can be obtained as shown in Fig. 4.2(b).

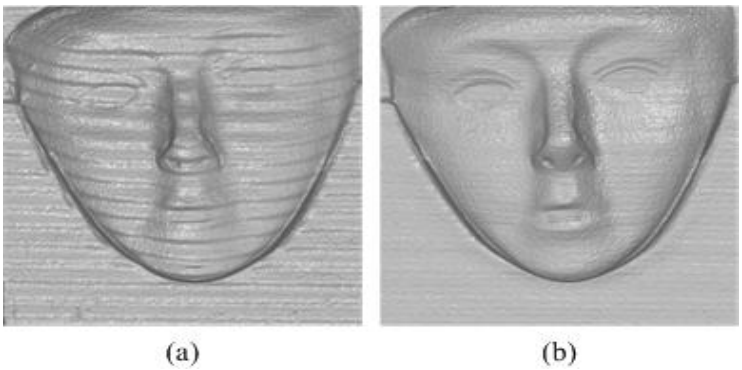

Fig. 4.2. Comparison of measurement results for the second experiment: (a) the reconstructed result by mesh display with the traditional PSP; (b) the reconstructed result by mesh display with the proposed method.

Experiment 3: In the third experiment, the object is rotated clockwise in $x-y$ plane for 0.0599 rad and moved in the direction of height for 5 mm in the second step of PSP; then, the object is rotated clockwise in $x-y$ plane for 0.0256 rad, and moved in the direction of height for 3 mm in the third step of PSP. The result with the traditional PSP is shown in Fig. 4.3(a) showing significant errors. With the proposed algorithm, the result is depicted in Fig. 4.3(b), also showing significant improvement.

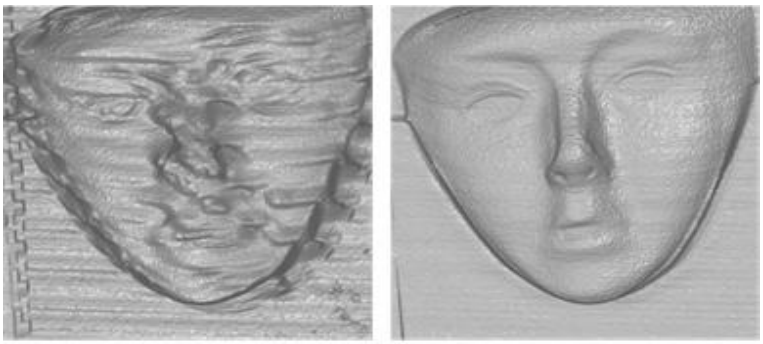

Fig. 4.3. Comparison of measurement results for the third experiment: (a) the reconstructed result by mesh display with the traditional PSP; (b) the reconstructed result by mesh display with the proposed method.

Experiment 4: For the fourth experiment, the object is moved 3 mm in x-direction, 5 mm in y-direction, 3 mm in the direction of height and rotated clockwise in $x-y$ plane for 0.0295 rad in the second step of PSP; and then in the third step of PSP, the object is moved 2 mm in the x-direction, 4 mm in y-direction, 2 mm in the direction of height and rotated clockwise for 0.0277 rad in $x-y$ plane. Figure 4.4(a) shows the result with traditional PSP. Significant errors occur in the result. The result with the proposed algorithm is shown in Fig. 4.4(b), again demonstrating significant improvement.

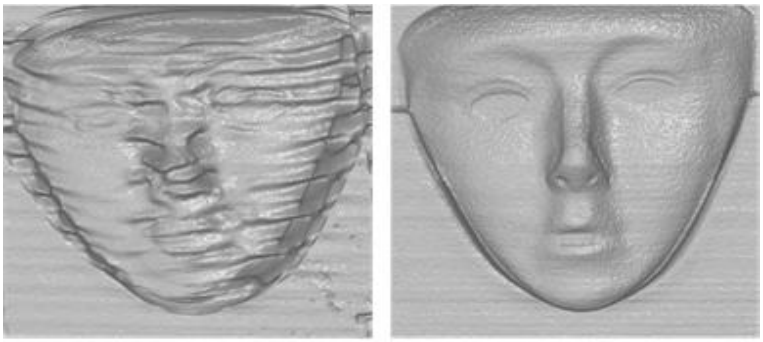

Fig. 4.4. Comparison of measurement results for the fourth experiment: (a) the reconstructed result by mesh display with the traditional PSP; (b) the reconstructed result by mesh display with the proposed method.

In order to evaluate the performance of the proposed algorithm, we also computed the RMS errors of the height for all the points on the object surface, the iterative times and the height offset (mean of the error) of the proposed method for the above experiments. The results are shown in Table 4.1. As the exact shape of the mask is not available, the reconstructed result for the stationary object in Fig. 4.1(b) is used as the reference for our computation. Table 4.1 shows that the proposed method has significant accuracy improvement and fast convergence.

Table 4.1. Accuracy and iterative times ($\varepsilon = 10^{-4}$)

Experiment number	RMS errors (traditional PSP)	RMS errors (proposed method)	Iterative times	Height offset
Experiment 2	10.385 mm	0.071 mm	9	0.002 mm
Experiment 3	62. 946 mm	0.089 mm	12	0.006mm
Experiment 4	57.174 mm	0.083 mm	14	0.004mm

We also compared the accuracy of the results shown in Fig. 4.4(a) and Fig. 4.4(b). The absolute errors associated with these two cases are shown in Fig. 4.5. It can be

seen that the absolute error in Fig. 4.5(b) using the proposed method is significant smaller than the error of the traditional PSP in Fig. 4.5(a).

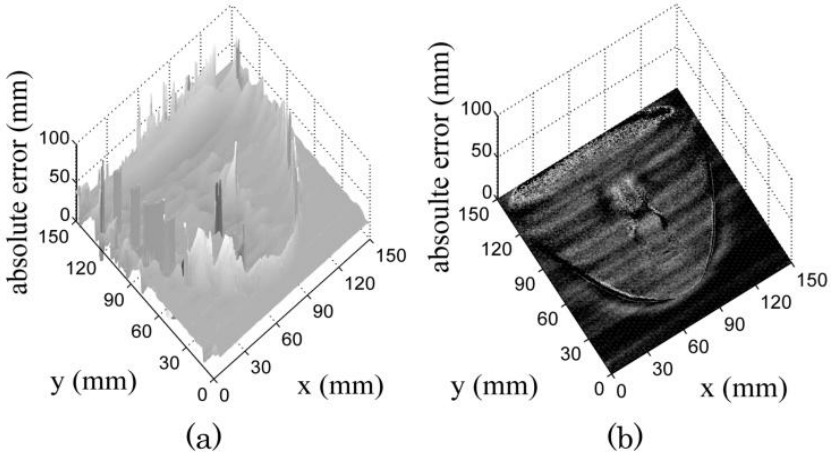

Fig. 4.5. (a)-(b) The absolute error for Fig. 4.4(a) and Fig. 4.4(b).

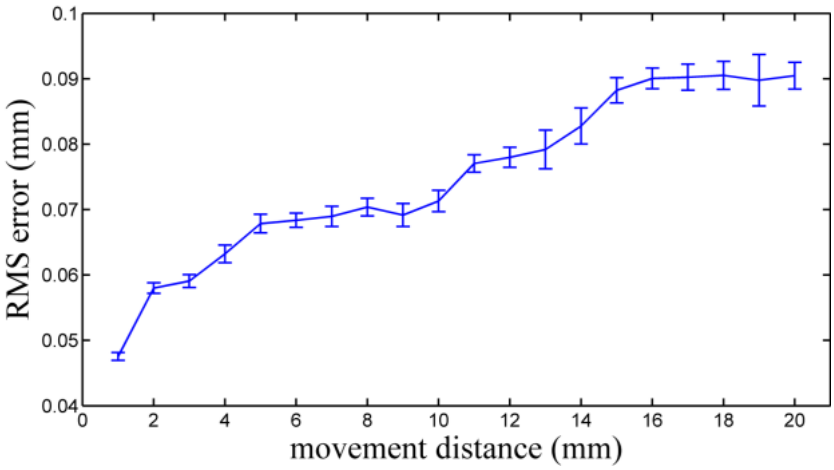

Fig. 4.6. The relationship between the accuracy of the proposed method and the movement distance in the direction of height.

We also studied how the amount of movement impacts on the RMS error and the result is shown in Fig. 4.6. In the second step and third step of PSP, the object is moved equally and the movement distance shown in Fig. 4.6 is the sum of the movement. For each movement distance in Fig. 4.6, 8 experiments are carried out. Fig. 4.6 shows the mean of the RMS errors and the error bars giving the standard

deviation for the 8 experiments at each movement distance. It is seen that RMS error slightly increases with the movement distance. This may be due to the influence of geometric structure of the system, as we only used the ideal model for the system structure, the camera and the projector. It is expected that the error can be reduced by means of accurate calibration of the system [122, 123].

The computation cost associated with the proposed method was also analysed. Among other operations, the wrapped phase extraction in Eqs. (4.16)-(4.20) is most time consuming due to a matrix inversion for each pixel of the fringe patterns. However, parallel computing can be used as the computation can be independently implemented for each individual point. We employed such an approach using Matlab on a Dell Vostro 470 computer with 3.4 GHz CPU and 8G memory, and it took 0.41 second to complete one iteration of Step 1 and Step 2 of the proposed algorithm for the fringe pattern of 500 by 500 pixels. It is expected that the time can be further reduced if dedicated hardware such as digital signal processors is employed [132].

4.4 Conclusion

A new approach has been proposed to determine the phase map of phase-shifted fringe patterns reflected from a rigid object that is subjected to 3D movement. Firstly, a new model has been presented to describe the fringe patterns influenced by the 3D movement. An iterative least-squares method has then been proposed to estimate the correct phase map without requiring knowledge of the height variations. The estimated phase map can be used to reconstruct the 3D shape with improved accuracy performance compared with the conventional PSP approach. Experimental results have been presented to verify the effectiveness of the proposed method.

5 AUTOMATIC REMOVAL OF THE INVALID POINTS CAUSED BY THE SHADOW IN PSP

5.1 Introduction

PSP has been widely used in many applications as a non-destructive, high accuracy and high speed technique for 3D shape reconstruction [100, 133, 134]. However, because the camera and the projector probe the object from different directions, an area of shadow will be introduced into the captured fringe patterns of the object. The shadow area does not contain information of the projected fringe patterns, resulting in errors of the reconstructed result for the points in the shadow.

This chapter proposes a new method to remove the invalid points caused by the shadow in PSP. The idea is as follows. Firstly, the 3D reconstruction is carried out using the PSP method presented by Zhang and Huang [122], where the reconstructed 3D shape is based on the relationships between a point on the object surface and the corresponding points on the image captured by the camera and on the fringe projected by the projector. Due to the existence of shadows, the obtained 3D data contains errors. Then, using the above relationships, the entire 3D data is mapped into the DMD plane of the projector on a point-by-point basis. The shadow points are detected from the mapped positions on the DMD plane. The proposed method can achieve automatic 3D measurement by removing the errors caused by shadow. In addition, the performance of the 3D registration can be improved significantly. This chapter is organised as follows. Section 5.2 discusses the principle of the proposed method for removing the errors caused by the shadow. In section 5.3,

experimental results are presented to verify the proposed method, and Section 5.4 concludes this chapter.

5.2 The proposed method to remove the errors caused by shadow

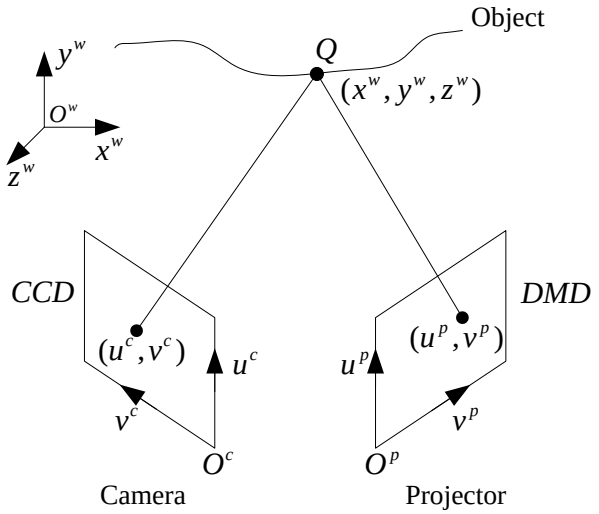

Fig. 5.1 The schematic diagram of the measurement system.

Figure 5.1 shows the schematic diagram of the measurement system presented in [122], which involves three coordinate systems, including projector coordinate system $(O^p; u^p, v^p)$, camera coordinate system $(O^c; u^c, v^c)$ and the word coordinate system $(O^w; x^w, y^w, z^w)$. A point (x^w, y^w, z^w) on the object surface corresponds to the positions at the other two coordinates by the following relationship [122]:

$$\begin{cases} s_c[u^c, v^c, 1]^T = \mathbf{A}^c \mathbf{R}^c \mathbf{T}^c [x^w, y^w, z^w, 1]^T \\ s_p[u^p, v^p, 1]^T = \mathbf{A}^p \mathbf{R}^p \mathbf{T}^p [x^w, y^w, z^w, 1]^T \end{cases} \tag{5.1}$$

where $\mathbf{A}^c$ and $\mathbf{A}^p$ are the intrinsic parameter matrices for the camera and projector respectively; $(\mathbf{R}^c, \mathbf{T}^c)$ and $(\mathbf{R}^p, \mathbf{T}^p)$ are the extrinsic parameter matrices for the camera and projector respectively. s_c and s_p are the scale factors, which are

functions of (x^w, y^w, z^w). The intrinsic and extrinsic parameters can be obtained through the calibration of the system. In Eq. (5.1), there are 4 equations and 5 unknown parameters $(x^w, y^w, z^w, u^p, v^p)$. Therefore, in order to obtain the height distribution of the object (x^w, y^w, z^w), additional constraint can be introduced by the corresponding relationship between the (u^c, v^c) and (u^p, v^p), based on the phase relationship obtained by PSP.

For the N-step PSP, images with phase shifted fringes vertical to the direction u^p are projected by the projector and can be expressed as

$$d_n^p(u^p, v^p) = a^p + b^p \cos(\Phi^p(u^p, v^p) + \frac{2\pi(n-1)}{N}) \tag{5.2}$$

where $n = 1, 2, 3, ..., N$; $\Phi^p(u^p, v^p) = 2\pi f^p u^p$ and f^p is the frequency of the fringe pattern designed in the projector; a^p and b^p can be set in the computer to adjust the intensity of the fringe patterns. Then, the fringe patterns are captured by the camera and can be expressed as:

$$d_n^c(u^c, v^c) = A(u^c, v^c) + B(u^c, v^c) \cos(\phi^c(u^c, v^c) + \frac{2\pi(n-1)}{N}) \tag{5.3}$$

where

$$A(u^c, v^c) = C[r(u^c, v^c)a^p + d^a(u^c, v^c)], \tag{5.4}$$

and

$$B(u^c, v^c) = Cr(u^c, v^c)b^p \tag{5.5}$$

$A(u^c, v^c)$ is the average intensity, $B(u^c, v^c)$ is the intensity modulation of the sinusoidal fringe patterns; C denotes the sensitivity to the light of the camera; $r(u^c, v^c)$ is the reflectivity of the object surface; $d^a(u^c, v^c)$ is the ambient light. When $N \geq 3$, $A(u^c, v^c)$, $B(u^c, v^c)$ and $\phi^c(u^c, v^c)$ can be obtained by the following,

$$A(u^c, v^c) = \frac{1}{N}\sum_{n=1}^{N} d_n^c(u^c, v^c), \tag{5.6}$$

$$B(u^c, v^c) = \frac{2}{N}\sqrt{[\sum_{n=1}^{N} d_n^c(u^c, v^c)\sin(\frac{2\pi n}{N})]^2 + [\sum_{n=1}^{N} d_n^c(u^c, v^c)\cos(\frac{2\pi n}{N})]^2}, \tag{5.7}$$

$$\phi^c(u^c, v^c) = \arctan\frac{-\sum_{n=1}^{N} d_n^c(u^c, v^c)\sin 2\pi n / N}{\sum_{n=1}^{N} d_n^c(u^c, v^c)\cos 2\pi n / N}. \tag{5.8}$$

Define

$$\gamma(u^c, v^c) = \frac{B(u^c, v^c)}{A(u^c, v^c)} \tag{5.9}$$

where $0 < \gamma(u^c, v^c) < 1$ is the data modulation and it can be used to describe the quality of the fringe pattern in terms of signal to noise ratio [135]. The higher of the $\gamma(u^c, v^c)$, the better of the quality.

With the fringe patterns captured by the camera, the wrapped phase map $\phi^c(u^c, v^c)$ can be obtained by Eq. (5.8), which is then unwrapped to yield the absolute phase map $\Phi^c(u^c, v^c)$. Note that in the phase map $\Phi^p(u^p, v^p)$, the absolute phase values are constant with respect to v^p for the same u^p. Therefore, for a specific point

(u^c, v^c) , a line along u^p on the DMD can be found based on $\Phi^p(u^p, v^p) = \Phi^c(u^c, v^c)$.

From Eq. (5.1), three linear equations can be obtained as the following,

$$\begin{cases} f_1(x^w, y^w, z^w, u^c) = 0 \\ f_2(x^w, y^w, z^w, v^c) = 0 \\ f_3(x^w, y^w, z^w, u^p) = 0 \end{cases} \tag{5.10}$$

where (u^c, v^c, u^p) are known. Therefore, (x^w, y^w, z^w) can be determined by solving Eq. (5.10).

The object is reconstructed by Eq. (5.10). However, in practice, there are shadows exist in the captured images. The shadows do not contain the information of the projected fringe patterns. When Eq. (5.8) is applied to the points in the shadow area, errors will be introduced in the phase value. The incorrect phase value will be corresponded to an invalid u^p in the DMD plane, leading to the errors in the reconstruction of the object.

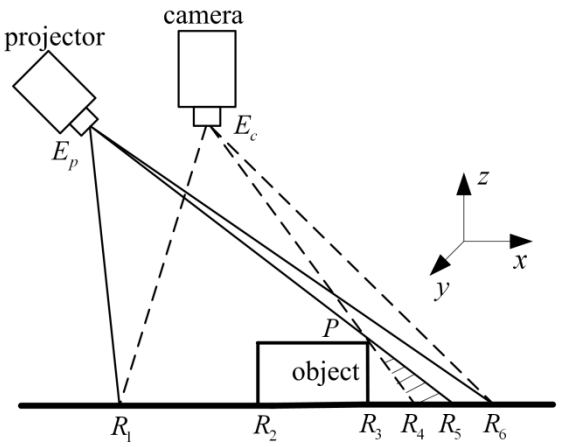

Fig. 5.2. The principle of the reason causing shadow in PSP system.

In order to remove the points in the shadow area, the reason causing the shadow in the PSP system should be analyzed. In the schematic diagram of the PSP system shown in Fig. 5.2, the scope of the camera and the projector is $E_c R_1 R_6$ and $E_p R_1 R_6$ respectively. The light beam $E_p P R_5$ emitted from the projector is projected onto the point R_5 through point P on the object. Due to the sharp change in the height of the object at point P, a shadow area PR_3R_5 will be formed. The camera captures the fringe patterns in another direction and it can observe point R_4 through point P. It is apparent that the shadow area PR_4R_5 will be captured by the camera, which does not contain the information of the projected fringe patterns.

We propose to identify the points in shadow by verifying whether they are projected from the DMD plane or not. In order to do this, the whole image captured by the camera can be divided into two types of area, namely the fringe pattern area and shadow area. Assuming the camera can see all the areas on the object surface illuminated by the projector (as shown in Fig. 5.2), the fringe pattern area on the camera image will cover the whole fringe pattern projected. While correct 3D reconstruction can be obtained from the fringe pattern area, measurement error occurs due to the shadow areas. If we map all the points of the reconstructed result (include the fringe pattern area and shadow area) to the DMD plane using Eq. (5.1), the points from the fringe pattern area will cover all the points on the DMD plane. In contrast, the mapped points from the shadow area may be outside or inside the boundary of the DMD. We will make use of the positions associated with the mapped points to detect the shadow areas. The details of the proposed approach are described below.

If a point is mapped outside the DMD boundary (Type1), it will be detected as the shadow point. This is because the entire fringe pattern is reflected by the surface, and hence if a 3D point is valid, its corresponding mapped point on DMD must be within the dimension of the fringe pattern, i.e., the boundary of the DMD.

If a mapped point has unique positions within the boundary of DMD (Type 2), the point will be detected as a valid point. This is also because the entire fringe pattern is reflected by the surface, implying that any point on the pattern is utilised for 3D reconstruction, which must correspond to a valid 3D point. Hence, if the mapped point is unique on the DMD, the 3D point must be valid.

3D points with error may also be mapped to points within the boundary, but in this case these points must coincide with others, because the valid 3D data must cover the entire DMD. Therefore for the mapped points with the boundary of DMD but do not have unique positions (Type 3), one must be valid and the remaining are the shadow ones. In this case decision needs to be made to indentify the valid one.

For these Type 3 points, we propose to use the data modulation $\gamma(u^c, v^c)$ to identify them [110, 136]. The shadow areas usually only contain the ambient light $d^a(u^c, v^c)$ and hence from Eq. (5.6) and Eq. (5.7) we have

$$A(u^c, v^c) = d^a(u^c, v^c), \tag{5.11}$$

and

$$B(u^c, v^c) = 0 \tag{5.12}$$

From the expression of the data modulation $\gamma(u^c, v^c)$ described in Eq. (5.9), we can see that $\gamma(u^c, v^c) = 0$ or should be very small if not zero for the points in shadow.

In contrast, for the valid points reflecting the fringe patterns, submit Eq. (5.4) and Eq. (5.5) into Eq. (5.9), we have

$$\gamma(u^c, v^c) = \frac{r(u^c, v^c) b^p}{r(u^c, v^c) a^p + d^a(u^c, v^c)} \tag{5.13}$$

In practice, $a^p = b^p$ is usually used in projector in order to make full use of the intensity range, and the ambient light $d^a(u^c, v^c)$ is much smaller than the a^p and b^p. Therefore, when the reflectivity $r(u^c, v^c)$ is not too small, the $\gamma(u^c, v^c)$ should exhibit larger values in the fringe pattern areas than the ones in the shadow areas.

Consequently, when multiple points are overlapping in the DMD plane, the one with the biggest $\gamma(u^c, v^c)$ can be identified as the valid point and the rest as the invalid points from the shadow. Different with other methods employing the data modulation to remove the shadow, threshold is not required in the proposed method, resulting more flexible and robust algorithm.

5.3 Experiments

In order to verify the proposed algorithm, a plaster pyramid model shown in Fig. 5.3(a) is reconstructed in the experiments. Three-step PSP is utilised to reconstruct the object and Fig. 5.3(b) is one of the captured fringe patterns. It is apparent that the shadow area exists in the captured fringe pattern of the object. In the experiments, the absolute phase map is obtained with the help of six Gray-code patterns. The decoded Gray-code value is used as the index of the period of the fringe patterns.

Due to the existence of the shadow, the decoded Gray-code is also not correct in the shadow area, leading to the loss of monotonicity associated with the absolute phase map.

In the first experiment, the object is reconstructed by the three-step PSP directly. The reconstructed result is shown in Fig. 5.4. It is apparent that, the result of the points on the object matches the expectations of the PSP, but the points in the shadow area are reconstructed with errors.

In the second experiment, the proposed method is applied on the same fringe patterns used in the above experiment. The result is shown in Fig. 5.5. The erroneous points in the shadow area are completely removed leaving only the valid 3D measurement results.

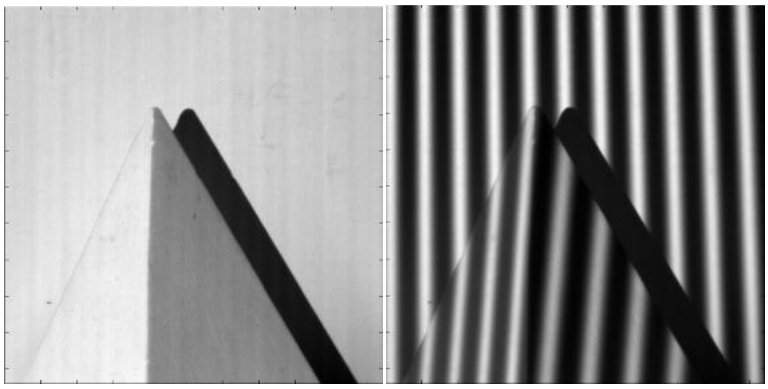

(a) (b)

Fig. 5.3. The measured pyramid and one of the captured fringe patterns.

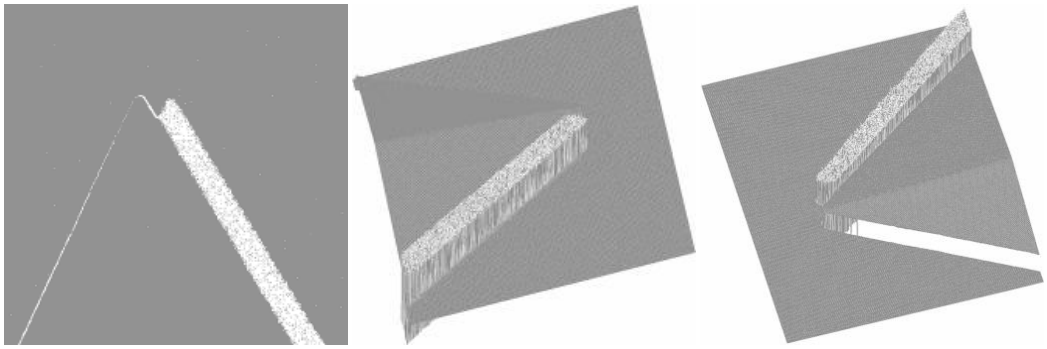

Fig. 5.4. The reconstructed result by PSP with mesh display.

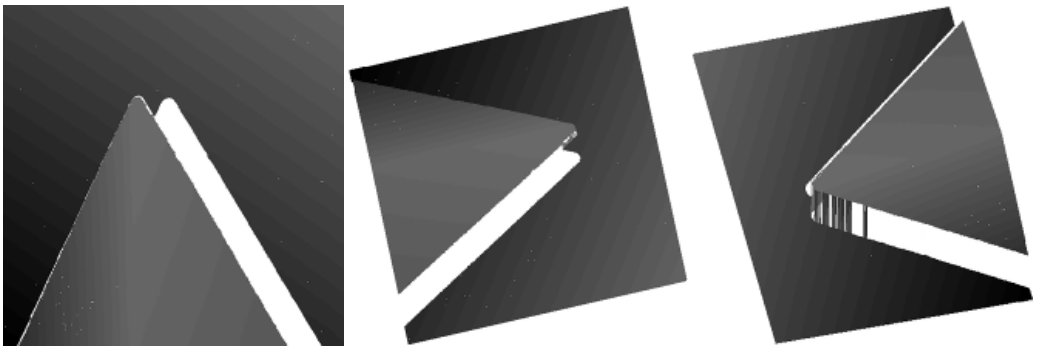

Fig. 5.5. The reconstructed result by the proposed method with the mesh display.

Then, a plaster hand model with complex shape shown in Fig. 5.6(a) is measured in the experiment. Figure 5.6(b) is one of the captured fringe pattern of the object. The shadow area not only exists on the right side of the object, but also exists between the fingers.

Figure 5.7 shows the reconstructed result when the three-step PSP is employed, showing obvious errors in the shadow areas.

Then, the proposed method is applied and the reconstructed result is shown in Fig. 5.8. Compared with the result shown in Fig. 5.7, the points in the shadow area are removed clearly and significant improvement is achieved.

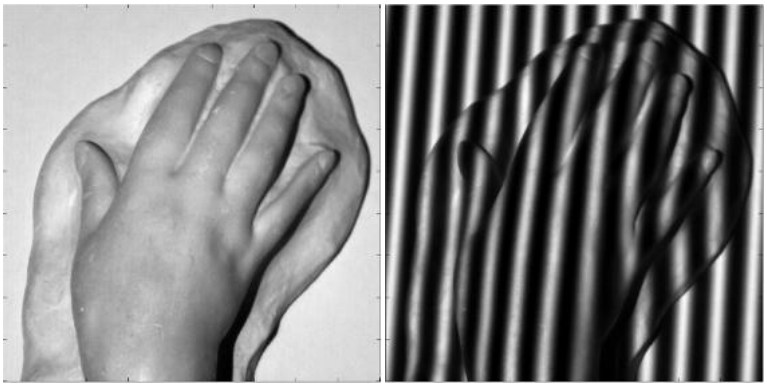

(a) (b)

Fig. 5.6. The measured hand model and one of the captured fringe patterns.

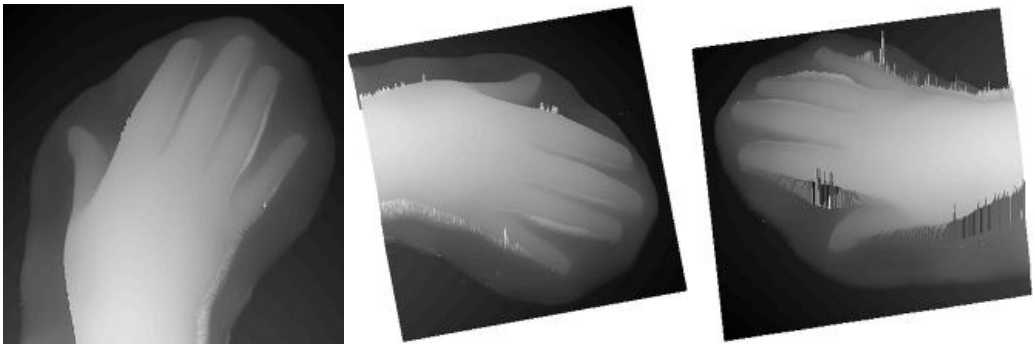

Fig. 5.7. The reconstructed result by PSP with the mesh display.

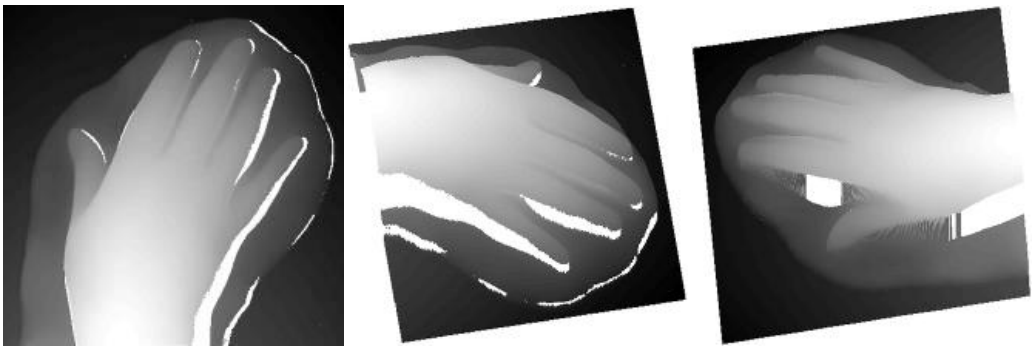

Fig. 5.8. The reconstructed result by the proposed method with the mesh display.

5.4 Conclusion

A new approach to removing the invalid points in the PSP method shadow area has been presented in this chapter. Although the data modulation for the points on the

object is bigger than the points on the shadow area, a threshold is always required which is hard to be determined. Because a threshold is not required, the proposed method is more flexible than existing methods for removing invalid points. Moreover, because the proposed method does not involve operations such as the Gaussian filter and least-squares fitting, it is computationally efficient. The performance of the proposed method has been verified by experiments.

6 CONCLUSION AND FUTURE WORK

Research focusing on techniques for 3D shape measurement of moving objects has been presented in the previous chapters. The major contributions made in this thesis are summarised in Section 6.1, and future work to extend this research is proposed in Section 6.2.

6.1 Conclusion

This thesis has focused on improving the accuracy of multiple-shot FPP techniques for the measurement of moving objects. Several new methods for measuring a moving object with high accuracy have been proposed. The proposed methods not only inherit the advantages of the multiple-shot techniques such as robustness, high accuracy and dense resolution, but are also insensitive to the motion of the object during the measurement. The proposed methods achieve high accuracy in the measurement of a moving object by using information about the movement. The movement of the object is described by a rotation matrix and translation vector, and then the influence on the fringe patterns caused by the movement is analysed and a new expression is derived to describe the fringe patterns after movement. The new expression for the object fringe patterns after movement is used to reconstruct the 3D shape of the object. These approaches are insensitive to the movement of the object and gives improved accuracy of the 3D shape measurement. Different algorithms have been developed to address different types of movement of the object. Specifically, this thesis has made the following major contributions:

(1) The movement of object is described mathematically.

To describe the movement of the object, circle markers are placed on the surface of the object. The centre of the circle markers are used as the corresponding points in the multiple fringe patterns. The least-squares fitting method is used to obtain the rotation matrix and translation vector of the movement.

(2) The influence on the fringe patterns caused by the movement of object is analysed.

The movement of the object can be modelled mathematically by the rotation matrix and translation vector, and when combined with the expression for the fringe patterns, the influence on the fringe patterns caused by the movement of the object can be described.

(3) A new expression for the fringe patterns with movement is obtained.

After the movement of the object is described by the rotation matrix and translation vector, the height distribution of the object surface with movement can be described. Because the height of the object corresponds to the difference in the fringe patterns between the object and the reference plane, a new expression for the fringe patterns with movement can be obtained.

(4) Based on PSP, a method to improve the measurement accuracy of a rigid object with 2D movement is proposed.

2D movement is common in the applications such as when an object is moved by a conveyor belt. Because 2D movement means that the object is moved in a direction that is orthogonal to the height direction, the height of

the object does not vary with the movement. To measure an object that is subjected to 2D movement, the 2D movement is described by a rotation matrix and translation vector. Because the object has a rigid shape, the height of the object does not change with 2D movement. Based on this constraint and the height-phase conversion equation of PSP, the phase distribution after movement can be obtained and used to derive a new expression for the fringe patterns with movement. Because the 2D movement does not introduce unknown parameters into the new expression of the fringe patterns, the phase value of the object can be obtained by solving the equations for the fringe patterns with movement. This method removes the errors caused by 2D movement of the object and high accuracy measurement is achieved.

(5) Based on the triangular fringe pattern and intensity ratio algorithm, a method is proposed to measure the rigid object surface with 2D movement with high accuracy and fast speed.

Instead of using the sinusoidal fringe patterns in PSP, triangular fringe pattern profilometry projects triangular fringe patterns to reconstruct the 3D shape of the object. PSP uses the arctangent function to calculate the phase value, which has a high computational cost. Triangular fringe pattern profilometry uses the intensity ratio to reconstruct the object. This only involves a simple mathematical calculation, and the computational burden is less than for PSP. However, as with all multiple-shot techniques, triangular fringe pattern profilometry also requires that the object must be kept stationary during the projection and capture of the multiple triangular patterns. To achieve high accuracy and fast measurement for objects with 2D movement, a new method

based on triangular fringe pattern profilometry has been proposed to address the errors caused by the 2D movement of rigid object. The 2D movement is still described by the rotation matrix and translation vector. Expressions are then derived for the fringe patterns under the influence of 2D movement of the object and are used to estimate the normalised fringe patterns of the object without movement. Finally, the 3D shape of the object is reconstructed by the existing intensity ratio algorithm. The proposed method can achieve accurate and fast measurement of an object with 2D movement.

(6) Based on PSP, an iterative algorithm is proposed to measure the rigid object with 3D movement.

The above two proposed algorithms are only applicable to 2D movement of an object, which limits them in terms of practical applications. A new method has been proposed to address errors caused by 3D movement of the object to be measured. The object is still assumed to be rigid. When there is 3D movement, the height distribution of the object is changed by the movement, which complicates the problem. Therefore, the movement described in Chapter 4 only includes a translation in the direction of height and 2D movement in the plane perpendicular to the direction of height. The movement is first described by a rotation matrix and translation vector. Then, a new model is proposed to describe the fringe patterns reflected from the object that is subject to 3D movement. Finally, an iterative least-squares algorithm can be applied on the derived fringe patterns to estimate the phase map, leading to improved accuracy of the reconstructed 3D shape of the object.

(7) The invalid points influenced by the shadow area are removed.

Because the camera and projector probe the object from different directions, a shadow area will be introduced into the captured fringe patterns. The shadow area includes no information about the projected fringe patterns, and the results obtained for the shadow area are unreliable and need to be removed. After the object is reconstructed with the influence of the shadow area, points from the result are mapped from the charge-coupled device of the camera to the DMD of the projector. Because only the points reflecting the projected fringe patterns can be used to obtain the correct result, only the valid points from the result will be mapped to the DMD of the projector. The invalid points will be mapped out of the range of the DMD or overlap with other points in DMD. Thus, the invalid points are identified and removed.

6.2 Future work

Although the research in this thesis has successfully improved the accuracy of 3D measurement of a moving object, there are still many issues to be addressed.

1. The markers on the object surface are needed to be removed.

   To obtain the rotation matrix and translation vector of the movement, markers are placed on the surface of the object. This requirement makes the algorithm inflexible. A method to track the movement of the object without using markers is one issue to be addressed. Algorithms from image processing, such as feature extraction, will be helpful.

2. How to improve the accuracy of the 3D shape measurement for the object with arbitrary 3D movement.

The algorithms presented in the thesis did not address all of the possibilities for movement in practice. The object is limited to have a rigid shape and the 3D movement cannot have rotation in the height direction. To extend the application of the 3D shape movement techniques, the above restrictions need to be lifted.

3. How to achieve the 3D shape measurement in the strong ambient light.

   The current 3D shape measurement techniques use projected structured light and are substantially influenced by ambient light when the captured fringe patterns are saturated. When the ambient light is strong, the signal-to-noise ratio is too low to obtain a high quality reconstructed result. Therefore, it is difficult to measure objects outdoors. Invisible light can be used to project the fringe patterns to improve the signal-to-noise ratio, leading to a high quality result for measurement in sunlight.

4. The applications of the FPP need to be extended.

   With the development of the 3D shape measurement technique in this thesis, the measurement result has become more accurate and faster using affordable equipment. More applications can be developed to implement the 3D shape measurement, such as 3D printing and gesture control. We plan to extend the application of the new technique.

7 REFERENCE

[1] J. Smisek, M. Jancosek, and T. Pajdla, "3D with Kinect," *IEEE International Conference on Computer Vision Workshops (ICCV Workshops),* pp. 1154-1160, 2011.

[2] V. R. Duseev, and A. N. Malchukov, "Kinect sensor depth data filtering," *International Conference on Mechanical Engineering, Automation and Control Systems (MEACS),* pp. 1-4, 2014.

[3] C. Liang-Chia, and H. Chung-Chih, "Miniaturized 3D surface profilometer using digital fringe projection," *Measurement Science and Technology,* vol. 16, no. 5, pp. 1061, 2005.

[4] S. T. Yılmaz, U. D. Özugˇurel, K. Bulut, and M. N. Inci, "Vibration amplitude analysis with a single frame using a structured light pattern of a four-core optical fibre," *Optics Communications,* vol. 249, no. 4–6, pp. 515-522, 2005.

[5] Q. Zhang, and X. Su, "High-speed optical measurement for the drumhead vibration," *Optics Express,* vol. 13, no. 8, pp. 3110-3116, 2005.

[6] J. S. Massa, G. S. Buller, A. C. Walker, S. Cova, M. Umasuthan, and A. M. Wallace, "Time-of-flight optical ranging system based on time-correlated single-photon counting," *Applied Optics,* vol. 37, no. 31, pp. 7298-7304, 1998.

[7] D. Amad ud, I. A. Halin, and S. B. Shafie, “A review on solid state time of flight TOF range image sensors,” *IEEE Student Conference on Research and Development (SCOReD),* pp. 246-249, 2009.

[8] E. Lilienblum, and A. Al-Hamadi, “A structured light approach for 3d surface reconstruction with a stereo line-scan system,” *IEEE International Instrumentation and Measurement Technology Conference (I2MTC) Proceedings*, pp. 1171-1176, 2014.

[9] D. Vlasic, P. Peers, I. Baran, P. Debevec, J. Popovic, S. Rusinkiewicz, and W. Matusik, “Dynamic shape capture using multi-view photometric stereo,” *in ACM SIGGRAPH Asia*, pp. 1-11, 2009.

[10] Z. Li, B. Curless, and S. M. Seitz, “Spacetime stereo: shape recovery for dynamic scenes,” *IEEE Computer Society Conference on Computer Vision and Pattern Recognition,* pp. II-367-74 vol.2, 2003.

[11] Z. Yueyi, X. Zhiwei, Y. Zhe, and W. Feng, “Real-Time scalable depth sensing with hybrid structured light illumination,” *IEEE Transactions on Image Processing*, vol. 23, no. 1, pp. 97-109, 2014.

[12] Q. Xue, Z. Wang, J. Huang, and J. Gao, “Improving the measuring accuracy of structured light measurement system,” *Optical Engineering,* vol. 53, no. 11, pp. 112204-112204, 2014.

[13] H. Weidong, G. Mingying, H. Yanhui, S. Lifeng, and Y. Shiqiang, “High-resolution 3D reconstruction for complex color scenes with structured light,” *IEEE International Conference on Multimedia and Expo Workshops (ICMEW),* pp. 1-6, 2014.

[14] L. Merner, Y. Wang, and S. Zhang, “Accurate calibration for 3D shape measurement system using a binary defocusing technique,” *Optics and Lasers in Engineering*, vol. 51, no. 5, pp. 514-519, 2013.

[15] J. Geng, “Structured-light 3D surface imaging: a tutorial,” *Advances in Optics and Photonics*, vol. 3, no. 2, pp. 128-160, 2011.

[16] S. Zhang, D. Van Der Weide, and J. Oliver, “Superfast phase-shifting method for 3-D shape measurement,” *Optics Express*, vol. 18, no. 9, pp. 9684-9689, 2010.

[17] Y. Ding, J. Xi, Y. Yu, and J. Chicharol, “Recovering the absolute phase maps of two fringe patterns with selected frequencies,” *Optics Letters*, vol. 36, no. 13, pp. 2518-2520, 2011.

[18] K. Liu, Y. Wang, D. L. Lau, Q. Hao, and L. G. Hassebrook, “Gamma model and its analysis for phase measuring profilometry,” *Journal of the Optical Society of America A: Optics and Image Science, and Vision*, vol. 27, no. 3, pp. 553-562, 2010.

[19] Y. Hu, J. Xi, J. Chicharo, and Z. Yang, “Blind color isolation for color-channel-based fringe pattern profilometry using digital projection,” *Journal of the Optical Society of America A: Optics and Image Science, and Vision*, vol. 24, no. 8, pp. 2372-2382, 2007.

[20] Z. Hanqi, and Y. Wang, “A coordinate measuring machine with parallel mechanisms,” *IEEE International Conference on Robotics and Automation*, pp. 3256-3261 vol.4, 1997.

[21] A. Wozniak, and M. Dobosz, “Factors influencing probing accuracy of a coordinate measuring machine,” *IEEE Transactions on Instrumentation and Measurement,* vol. 54, no. 6, pp. 2540-2548, 2005.

[22] J. Salvi, S. Fernandez, T. Pribanic, and X. Llado, “A state of the art in structured light patterns for surface profilometry,” *Pattern Recognition,* vol. 43, no. 8, pp. 2666-2680, 2010.

[23] H. Hirschmuller, “Accurate and efficient stereo processing by semi-global matching and mutual information,” *IEEE Computer Society Conference on Computer Vision and Pattern Recognition,* pp. 807-814 vol. 2, 2005.

[24] K. Schreve, “How accurate can a stereovision measurement be?,” *2014 15th International Workshop on Research and Education in Mechatronics (REM),* pp. 1-7, 2014.

[25] J. Battle, E. Mouaddib, and J. Salvi, “Recent progress in coded structured ligth as a technique to solve the correspondence problem: a survey,” *Pattern Recognition,* vol. 31, no. 7, pp. 963-982, 1998.

[26] H. Kawasaki, R. Furukawa, R. Sagawa, and Y. Yagi, “Dynamic scene shape reconstruction using a single structured light pattern,” *IEEE Conference on Computer Vision and Pattern Recognition,* pp. 1-8, 2008.

[27] X. Su, and Q. Zhang, “Dynamic 3-D shape measurement method: A review,” *Optics and Lasers in Engineering,* vol. 48, no. 2, pp. 191-204, 2010.

[28] S. Yu, C. A. Glasbey, G. Polder, and G. W. A. Van Der Heijden, “Non-destructive automatic leaf area measurements by combining stereo and time-of-flight images,” *Computer Vision, IET,* vol. 8, no. 5, pp. 391-403, 2014.

[29] H. Luo, J. Xu, N. Hoa Binh, S. Liu, C. Zhang, and K. Chen, “A simple calibration procedure for structured light system,” *Optics and Lasers in Engineering,* vol. 57, pp. 6-12, 2014.

[30] K. Si, J. Zhang, Z. Li, Z. Guo, X. Lu, and J. Xie, “High-fidelity 3D plants model reconstructed based on color structured light,” *Third International Conference on Agro-geoinformatics,* pp. 1-4, 2014.

[31] Ø. Skotheim, and F. Couweleers, “Structured light projection for accurate 3D shape determination,” *12th International Conference on Experimental Mechanics,* pp. 536-541, 2004.

[32] S. Hsu, S. Acharya, A. Rafii, and R. New, "Performance of a time-of-flight range camera for intelligent vehicle safety applications," *Advanced Microsystems for Automotive Applications,* pp. 205-219, 2006.

[33] M. E. Bouzouraa, M. Kellner, U. Hofmann, and R. Lutz, “Laser scanner based road surface estimation for automotive applications,” *2014 IEEE SENSORS,* pp. 2034-2037, 2014.

[34] Q. Wu, D. Xu, and W. Zou, “A survey on three-dimensional modeling based on line structured light scanner,” *2014 33rd Chinese Control Conference (CCC),* pp. 7439-7444, 2014.

[35] R. A. Morano, C. Ozturk, R. Conn, S. Dubin, S. Zietz, and J. Nissano, "Structured light using pseudorandom codes," *IEEE Transactions on Pattern Analysis and Machine Intelligence,* vol. 20, no. 3, pp. 322-327, 1998.

[36] T. Etzion, "Constructions for perfect maps and pseudorandom arrays," *IEEE Transactions on Information Theory,* vol. 34, no. 5, pp. 1308-1316, 1988.

[37] Z. Zhang, D. Zhang, and X. Peng, "Performance analysis of a 3D full-field sensor based on fringe projection," *Optics and Lasers in Engineering*, vol. 42, no. 3, pp. 341-353, 2004.

[38] S. Lei, and S. Zhang, "Flexible 3-D shape measurement using projector defocusing," *Optics Letters,* vol. 34, no. 20, pp. 3080-3082, 2009.

[39] P. Jia, J. Kofman, and C. English, "Two-step triangular-pattern phase-shifting method for three-dimensional objectshape measurement," *Optical Engineering,* vol. 46, no. 8, pp. 083201, 2007.

[40] P. Jia, J. Kofman, and C. English, "Multiple-step triangular-pattern phase shifting and the influence of number of steps and pitch on measurement accuracy," *Applied Optics,* vol. 46, no. 16, pp. 3253-3262, 2007.

[41] P. S. Huang, S. Zhang, and F. P. Chiang, "Trapezoidal phase-shifting method for three-dimensional shape measurement," *Optical Engineering,* vol. 44, no. 12, pp. 123601, 2005.

[42] L. Chen, C. Quan, C. J. Tay, and Y. Fu, "Shape measurement using one frame projected sawtooth fringe pattern," *Optics Communications,* vol. 246, no. 4–6, pp. 275-284, 2005.

[43] S. S. Gorthi, and P. Rastogi, “Fringe projection techniques: Whither we are?,” *Optics and Lasers in Engineering,* vol. 48, no. 2, pp. 133-140, 2010.

[44] H. Yingsong, X. Jiangtao, J. F. Chicharo, C. Wenqing, and Y. Zongkai, “Inverse function analysis method for fringe pattern profilometry,” *IEEE Transactions on Instrumentation and Measurement,* vol. 58, no. 9, pp. 3305-3314, 2009.

[45] M. Takeda, H. Ina, and S. Kobayashi, “Fourier-transform method of fringe-pattern analysis for computer-based topography and interferometry,” *Journal of the Optical Society of America,* vol. 72, no. 1, pp. 156-160, 1982.

[46] X. Su, W. Chen, Q. Zhang, and Y. Chao, “Dynamic 3-D shape measurement method based on FTP,” *Optics and Lasers in Engineering,* vol. 36, no. 1, pp. 49-64, 2001.

[47] X. Su, and W. Chen, “Fourier transform profilometry:: a review,” *Optics and Lasers in Engineering,* vol. 35, no. 5, pp. 263-284, 2001.

[48] M. Takeda, “Spatial-carrier fringe-pattern analysis and its applications to precision interferometry and profilometry: An overview,” *Industrial Metrology,* vol. 1, no. 2, pp. 79-99, 1990.

[49] C. Wust, and D. Capson, “Surface profile measurement using color fringe projection,” *Machine Vision and Applications,* vol. 4, no. 3, pp. 193-203, 1991.

[50] A. Pförtner, and J. Schwider, "Red-green-blue interferometer for the metrology of discontinuous structures," *Applied Optics,* vol. 42, no. 4, pp. 667-673, 2003.

[51] P. S. Huang, C. Zhang, and F.-P. Chiang, "High-speed 3-D shape measurement based on digital fringe projection," *Optical Engineering,* vol. 42, no. 1, pp. 163-168, 2003.

[52] P. S. Huang, Q. Hu, F. Jin, and F.-P. Chiang, "Color-encoded digital fringe projection technique for high-speed three-dimensional surface contouring," *Optical Engineering,* vol. 38, no. 6, pp. 1065-1071, 1999.

[53] Z. Zhang, C. E. Towers, and D. P. Towers, "Time efficient color fringe projection system for 3D shape and color using optimum 3-frequency Selection," *Optics Express,* vol. 14, no. 14, pp. 6444-6455, 2006.

[54] Z. H. Zhang, C. E. Towers, and D. P. Towers, "Phase and colour calculation in colour fringe projection," *Journal of Optics A: Pure and Applied Optics,* vol. 9, no. 6, pp. S81, 2007.

[55] W.-H. Su, "Color-encoded fringe projection for 3D shape measurements," *Optics Express,* vol. 15, no. 20, pp. 13167-13181, 2007.

[56] H. J. Chen, J. Zhang, D. J. Lv, and J. Fang, "3-D shape measurement by composite pattern projection and hybrid processing," *Optics Express,* vol. 15, no. 19, pp. 12318-12330, 2007.

[57] W.-H. Su, “Projected fringe profilometry using the area-encoded algorithm for spatially isolated and dynamic objects,” *Optics Express,* vol. 16, no. 4, pp. 2590-2596, 2008.

[58] Z. Zhang, D. P. Towers, and C. E. Towers, “Snapshot color fringe projection for absolute three-dimensional metrology of video sequences,” *Applied Optics,* vol. 49, no. 31, pp. 5947-5953, 2010.

[59] Z. H. Zhang, “Review of single-shot 3D shape measurement by phase calculation-based fringe projection techniques,” *Optics and Lasers in Engineering,* vol. 50, no. 8, pp. 1097-1106, 2012.

[60] C. Guan, L. G. Hassebrook, and D. L. Lau, “Composite structured light pattern for three-dimensional video,” *Optics Express,* vol. 11, no. 5, pp. 406-417, 2003.

[61] I. Ishii, K. Yamamoto, K. Doi, and T. Tsuji, “High-speed 3D image acquisition using coded structured light projection,” IEEE *International Conference on Intelligent Robots and Systems,* pp. 925-930, 2007.

[62] R. J. Valkenburg, and A. M. McIvor, “Accurate 3D measurement using a structured light system,” *Image and Vision Computing,* vol. 16, no. 2, pp. 99-110, 1998.

[63] J. L. Posdamer, and M. D. Altschuler, “Surface measurement by space-encoded projected beam systems,” *Computer Graphics and Image Processing,* vol. 18, no. 1, pp. 1-17, 1982.

[64] J. Salvi, J. Pagès, and J. Batlle, “Pattern codification strategies in structured light systems,” *Pattern Recognition,* vol. 37, no. 4, pp. 827-849, 2004.

[65] J. Pan, P. S. Huang, S. Zhang, and F.-P. Chiang, “Color N-ARY gray code for 3-D shape measurement,” *12th International Conference on Experimental Mechanics,* 2004.

[66] D. Caspi, N. Kiryati, and J. Shamir, “Range imaging with adaptive color structured light,” *IEEE Transactions on Pattern Analysis and Machine Intelligence,* vol. 20, no. 5, pp. 470-480, 1998.

[67] E. Horn, and N. Kiryati, “Toward optimal structured light patterns,” *in 3-D Digital Imaging and Modeling, International Conference on Recent Advances,* pp. 28-35, 1997.

[68] P. Jia, J. Kofman, and C. English, “Error compensation in two-step triangular-pattern phase-shifting profilometry,” *Optics and Lasers in Engineering,* vol. 46, no. 4, pp. 311-320, 2008.

[69] P. Jia, J. Kofman, C. English, and A. Deslauriers, “Two-step triangular phase-shifting method for 3-D object-shape measurement,” *Proceedings of SPIE - Volume 6049, Optomechatronic Machine Vision,* pp.6049-21, 2005.

[70] B. Carrihill, and R. Hummel, “Experiments with the intensity ratio depth sensor,” *Computer Vision, Graphics, and Image Processing,* vol. 32, no. 3, pp. 337-358, 1985.

[71] T. Miyasaka, K. Kuroda, M. Hirose, and K. Araki, “Reconstruction of realistic 3D surface model and 3D animation from range images obtained by

real time 3D measurement system," *International Conference on Pattern Recognition,* vol. 15, no. 4, pp. 594-597, 2000.

[72] G. Chazan and N. Kiryati, "Pyramidal intensity-ratio depth sensor," *Technion Israel Institute of Technology,* 1995.

[73] J. B. S. Savarese, and P. Perona, "3D depth recovery with grayscale structured lighting," *California Insititute of Tech-nology,* 1998.

[74] T. Miyasaka, and K. Araki, "Development of real time 3-D measurement system using intensity ratio method," *Graduate School of Computer and Cognitive Sciences, Chukyo University, Japan,* 2010.

[75] S. Zhang, "High-resolution 3D profilometry with binary phase-shifting methods," *Applied Optics,* vol. 50, no. 12, pp. 1753-1757, 2011.

[76] Y.-Y. Cheng, and J. C. Wyant, "Phase shifter calibration in phase-shifting interferometry," *Applied Optics,* vol. 24, no. 18, pp. 3049-3052, 1985.

[77] G. Lai, and T. Yatagai, "Generalized phase-shifting interferometry," *Journal of the Optical Society of America A,* vol. 8, no. 5, pp. 822-827, 1991.

[78] V. Srinivasan, H. C. Liu, and M. Halioua, "Automated phase-measuring profilometry of 3-D diffuse objects," *Applied Optics,* vol. 23, no. 18, pp. 33105-3108, 1984.

[79] X.-Y. Su, W.-S. Zhou, G. von Bally, and D. Vukicevic, "Automated phase-measuring profilometry using defocused projection of a Ronchi grating," *Optics Communications,* vol. 94, no. 6, pp. 561-573, 1992.

[80] H.-J. Su, J.-L. Li, and X.-Y. Su, “Phase algorithm without the influence of carrier frequency,” *Optical Engineering,* vol. 36, no. 6, pp. 1799-1805, 1997.

[81] R. M. Goldstein, H. A. Zebker, and C. L. Werner, “Satellite radar interferometry:Two dimensional phase unwrapping,” *Radio Science,* vol. 23, no. 4, pp. 713-720, 1988.

[82] H. Zhao, W. Chen, and Y. Tan, “Phase-unwrapping algorithm for the measurement of three-dimensional object shapes,” *Applied Optics,* vol. 33, no. 20, pp. 4497-4500, 1994.

[83] S. Fang, L. Meng, L. Wang, P. Yang, and M. Komori, “Quality-guided phase unwrapping algorithm based on reliability evaluation,” *Applied Optics,* vol. 50, no. 28, pp. 5446-5452, 2011.

[84] C. Bräuer-Burchardt, P. Kühmstedt, and G. Notni, “Phase unwrapping using geometric constraints for high-speed fringe projection based 3D measurements,” *Proceeding of SPIE 8789, Modeling Aspects in Optical Metrology IV,* pp. 878906, 2013.

[85] C. Brenner, J. Boehm, and J. Guehring, “Photogrammetric calibration and accuracy evaluation of a cross-pattern stripe projector,” *Proceeding of SPIE 3641, Videometrics VI, 164,* pp. 164-172, 1998.

[86] J. M. Huntley, “Noise immune phase unwrapping algorithm,” *Applied Optics,* vol. 28, no. 15, pp. 3268-3210, 1989.

[87] Y. Ding, J. Xi, Y. Yu, W. Cheng, S. Wang, and J. F. Chicharo, "Frequency selection in absolute phase maps recovery with two frequency projection fringes," *Optics Express,* vol. 20, no. 12, pp. 13238-13251, 2012.

[88] J. Lu, and H. Su, "Fast phase unwrapping algorithm based on region partition for structured light vision measurement," *Optical Engineering,* vol. 53, no. 4, pp. 044103, 2014.

[89] W. Lohry, V. Chen, and S. Zhang, "Absolute three-dimensional shape measurement using coded fringe patterns without phase unwrapping or projector calibration," *Optics Express,* vol. 22, no. 2, pp. 1287-1301, 2014.

[90] K. Wu, J. Xi, Y. Yu, and Z. Yang, "3D profile measurement based on estimation of spatial shifts between intensity ratios from multiple-step triangular patterns," *Optics and Lasers in Engineering,* vol. 51, no. 4, pp. 440-445, 2013.

[91] Z. Yang, K. Wu, J. Xi, and Y. Yu, "Intensity ratio approach for 3D profile measurement based on projection of triangular patterns," *Applied Optics,* vol. 53, no. 2, pp. 200-207, 2014.

[92] F. Yuan, D. Song, and L. Zeng, "Measuring 3D profile and position of a moving object in large measurement range by using tracking fringe pattern," *Optics Communications,* vol. 196, no. 1–6, pp. 85-91, 2001.

[93] S. Tan, D. Song, and L. Zeng, "A tracking fringe method for measuring the shape and position of a swimming fish," *Optics Communications,* vol. 173, no. 1–6, pp. 123-128, 2000.

[94] S. Rusinkiewicz, O. Hall-Holt, and M. Levoy, "Real-time 3D model acquisition," *ACM Transactions on Graphics (SIGGRAPH),* vol. 21, no. 3, pp. 438-446, 2002.

[95] O. Hall-Holt, and S. Rusinkiewicz, "Stripe boundary codes for real-time structured-light range scanning of moving objects," *IEEE International Conference on Computer Vision,* pp. 359-366 vol.2, 2001.

[96] S. Zhang, and S. T. Yau, "High-speed three-dimensional shape measurement system using a modified two-plus-one phase-shifting algorithm," *Optical Engineering,* vol. 46, no. 11, pp. 113603, 2007.

[97] T. Weise, B. Leibe, and L. Van Gool, "Fast 3D scanning with automatic motion compensation," *IEEE Conference on Computer Vision and Pattern Recognition,* pp. 1-8, 2007.

[98] L. Guo, X. Su, and J. Li, "Improved Fourier transform profilometry for the automatic measurement of 3D object shapes," *Optical Engineering,* vol. 29, no. 12, pp. 1439-1444, 1990.

[99] E. Hu, and Y. He, "Surface profile measurement of moving objects by using an improved π phase-shifting Fourier transform profilometry," *Optics and Lasers in Engineering,* vol. 47, no. 1, pp. 57-61, 2009.

[100] B. Li, N. Karpinsky, and S. Zhang, "Novel calibration method for structured-light system with an out-of-focus projector," *Applied Optics,* vol. 53, no. 16, pp. 3415-3426, 2014.

[101] T. Wakayama, and T. Yoshizawa, “High-speed three-dimensional shape measurements using multiwavelength spatiotemporal phase shifting,” *Optical Engineering,* vol. 53, no. 11, pp. 112207, 2014.

[102] C. Zuo, Q. Chen, G. Gu, S. Feng, and F. Feng, “High-speed three-dimensional profilometry for multiple objects with complex shapes,” *Opt. Express,* vol. 20, no. 17, pp. 19493-19510, 2012.

[103] L. Yong, Z. Cuifang, W. Hui, and J. Hongzhen, “High-speed three-dimensional shape measurement for isolated objects based on fringe projection,” *Journal of Optics,* vol. 13, no. 3, pp. 035403, 2011.

[104] Y. Wang, S. Zhang, and J. H. Oliver, “3D shape measurement technique for multiple rapidly moving objects,” *Optics Express,* vol. 19, no. 9, pp. 8539-8545, 2011.

[105] O. A. Skydan, M. J. Lalor, and D. R. Burton, “Using coloured structured light in 3-D surface measurement,” *Optics and Lasers in Engineering,* vol. 43, no. 7, pp. 801-814, 2005.

[106] S. Zhang, “Phase unwrapping error reduction framework for a multiple-wavelength phase-shifting algorithm,” *Optical Engineering,* vol. 48, no. 10, pp. 105601-105608, 2009.

[107] F. Chen, X. Su, and L. Xiang, “Analysis and identification of phase error in phase measuring profilometry,” *Optics Express,* vol. 18, no. 11, pp. 11300-11307, 2010.

[108] H. Lei, and A. Anand Krishna, “Phase invalidity identification framework with the temporal phase unwrapping method,” *Measurement Science and Technology,* vol. 22, no. 3, pp. 035304, 2011.

[109] S. Zhang, “Composite phase-shifting algorithm for absolute phase measurement,” *Optics and Lasers in Engineering,* vol. 50, no. 11, pp. 1538-1541, 2012.

[110] D. L. Lau, K. Liu, and L. G. Hassebrook, “Real-time three-dimensional shape measurement of moving objects without edge errors by time-synchronized structured illumination,” *Optics Letters,* vol. 35, no. 14, pp. 2487-2489, 2010.

[111] K. Zhong, Z. Li, Y. Shi, C. Wang, and Y. Lei, “Fast phase measurement profilometry for arbitrary shape objects without phase unwrapping,” *Optics and Lasers in Engineering,* vol. 51, no. 11, pp. 1213-1222, 2013.

[112] P. S. Huang, and S. Zhang, “Fast three-step phase-shifting algorithm,” *Applied Optics,* vol. 45, no. 21, pp. 5086-5091, 2006.

[113] B. Li, Y. Wang, J. Dai, W. Lohry, and S. Zhang, “Some recent advances on superfast 3D shape measurement with digital binary defocusing techniques,” *Optics and Lasers in Engineering,* vol. 54, pp. 236-246, 2014.

[114] Y. Wang, J. I. Laughner, I. R. Efimov, and S. Zhang, “3D absolute shape measurement of live rabbit hearts with a superfast two-frequency phase-shifting technique,” *Optics Express,* vol. 21, no. 5, pp. 5822-5832, 2013.

[115] Z. Song, “Recent progresses on real-time 3-D shape measurement using digital fringe projection techniques,” *Optics and Lasers in Engineering,* vol. 48, pp. 149-158, 2010.

[116] R. Legarda-Sa´enz, T. Bothe, and W. P. Ju¨ptner, “Accurate procedure for the calibration of a structured light system,” *Optical Engineering,* vol. 43, no. 2, pp. 464-471, 2004.

[117] F. J. Cuevas, M. Servin, and R. Rodriguez-Vera, “Depth object recovery using radial basis functions,” *Optics Communications,* vol. 163, no. 4–6, pp. 270-277, 1999.

[118] F. J. Cuevas, M. Servin, O. N. Stavroudis, and R. Rodriguez-Vera, “Multi-layer neural network applied to phase and depth recovery from fringe patterns,” *Optics Communications,* vol. 181, no. 4–6, pp. 239-259, 2000.

[119] J. Heikkila, “Geometric camera calibration using circular control points,” *IEEE Transactions on Pattern Analysis and Machine Intelligence,* vol. 22, no. 10, pp. 1066-1077, 2000.

[120] F. Pedersini, A. Sarti, and S. Tubaro, “Accurate and simple geometric calibration of multi-camera systems,” *Signal Processing,* vol. 77, no. 3, pp. 309-334, 1999.

[121] Q. Hu, P. S. Huang, Q. Fu, and F.-P. Chiang, “Calibration of a three-dimensional shape measurement system,” *Optical Engineering,* vol. 42, no. 2, pp. 487-493, 2003.

[122] S. Zhang, and P. S. Huang, “Novel method for structured light system calibration,” *Optical Engineering,* vol. 45, no. 8, pp. 083601, 2006.

[123] Z. Zhengyou, “A flexible new technique for camera calibration,” *IEEE Transactions on Pattern Analysis and Machine Intelligence,* vol. 22, no. 11, pp. 1330-1334, 2000.

[124] P. Meer, D. Mintz, A. Rosenfeld, and D. Kim, “Robust regression methods for computer vision: A review,” *International Journal of Computer Vision,* vol. 6, no. 1, pp. 59-70, 1991.

[125] K. S. Arun, T. S. Huang, and S. D. Blostein, “Least-squares fitting of two 3-D point sets,” *IEEE Transactions on Pattern Analysis and Machine Intelligence,* vol. PAMI-9, no. 5, pp. 698-700, 1987.

[126] B. K. P. Horn, “Closed-form solution of absolute orientation using unit quaternions,” *Journal of the Optical Society of America A,* vol. 4, no. 4, pp. 629-642, 1987.

[127] A. Trujillo-Pino, K. Krissian, M. Alemán-Flores, and D. Santana-Cedrés, “Accurate subpixel edge location based on partial area effect,” *Image and Vision Computing,* vol. 31, no. 1, pp. 72-90, 2013.

[128] Y. Hu, J. Xi, Z. Yang, E. Li, and J. F. Chicharo, “Study on generalized analysis model for fringe pattern profilometry,” *IEEE Transactions on Instrumentation and Measurement,* vol. 57, no. 1, pp. 160-167, 2008.

[129] Z. Wang, and B. Han, "Advanced iterative algorithm for phase extraction of randomly phase-shiftedinterferograms," *Optics Letters,* vol. 29, no. 14, pp. 1671-1673, 2004.

[130] X. F. Xu, L. Z. Cai, X. F. Meng, G. Y. Dong, and X. X. Shen, "Fast blind extraction of arbitrary unknown phase shifts by an iterative tangent approach in generalized phase-shifting interferometry," *Optics Letters,* vol. 31, no. 13, pp. 1966-1968, 2006.

[131] C.-S. Guo, B. Sha, Y.-Y. Xie, and X.-J. Zhang, "Zero difference algorithm for phase shift extraction in blind phase-shifting holography," *Optics Letters,* vol. 39, no. 4, pp. 813-816, 2014.

[132] R. Juarez-Salazar, C. Robledo-Sanchez, F. Guerrero-Sanchez, and A. Rangel-Huerta, "Generalized phase-shifting algorithm for inhomogeneous phase shift and spatio-temporal fringe visibility variation," *Optics Express,* vol. 22, no. 4, pp. 4738-4750, 2014.

[133] Q. Zhang, X. Su, L. Xiang, and X. Sun, "3-D shape measurement based on complementary Gray-code light," *Optics and Lasers in Engineering,* vol. 50, no. 4, pp. 574-579, 2012.

[134] H. Guo, and Z. Zhang, "Phase shift estimation from variances of fringe pattern differences," *Applied Optics,* vol. 52, no. 26, pp. 6572-6578, 2013.

[135] S. Zhang, and S.-T. Yau, "High-resolution, real-time 3D absolute coordinate measurement based on a phase-shifting method," *Optics Express,* vol. 14, no. 7, pp. 2644-2649, 2006.

[136] X.-Y. Su, G. von Bally, and D. Vukicevic, “Phase-stepping grating profilometry: utilization of intensity modulation analysis in complex objects evaluation,” *Optics Communications*, vol. 98, no. 1–3, pp. 141-150, 1993.